MULTIPHASE MEMBRANE CONTACTORS AND REACTORS

MODELING AND OPTIMIZATION STUDY

The research presented in this thesis was financially supported by Stichting voor de Technische Wetenschappen (STW, Project 07569).

Committee members

Prof. Dr.ir. R.G.H. Lammertink	(Promotor)	University of Twente
Prof. Dr.-Ing. M.Wessling	(Co-promotor)	University of Twente RWTH Aachen University, Germany
Prof. Dr. J.G.E. Gardeniers		University of Twente
Prof. Dr.ir. T.H. van der Meer		University of Twente
Prof. Dr. G. Mul		University of Twente
Dr.ir. D.W.F. Brilman		University of Twente
Prof. Dr. K. Li		Imperial College London, UK

Title: Multiphase Membrane Contactors and Reactors: Modeling and optimization study

ISBN: 978-90-365-3295-2
DOI: http://dx.doi.org/10.3990/1.9789036532952
Printing: Drukkerij Gildeprint, Enschede, The Netherlands

MULTIPHASE MEMBRANE CONTACTORS AND REACTORS

MODELING AND OPTIMIZATION STUDY

DISSERTATION

to obtain
the degree of doctor at the University of Twente,
on the authority of the rector magnificus,
Prof. Dr. H. Brinksma,
on account of the decision of the graduation committee,
to be publicly defended on
Friday, 02 December 2011, at 12:45 hrs

by

Jigar Madhusudan Jani

born on 21 September 1980
in Anand, India

This thesis has been approved by:

Promotor
Prof. Dr.Ir. R. (Rob) G.H. Lammertink

Co-promotor
Prof. Dr.-Ing. M. (Matthias) Wessling

To My Parents

Contents

CHAPTER 1

Introduction

Abstract

This chapter presents the theoretical background and objectives of the research work that is presented in this thesis. The principles of microscopic multiphase flow and main advantages of microreaction technology are discussed. An in depth discussion is presented regarding the specific requirements of microreaction technology in the field of gas-liquid contacting/reaction.

1.1 Microreaction technology

Microreaction technology concerns process intensification that involves miniaturized reaction domain with dimensions typically smaller than a millimeter. Due to short diffusion lengths in their sub-millimeter channnels (typical dimensions are 50 to 500 μm), microreactors offer high heat and mass transfer rates along with short residence time and small fluid hold-up [1]. With increased surface-to-volume ratio (typical values are in the range of 10,000 to 100,000 m^2/m^3), it is possible to carry out processes in small volumes which facilitate the application of high concentration and/or temperature. This could allow traditionally infeasible process routes to be achieved with enhanced performance [1–4]. On the other hand, sub-millimeter dimensions give improvements (enhanced mass and heat transfer) in reaction conditions where high interfacial area can be obtained [5–8]. Microreactors have developed to a level where such devices are not only limited to the academic domain but have gathered significant interest for applications in industry. In general, microreactors consist of the following characteristics:

- Enhanced heat and mass transfer rates giving stable operating conditions
- Operated continuously
- Small flow rates per channel, creating laminar flow conditions
- Improved process safety for potentially fast and difficult reactions
- Precise control of reactions is possible due to narrow residence time distribution
- Increase in conversion and selectivity

The advantages offered by microreactors are specifically expected for fast, highly exothermic or endothermic reactions [3]. Moreover, a high surface-to-volume ratio is beneficial for heterogeneously catalyzed reactions or transport-limited processes [9, 10]. However, in order to effectively exploit microreactor technology into a wide range of applications, it is necessary to ensure appropriate multiphase contacting and mixing at the microscale [11, 12].

Different materials can be employed to produce microreactors, including metals, polymers, ceramics, glasses and silicon. Microstructuring methods include micromachining, lithography and etching, replication and laser ablation processes. The integration of specifically designed unit operations such as reactors, fluid-fluid separators, micromixers

and heat exchangers makes the whole system suitable for process intensification.

In general, microreactor design is governed by different constraints, such as material properties, fabrication methods, geometrical configurations and economics. Apart from that, characteristic time and length scales need to be taken into account for hydrodynamics, mass and heat transfer, and reaction kinetics. It is therefore crucial to implement detailed descriptions of these in predictive models that can aid in the design of microreactors.

1.2 Multiphase microreactors

At the microscale, properties such as surface tension of fluid, viscosity and surface wetting become more dominant compared to volume forces like gravity, pressure or momentum. There are mainly two distinct characteristics of multiphase flows at the microscale,

- Increased influence of surface forces over volume forces.
- Reynolds number is very small, so laminar flow is established.

Because of the above mentioned characteristics, multiphase flow in microchannels behaves differently compared to macrosized devices [13–17]. The influence of interfacial tension, gravity, intertial and viscous forces gives different formations of complex flow patterns. The physical behavior of a multiphase system can be represented by following dimensionless numbers. The Reynolds number is defined as the ratio of inertial to viscous forces;

$$Re = \frac{\rho U L}{\mu} \tag{1.1}$$

Where, ρ is the density of the fluid, U is the characteristic velocity of the flow, L is the characteristic length scale and μ is the viscosity of the fluid. Due to very small characteristic dimension of the microchannel and low velocity, Re is very small ($Re < 100$). This implies that mixing is mainly governed by molecular diffusion. To estimate the relative importance of diffusion, we compare the typical time scale for diffusion (L^2/D) and the time scale for convection (L/U). The relationship between

convection and diffusion is represented by Péclet number:

$$Pe = \frac{UL}{D} \tag{1.2}$$

where D is the solute diffusion coefficient. The Péclet number and the Reynolds number are related by $Pe = ReSc$. Here, Sc is the Schmidt number defined by $Sc = \mu/\rho D$ (the ratio of viscous diffusion over molecular diffusion). For higher Pe, the influence of convective flow is more important than the molecular diffusion. A typical Pe value in microchannels is $O(10^2)$, which indicates that diffusive mass transfer occurs at much lower rate than the typical timescales involved for convective fluid flow.

The interfacial forces with respect to gravity is described by the Bond number (Bo):

$$Bo = \frac{\Delta\rho g L^2}{\gamma} \tag{1.3}$$

where $\Delta\rho$ is the density difference between the phases, g is the gravity acceleration and γ is the interfacial tension. Since the Bond number gives a measure of the importance of surface tension force compared to body forces, it can be used to characterize the shape of phase interface. For multiphase microreactor applications, Bo is typically very small ($\leq 10^{-3}$).

The importance of inertial forces to interfacial forces is expressed by the Weber number:

$$We = \frac{\rho U^2 L}{\gamma} \tag{1.4}$$

The Weber number can be useful in analyzing thin films and the formation of droplets and bubbles.

Multiphase reactors show a wide range of fluid flow characteristics depending on the relative flow rates of the phases involved. Based on the relative influence of the surface tension and inertial forces, mainly three flow regimes are observed. These are identified as *surface tension dominated*, *inertia dominated* and *transitional* regimes. These regimes consist of different flow patterns, including Taylor and bubbly flow (surface tension dominated), dispersed and annular flow (inertia dominated), and churn and Taylor-annular flow (transitional) [18]. The repeated perturbations at the

fluid-fluid interface causes specific flow conditions. Such conditions are beneficial for microstructured reactors offering enhanced mixing, large interfacial areas and decreased mass transfer limitations [11, 19].

Multiphase reactions for gas-liquid (G-L) or heterogeneously catalyzed gas-liquid-solid (G-L-S) systems can be carried out in a number of reactor configurations. Examples include structured catalyst in monoliths, bubble column, trickle bed, fixed bed and dispersed phase reactors [11]. Membrane reactors furthermore provide controlled phase contacting and relatively simple design [20]. Microreactors can be employed for a variety of applications such as emulsification [21, 22], material processing and chemical reactions [12, 23–26]. Multiphase reactors have become essential in many process engineering applications involving gas-liquid-solid (G-L-S) [27, 28] or liquid-liquid-solid reactions, such as hydrogenation [27, 29–31] and in challenging gas-liquid reactions, such as fluorination [6, 32, 33], dehydration [34], dehydrogenation [35] and oxidation [36] reactions.

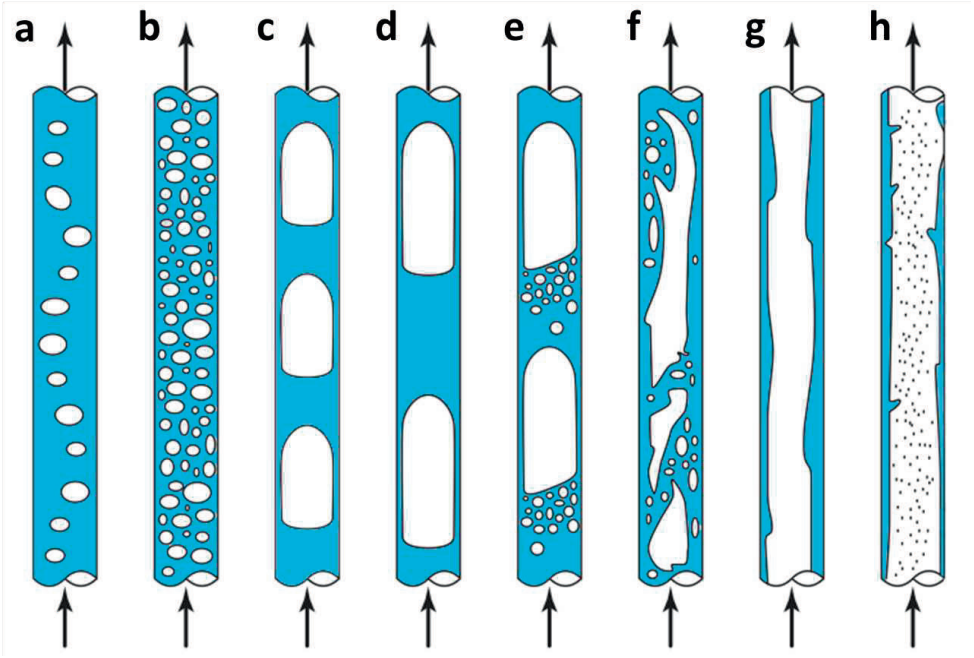

Figure 1.1: General classification of gas-liquid two-phase flow patterns: (a) dispersed bubble flow (b) bubble flow (c) elongated bubble flow (d) Taylor flow (e) slug flow (f) churn flow (g) annular flow (h) mist flow (Adapted from Heiszwolf et al. [37]).

1.2.1 Gas-liquid flow

Depending on the gas and liquid flow rates, a number of different flow regimes can be observed (Fig.1.1). Some of the important flow regimes are: *dispersed bubble flow* in which number of smaller diameter bubbles are dispersed in the liquid (Fig.1.1 a,b), *segmented flow* in which liquid plugs and gas bubbles fill the microchannel alternatively (Fig.1.1 c,d), *slug/churn flow* in which parts of the liquid intermittently block the microchannel (Fig.1.1 e,f) and *film and annular flow* in which a thin film of liquid flows along the channel wall with gas flowing in the center of the channel (Fig.1.1 g,h).

Out of all the different flow regimes mentioned above, Taylor flow is the most studied regarding multiphase microreactors. Typically, a circulating flow is observed in the liquid slug due to the axial flow of bubbles. This liquid circulation in the slugs improves radial mass transfer [37–40].

Multiphase microreactors [11, 41, 42] are mainly categorized in two types: *continuous* and *dispersed phase* microreactors. In the continuous-phase contacting, both phases remain non-dispersed with a separate inlet and outlet (e.g. falling film microreactor). Dispersed-phase contacting is achieved when one of the phases is dispersed into the other phase creating various flow patterns (e.g. Taylor flow) [11]. In both types of microreactors, it is necessary to control the G/L flow ratios in order to realize a stable interface.

1.2.2 Wetting characteristics of microchannel surface

The microchannel surface is characterized by its wetting behavior (Fig.1.2). Wetting properties are affected by surface chemistry and structure. The wetting behavior of a surface by a liquid can be represented by the contact angle θ , which is represented by angle between the G-L and the L-S interface (Fig 1.2c). A hydrophilic surface exhibits a water contact angle of $\theta < 90°$, while a hydrophobic surface has a higher contact angle of $90° < \theta < 180°$.

The contact angle can be experimentally measured at the three-phase contact line of a liquid drop on a solid surface. The wetting phenomenon can be described in terms of the Young's equation, with the equilibrium of the interfacial tension between the different phases (G-L-S) determining the contact angle (θ) [43]. It is defined as:

$$cos\theta = \frac{\gamma_{SG} - \gamma_{LS}}{\gamma_{LG}} \tag{1.5}$$

where γ_{SG}, γ_{LS} and γ_{LG} are the solid-gas, liquid-solid and liquid-gas interfacial tensions, respectively.

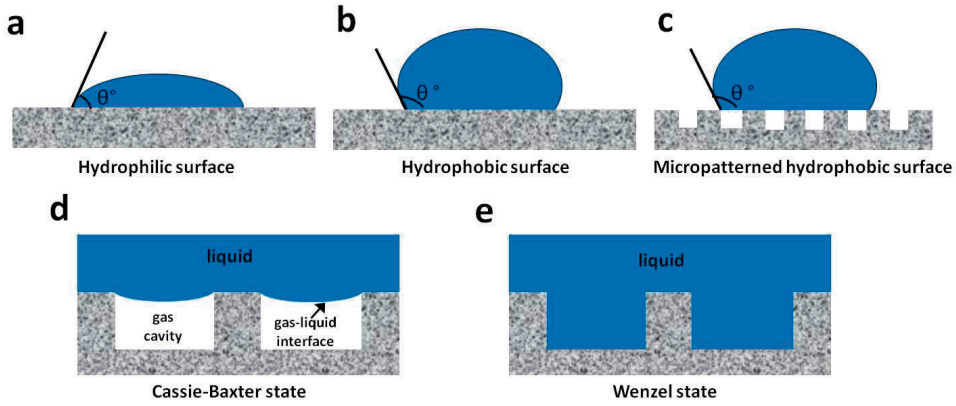

Figure 1.2: Water droplet on (a) a flat hydrophilic surface (b) a flat hydrophobic surface (c) a micropatterned hydrophobic surface; liquid representing (d) Cassie-Baxter state (e) Wenzel state.

The wetting condition that exhibits a contact angle higher than 150° is called superhydrophobicity. Superhydrophobic surfaces resemble the self-cleaning mechanism of the lotus leaf, which later led to coin the term *lotus effect* [44]. The *lotus effect* describes a condition in which a liquid is partly in contact with gas and partly with the rough or microstructured solid surface.

The characateristics of liquid behavior on the solid rough surface can be represented by two states: Cassie-Baxter [45] state and Wenzel state [46] (Fig. 1.2d and e). The Wenzel state is observed when the water penetrates into the microstructures (Fig. 1.2e). In the Cassie-Baxter state, the hydrophobicity of the microscale structured surface prevents the water from entering into the cavity, resulting in a G-L interface as seen in Fig. 1.2d. This leads to an increased contact angle for the water droplet. The water on hydrophobic microstructured surface will remain in non-wetted state (Cassie-Baxter state) as long as the pressure differential across the G-L interface is not too high and gas will remain entrapped in the cavity region.

The overall shear stress, offered by microstructured hydrophobic surface for liquid flowing past, decreases drastically compared to normal hydrophobic surface. This is observed since the liquid will not wet the cavity regions, which leads to reduction in the interfacial liquid-solid contact area (Fig. 1.2d). The boundary condition for the liquid in contact with the solid surface is a no-slip condition [47], whereas the G-L interfaces (existing between the microstructures or patterns) is shear-free which gives rise to a slip boundary condition. The magnitude of the slip velocity [48, 49] at the wall is quantified by:

$$u_{slip} = b\frac{\partial U}{\partial n} \tag{1.6}$$

where u_{slip} is the slip velocity, b is the slip-length and $\partial U/\partial n$ is velocity gradient normal to the surface.

1.3 Membrane reactors and contactors

Membrane based G-L contacting is widely used in order to establish a stabilized interface between two phases. Porous membranes represent a physical separator between two phases [50]. Such membranes offer many advantages over conventional G-L contacting apparatus [50–52]. The important advantages of the porous membrane based G-L contacting are higher mass transfer rates, operational simplicity and easy scale-up [53]. The gas and liquid flow separately in their respective channels allowing manipulating gas and liquid flow rates independently.

Figure 1.3 shows a schematic representation of a typical membrane contacting condition. One fluid phase (gas) remains on one side of the porous membrane and also occupies the pores of the membrane. The second phase (liquid) is on the other side of the porous membrane. In a typical G-L membrane contacting process, the operation in non-wetted condition (gas-filled pores) is more favorable than that in the wetted mode (liquid-filled pores). Such operation gives almost no mass transfer resistance in the membrane. When the differential pressure exceeds the wetting pressure, liquid fills the membrane pores (wetted mode), the mass transfer resistance of the membrane becomes evident leading to unfavorable operation [54]. It is also important that gas to liquid trans-membrane pressure should not exceed the bubbling pressure or else bubbles appear at the liquid side leading to unfavorable operation. In addition to pressure control, the positioning of the stabilized G-L interface can also be achieved

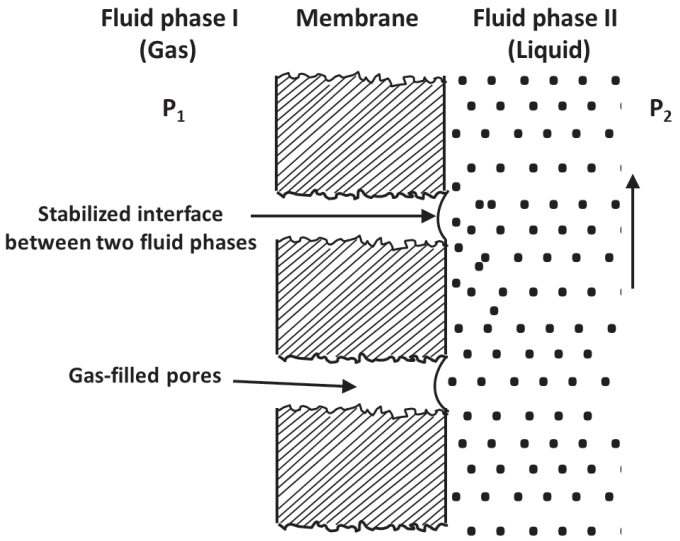

Figure 1.3: Two fluid phases contacting through a stabilized interface in a membrane contactor.

using surface modification (hydrophobization) techniques [28]. Such configurations are prepared with selective hydrophobization methods, in which the membrane support is converted hydrophobic while the catalytic layer remained hydrophilic facilitating a stabilized G-L interface.

Membrane microreactors combine membrane contacting with catalyst immobilization. The solid catalyst surface should be accessible for the reactants from both gas and liquid phases (Fig.1.4). In case of immobilized catalysts on the inner wall of a porous membrane, the solute transport will be severely affected by the internal mass transfer limitations dictated by the porosity and wetting of the catalyst support layer. This requires detailed modeling of convection-diffusion-reaction to calculate mass transfer to a reactive boundary.

1.3.1 Diffusion, adsorption and reaction in microreactors

Laminar flows in microchannels (low Re) typically result in relatively low Pe, which indicates that diffusive mixing occurs at much lower rate than the typical timescales involved for convective fluid flow. The mixing length is proportional to Pe for laminar

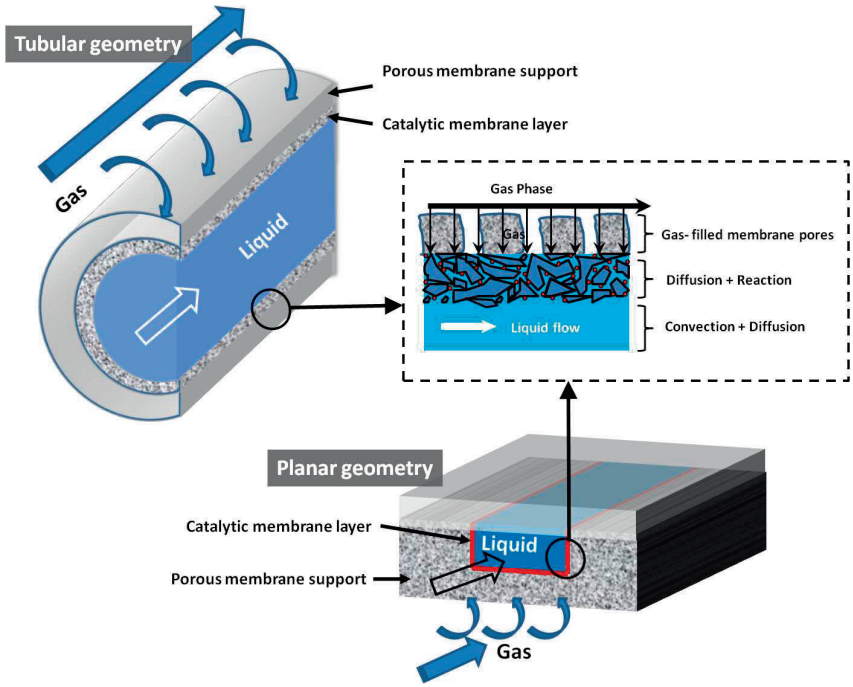

Figure 1.4: Schematic representation of porous membrane microreactor for a gas-liquid reaction over heterogeneous catalysts immobilized over membrane wall.

unidirectional flow, so the mixing length can be in the order of several centimeters. Secondary flows across the microchannel can be generated through inertial effects at moderate *Re* (Dean flows) using patterning of the surface [55] or by surface bounded flow (lid-driven cavity (LDC)) [56]. The most important parameters that affect the interfacial mass transfer rate are shear rate at the interface, boundary conditions of the momentum balance at the interface and the magnitude of the transverse component of velocity relative to the axial component [57]. The interplay between the character of a flow and the resulting interfacial mass transfer influences the efficiency of the reactor [58].

The overall reaction rate in heterogeneously catalyzed reactions depends on the intrinsic kinetics of the chemical reaction together with the external and internal mass transport of the phases involved. The adsorption rate of the solute on the immobilized catalysts on the porous wall is often limiting the overall conversion. The performance of a catalytic membrane microreactor is affected by many factors such as reactor size, catalytic layer thickness, flow regime, interface mass transfer and internal diffusion

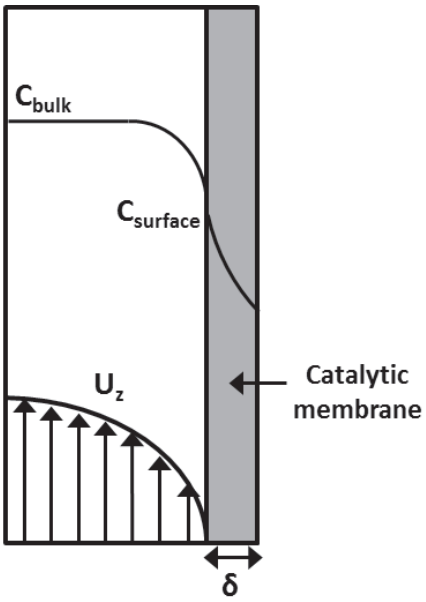

Figure 1.5: Schematic representation of concentration profile in catalytic membrane microreactor.

($D_M = D\varepsilon/\tau$). The internal diffusion depends on the membrane porosity (ε) and tortuosity (τ).

As a result of a reaction taking place in the catalytic layer, the solute concentration becomes depleted near the reactive boundary (Fig. 1.5). This leads to the growth of a concentration boundary layer near the reactive boundary along the reactor. The flux at the interface can be expressed by the mass transfer coefficient and concentration difference:

$$N(z) = k(z)(C_{bulk}(z) - C_{surface}) \tag{1.7}$$

where $N(z)$ is the solute flux to the reactive interface, $k(z)$ is the mass transfer coefficient, $C_{bulk}(z)$ is the local bulk concentration and $C_{surface}$ is the solute concentration at the reactive interface. For a smooth reactor wall, a Leveque scaling is expected, where a depletion layer is formed near the reactive boundary. The thickness of the depletion layer grows axially with a 1/3 power scaling. So, the flux to the stationary

wall decreases axially along the reactor, given by following formula [57]:

$$Sh(z) = 1.62 \left(\frac{z}{dPe} \right)^{-1/3} \tag{1.8}$$

where d is the diameter of the reactor and $Sh(z)$ is the local Sherwood number, which can de defined as:

$$Sh(z) = \frac{k(z)d}{D} = -\frac{N(z)d}{[C_{bulk}(z) - C_{surface}(z)]D} \tag{1.9}$$

When the thickness of the concentration boundary layer becomes similar to the distance between the reactive interface and center of the microchannel, the Sherwood number achieves a constant value and the average concentration decreases with the axial distance along the microchannel. This region is called the fully developed region [57].

Mass transfer in three-dimensional laminar flows has been studied for various cases [59, 60]. Yoon et al. studied several approaches that can be applied to reduce the depletion of solute in the boundary layer in order to increase mass transfer [61]. Two approaches were to introduce intermediate inlets or outlets to deliver fresh solutions to or remove depleted fluid from the main channel, respectively. Another approach was to use herringbone patters in the wall similarly described by Kirtland *et al.* [58]. Gervais and Jensen have studied adsorption to surfaces during steady unidirectional pressure driven flow in microfluidic devices [57]. They have described the performance of microfluidic devices categorizing various regimes of behavior. Lopez and Graham studied the role of shear-induced diffusion in enhancing adsorption and bulk mixing in microfluidic devices [62]. The authors considered Leveque scaling in order to characterize the adsorption on a stationary surface, where a depletion layer is formed near the adsorbing boundary. The thickness of the depletion layer was found to grow axially with a 1/3 power scaling [57].

1.4 Structure of the thesis

The main focus of this thesis is to create an understanding of G-L contacting/reaction in membrane contacting devices. At the microscale, the performance of membrane devices is often limited by the laminar flow and low diffusivity of the solutes in fluid. Therefore, it is necessary to increase the mass transfer rate by modifying the

configurations of the membrane microchannel. There are two crucial questions that we address in this thesis:

- *To what extent fluid flow and geometrical parameters influence the solute transport near the G-L interface in porous membrane micro**contactor** devices?* (Chapter 2-4)
- *What are the critical geometrical and operating parameters that influence the performance of the porous membrane micro**reactors** for heterogeneously catalyzed reactions?* (Chapter 5 and 6)

Both experimental and numerical work was performed to address these questions.

Chapter 2 is devoted to investigate gas uptake in liquid flowing inside a hollow fiber microchannel at different flow velocities. The experiments and numerical analysis were performed in straight and helical microchannels to show G-L contacting efficiency in both geometries. A detailed design and optimization of the microfluidic device is presented that integrates computational fluid dynamics (CFD) with Taguchi method [63] of optimization (based on Design of Experiment). The study details the magnitude of secondary flows in helical microchannel for different operating and geometrical parameters and its influence on microcontactor performance.

Chapter 3 deals with the study of using planar microgrooved hydrophobic membrane surfaces in order to increase the mass transfer rate of gas absorption into the liquid. Two different types of microgrooves have been studied in this work: continuous and non-continuous microgrooves for just mass transfer studies and mass transfer with bulk and surface reactions. The effects of these patterns on the flow behavior and transport of gas into the liquid are analyzed using two-dimensional simulations. The enhancement in flux across the porous membrane has been quantified for varying dimensionless effective slip lengths. The geometrical optimization study was conducted to determine the critical design parameters that influence the performance of the gas-liquid contactor.

In **Chapter 4** a follow-up experimental work of the numerical study described in Chapter 3 is presented. The experiments related to gas uptake, liquid flow patterns and wetting behavior of microgrooved hydrophobic membranes were performed and compared with three-dimensional simulations. Two kinds of configurations, continuous and non-continuous grooves, were fabricated using phase separation microfabrication. These microstructured membranes were tested for G-L contacting experiments. The

flux enhancement was used to characterize the performance of each microcontactor.

Chapter 5 describes a detailed microreactor model and optimization study of a three-phase porous catalytic membrane microreactor. The influence of operating conditions and geometrical parameters, such as liquid flow rates, initial solute concentration and catalytic membrane layer thickness (wetting thickness) on conversion and solute removal rate were studied. The model is validated with experimental observations to verify the correct description of the reaction mechanism. The microreactor performance analysis using adsorption characterization gives detailed understanding of the convection-diffusion-reaction processes taking place at the reactive boundaries for different reactor geometries.

Chapter 6 deals with CFD modeling of a planar photocatalytic microreactor under different reaction and operating conditions. The model integrates convection and diffusion mass transport, chemical reaction kinetics and ultraviolet (UV) light irradiation distribution within the microreactor. The influence of liquid flow rate, initial solute concentration and photocatalytic optical properties on conversion and solute degradation rate were studied. Later, numerical results were validated with experimental observations to confirm the reaction mechanism suggested in literature and to optimize the design parameters.

Finally, **Chapter 7** describes the conclusions of the work presented. Some important aspects of the use of multiphase membrane contactor/reactor are mentioned. The implementation of different approaches in analyzing contactor/reactor under different conditions are discussed. The chapter ends with concluding remarks related to potential implementation of membrane contactors for wider socio-economic benefits, which are relevant for future applications.

1.5 References

[1] W. Ehrfeld, V. Hessel and H. Löwe; *Microreactors: new technology for modern chemistry* (2000); Vch Verlagsgesellschaft Mbh

[2] D. Harrison, J. Hall and H. Rase; *An automatic precision microreactor*; Industrial & Engineering Chemistry **57** (1) (1965) 18–24

[3] O. Wörz, K. Jäckel, T. Richter and A. Wolf; *Microreactors, a new efficient tool for optimum reactor design*; Chemical Engineering Science **56** (3) (2001) 1029–1033

[4] A. de Mello and R. Wootton; *But what is it good for? Applications of microreactor technology for the fine chemical industry*; Lab Chip **2** (1) (2002) 7–13

[5] K. Jähnisch, V. Hessel, H. Löwe and M. Baerns; *Chemistry in microstructured reactors*; Angewandte Chemie International Edition **43** (4) (2004) 406–446

[6] N. De Mas, A. Günther, M. Schmidt and K. Jensen; *Microfabricated multiphase reactors for the selective direct fluorination of aromatics*; Industrial & Engineering Chemistry Research **42** (4) (2003) 698–710

[7] C. de Bellefon, N. Tanchoux, S. Caravieilhes, P. Grenouillet and V. Hessel; *Microreactors for dynamic, high throughput screening of fluid/liquid molecular catalysis*; Angewandte Chemie **112** (19) (2000) 3584–3587

[8] C. De Bellefon, N. Pestre, T. Lamouille, P. Grenouillet and V. Hessel; *High throughput kinetic investigations of asymmetric hydrogenations with microdevices*; Advanced Synthesis & Catalysis **345** (1-2) (2003) 190–193

[9] A. Gross; *Theoretical surface science: a microscopic perspective* (2009); Springer Verlag

[10] H. Fogler; *Elements of Chemical Reaction Engineering* (1998); Prentice Hall International

[11] V. Hessel, P. Angeli, A. Gavriilidis and H. Löwe; *Gas-liquid and gas-liquid-solid microstructured reactors: contacting principles and applications*; Industrial & Engineering Chemistry Research **44** (25) (2005) 9750–9769

[12] A. Günther and K. Jensen; *Multiphase microfluidics: from flow characteristics to chemical and materials synthesis*; Lab Chip **6** (12) (2006) 1487–1503

[13] H. Stone, A. Stroock and A. Ajdari; *Engineering flows in small devices*; Annu. Rev. Fluid Mech. **36** (2004) 381–411

[14] T. Pfohl, F. Mugele, R. Seemann and S. Herminghaus; *Trends in mi-*

crofluidics with complex fluids; Chem.Phys.Chem. **4** (12) (2003) 1291–1298

[15] V. Ajaev and G. Homsy; *Modeling shapes and dynamics of confined bubbles*; Annu. Rev. Fluid Mech. **38** (2006) 277–307

[16] J. Atencia and D. Beebe; *Controlled microfluidic interfaces*; Nature **437** (7059) (2004) 648–655

[17] T. Squires and S. Quake; *Microfluidics: Fluid physics at the nanoliter scale*; Reviews of Modern Physics **77** (3) (2005) 977

[18] N. Shao, A. Gavriilidis and P. Angeli; *Flow regimes for adiabatic gas-liquid flow in microchannels*; Chemical Engineering Science **64** (11) (2009) 2749–2761

[19] K. Jensen; *Microreaction engineering–is small better?*; Chemical Engineering Science **56** (2) (2001) 293–303

[20] R. Dittmeyer, K. Svajda and M. Reif; *A review of catalytic membrane layers for gas/liquid reactions*; Topics in Catalysis **29** (1) (2004) 3–27

[21] A. Utada, E. Lorenceau, D. Link, P. Kaplan, H. Stone and D. Weitz; *Monodisperse double emulsions generated from a microcapillary device*; Science **308** (5721) (2005) 537

[22] H. Maenaka, M. Yamada, M. Yasuda and M. Seki; *Continuous and size-dependent sorting of emulsion droplets using hydrodynamics in pinched microchannels*; Langmuir **24** (8) (2008) 4405–4410

[23] S. Marre and K. Jensen; *Synthesis of micro and nanostructures in microfluidic systems*; Chem. Soc. Rev. **39** (3) (2010) 1183–1202

[24] J. Park, A. Saffari, S. Kumar, A. Günther and E. Kumacheva; *Microfluidic Synthesis of Polymer and Inorganic Particulate Materials*; Annual Review of Materials Research **40** (2010) 415–443

[25] H. Song, D. Chen and R. Ismagilov; *Reactions in droplets in microfluidic channels*; Angewandte Chemie (International ed. in English) **45** (44) (2006) 7336

[26] A. Hibara, S. Iwayama, S. Matsuoka, M. Ueno, Y. Kikutani, M. Tokeshi and T. Kitamori; *Surface modification method of microchannels for gas-liquid two-phase flow in microchips*; Analytical Chemistry **77** (3) (2005) 943–947

[27] J. Kobayashi, Y. Mori, K. Okamoto, R. Akiyama, M. Ueno, T. Kitamori and S. Kobayashi; *A microfluidic device for conducting gas-liquid-solid hydrogenation reactions*; Science **304** (5675) (2004) 1305

[28] H. Aran, J. Chinthaginjala, R. Groote, R. Roelofs, L. Lefferts, M. Wessling and R. Lammertink; *Porous ceramic mesoreactors: A new approach for gas-liquid contacting in multiphase microreaction technology*; Chemical Engineering Journal **169** (1-3) (2011) 239 – 246

[29] M. Losey, M. Schmidt and K. Jensen; *Microfabricated multiphase packed-bed reactors: Characterization of mass transfer and reactions*; Industrial & Engineering Chemistry Research **40** (12) (2001) 2555–2562

[30] M. Losey, R. Jackman, S. Firebaugh, M. Schmidt and K. Jensen; *Design and fabrication of microfluidic devices for multiphase mixing and reaction*; Journal of Microelectromechanical Systems **11** (6) (2002) 709–717

[31] R. Besser, X. Ouyang and H. Surangalikar; *Hydrocarbon hydrogenation and dehydrogenation reactions in microfabricated catalytic reactors*; Chemical Engineering Science **58** (1) (2003) 19–26

[32] R. Chambers, D. Holling, R. Spink and G. Sandford; *Part 13. Gas–liquid thin film microreactors for selective direct fluorination*; Lab Chip **1** (2) (2001) 132–137

[33] N. Miyake and T. Kitazume; *Microreactors for the synthesis of fluorinated materials*; Journal of Fluorine Chemistry **122** (2) (2003) 243–246

[34] A. Rouge, B. Spoetzl, K. Gebauer, R. Schenk and A. Renken; *Microchannel reactors for fast periodic operation: the catalytic dehydration of isopropanol*; Chemical Engineering Science **56** (4) (2001) 1419–1427

[35] G. Maria, A. Marin, C. Wyss, S. Muller and E. Newson; *Modelling and scaleup of the kinetics with deactivation of methylcyclohexane dehydrogenation for hydrogen energy storage*; Chemical Engineering Science **51** (11) (1996) 2891–2896

[36] S. DeWitt; *Microreactors for chemical synthesis*; Current Opinion in Chemical Biology **3** (3) (1999) 350–356

[37] J. Heiszwolf, M. Kreutzer, M. van den Eijnden, F. Kapteijn and J. Moulijn; *Gas-liquid mass transfer of aqueous Taylor flow in monoliths*; Catalysis Today **69** (1-4) (2001) 51–55

[38] M. Kreutzer, F. Kapteijn, J. Moulijn, C. Kleijn and J. Heiszwolf; *Inertial and interfacial effects on pressure drop of Taylor flow in capillaries*; AIChE Journal **51** (9) (2005) 2428–2440

[39] S. Irandoust, S. Ertlé and B. Andersson; *Gas-liquid mass transfer in taylor flow through a capillary*; The Canadian Journal of Chemical Engineering **70** (1) (1992) 115–119

[40] G. Bercic and A. Pintar; *The role of gas bubbles and liquid slug lengths on mass transport in the Taylor flow through capillaries*; Chemical Engineering Science **52** (21-22) (1997) 3709–3719

[41] G. Doku, W. Verboom, D. Reinhoudt and A. van den Berg; *On-microchip multiphase chemistry–a review of microreactor design principles and reagent*

contacting modes; Tetrahedron **61** (11) (2005) 2733–2742

[42] G. Chen, J. Yue and Q. Yuan; *Gas-liquid microreaction technology: Recent developments and future challenges*; Chinese Journal of Chemical Engineering **16** (5) (2008) 663–669

[43] P. De Gennes, F. Brochard-Wyart and D. Quéré; *Capillarity and wetting phenomena: drops, bubbles, pearls, waves* (2004); Springer Verlag

[44] W. Barthlott and C. Neinhuis; *Purity of the sacred lotus, or escape from contamination in biological surfaces*; Planta **202** (1) (1997) 1–8

[45] A. Cassie and S. Baxter; *Wettability of porous surfaces*; Trans. Faraday Soc. **40** (1944) 546–551

[46] R. Wenzel; *Resistance of solid surfaces to wetting by water*; Industrial & Engineering Chemistry **28** (8) (1936) 988–994

[47] W. Deen; *Analysis of transport phenomena* (1998); Oxford University Press New York

[48] O. Vinogradova; *Drainage of a thin liquid film confined between hydrophobic surfaces*; Langmuir **11** (6) (1995) 2213–2220

[49] F. Brochard and P. De Gennes; *Shear-dependent slippage at a polymer/solid interface*; Langmuir **8** (12) (1992) 3033–3037

[50] E. Drioli, A. Criscuoli and E. Curcio; *Membrane contactors: fundamentals, applications and potentialities*; volume 11 (2006); Elsevier Science

[51] K. Sirkar; *Membranes, Phase Interfaces, and Separations: Novel Techniques and Membranes An Overview*; Industrial & Engineering Chemistry Research **47** (15) (2008) 5250–5266

[52] A. Gabelman and S. Hwang; *Hollow fiber membrane contactors*; Journal of Membrane Science **159** (1-2) (1999) 61–106

[53] B. Reed, M. Semmens and E. Cussler; *Membrane contactors*; Membrane Science and Technology **2** (1995) 467–498

[54] H. Kreulen, C. Smolders, G. Versteeg and W. Van Swaaij; *Determination of mass transfer rates in wetted and non-wetted microporous membranes*; Chemical Engineering Science **48** (11) (1993) 2093–2102

[55] A. Stroock, M. Weck, D. Chiu, W. Huck, P. Kenis, R. Ismagilov and G. Whitesides; *Patterning electro-osmotic flow with patterned surface charge*; Physical Review Letters **84** (15) (2000) 3314–3317

[56] J. Koseff and R. Street; *On end wall effects in a lid-driven cavity flow*; Journal of Fluids Engineering **106** (1984) 385

[57] T. Gervais and K. Jensen; *Mass transport and surface reactions in microfluidic*

systems; Chemical Engineering Science **61** (4) (2006) 1102–1121

[58] J. Kirtland, G. McGraw and A. Stroock; *Mass transfer to reactive boundaries from steady three-dimensional flows in microchannels*; Physics of Fluids **18** (2006) 073602

[59] J. Khinast, A. Bauer, D. Bolz and A. Panarello; *Mass-transfer enhancement by static mixers in a wall-coated catalytic reactor*; Chemical Engineering Science **58** (3-6) (2003) 1063–1070

[60] H. Chang and M. Sen; *Application of chaotic advection to heat transfer*; Chaos, Solitons & Fractals **4** (6) (1994) 955–975

[61] S. Yoon, G. Fichtl and P. Kenis; *Active control of the depletion boundary layers in microfluidic electrochemical reactors*; Lab Chip **6** (12) (2006) 1516–1524

[62] M. Lopez and M. Graham; *Enhancement of mixing and adsorption in microfluidic devices by shear-induced diffusion and topography-induced secondary flow*; Physics of Fluids **20** (2008) 053304

[63] A. Atkinson, A. Donev and R. Tobias, editors; *Optimum Experimental Designs*; ISBN978-0-19-929659-0 (2007); New York: Oxford University Press

CHAPTER 2

Gas-liquid contacting in porous helical membrane microcontactor

A revised version of this chapter has been published:

Jigar M. Jani, M. Wessling, Rob G.H. Lammertink *Geometrical influence on mixing in helical porous membrane microcontactors*, Journal of Membrane Science, 378(1-2)351-358, 2011

Abstract

The goal of gas-liquid micromixing has led to develop various kinds of passive micromixer configurations, which can be used for many microfluidics applications. This work details gas-liquid contacting using porous helical microchannels. An experimental and numerical design methodology for different geometrical configurations is presented which systematically integrates computational fluid dynamics (CFD) with an optimization methodology based on the use of design of experiments (DOE) method. The methodology investigates the effect of geometric parameters on the mixing performance of helical membrane microchannel that has design characteristics based on the generation of secondary vortices. The methodology has been applied on different designs of helical hollow fiber geometry at several Reynolds numbers. The geometric features of this microchannel geometry have been optimized and their effects on mixing are evaluated. The flux enhancement and degree of mixing are the performance criteria to define the efficiency of the gas-liquid microchannel contactor for different design requirements. Due to its ease of fabrication, efficiency and operational flexibility, helical membrane micromixers are favorable for gas-liquid contacting, water oxygenation, pervaporation etc.

2.1 Introduction

Process intensification by innovative process design is the preliminary way to achieve less emission, improved chemistry and enhanced process efficiency. Microchemical technology has been widely studied for precise chemical synthesis while achieving downsized chemical plants. This miniaturized chemical plant consists of micromixers, heat exchangers and microreactors.

An important field of application for micromixers is gas-liquid reaction technology, which has attracted great amount of attention in recent years. For gas-liquid reaction, often multiphase catalysis is employed to reduce the reaction temperature and minimize unwanted side products. This type of gas-liquid-solid reaction could be carried out in various types of reactors i.e., dispersed phase reactors, falling film microreactors, micro-packed bed reactors and microreactors with interfaces stabilized by physical structures (membranes, micro-porous plates etc.) [1].

In microfluidic systems, analytical and experimental studies show that capillary forces dominate over the body forces (viscous and pressure forces) existing in the system [2]. In droplet based microfluidics, droplets of the fluids are generated and as they move along the microchannel, an internal flow field is generated. This causes enhanced mixing near gas-liquid interfaces [3–9]. There are numerous studies of physical aspects of droplet microfluidics in microchannels tuning the wetting condition at the wall and the way droplets move in microchannels [10]. Membrane based gas-liquid contacting can be useful to achieve a stable gas-liquid interface [11]. These membrane microreactors contain hydrophobic membrane structures with small pores typically around 50-100 nm. They act as a porous support to facilitate contact between gas and liquid phase. Here, the porous membrane must be non-wettable to ensure that the liquid does not fill the pores. With this approach, gas and liquid will remain in contact with each other at the microchannel wall.

For gas-liquid catalytic reactions using porous membranes, a stable interface can be formed. In such microreactor devices, the gas and liquid reactants have to diffuse to the catalyst surface [12]. For relatively slow reactions, concentration gradients due to transport limitation will be small. For fast reactions, the overall reaction rate will become limited by the transport of reactant from bulk liquid phase to the catalyst surface. In order to achieve high mass transfer rates, mixing in the liquid near the liquid-solid interface is necessary.

Micromixers are classified in two categories: active and passive micromixers. Actuated components in active micromixers require external power to achieve mixing. A passive micromixer makes use of geometrical configuration in order to increase the interfacial area between the fluids which in turn increases the mixing performance. One of the big advantages of passive micromixers is its ease of fabrication and its operational simplicity compared to active micromixer. Different methodologies were adapted for passive micromixers to achieve higher mixing efficiencies [13–15]. A comprehensive knowledge of the underlying physics is very essential for the optimal design of these microdevices.

Typical dimensions of these microdevices are in sub-millimeter range and thus, conventional methods to create mixing are not feasible. The Reynolds number for flow of fluids in these devices is defined as:

$$Re = \frac{du}{\nu} \tag{2.1}$$

where, u is the average flow velocity, d is the characteristic channel dimension and ν is the kinematic viscosity of fluid. Due to very small characteristic dimension of the microchannel and low velocity, Re is very small. This implies that mixing is mainly observed due to molecular diffusion and not mainly by convection.

Further, the Peclet number is defined as:

$$Pe = \frac{du}{D_{mol}} \tag{2.2}$$

where D_{mol} is molecular diffusivity. A typical Pe value in microchannels is 1000 or larger, which indicates that diffusive mixing occurs at much lower rate than the typical timescales involved for convective fluid flow. The mixing length is proportional to Pe for laminar unidirectional flow. Corresponding mixing length can be in the order of several centimeters. This leads to longer microchannels for complete mixing [16]. In several membrane applications, enhanced mixing performance using Dean vortices and generation of secondary flows have already been demonstrated [17]. In helical microchannels, transverse secondary flows arise as a result of the counter acting forces of centrifugal and viscous forces. Centrifugal force depends quadratically on the average velocity, u, while the viscous force depends linearly on u. Therefore, secondary flows get severely dampened at lower velocities. However, at larger fluid velocities (at $Re \geq 10$), centrifugal forces become stronger, promoting the secondary flows. This effect brings advantage to gas-liquid contacting using porous membranes

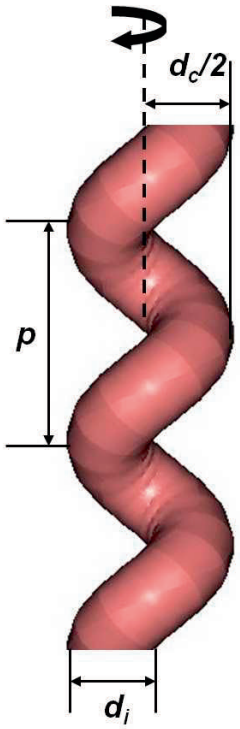

Figure 2.1: Schematic of geometrical parameters of helical microchannel.

as the gas reactant enters from the porous wall. Secondary flows can be induced in curved channels provided that complex 3D geometries are employed [18, 19]. They have determined the parameters that control fluid stirring in the channels with no moving parts. The results of numerical studies indicate the stretching of material lines and three-dimensional trajectories of fluid particles. Their study indicates coupling between chaos in the transverse direction and the non-uniform longitudinal transport of materials. Figure 2.1 shows the geometric parameters of the helical micromixer. The Dean number Dn is commonly regarded as a dimensionless number for flow description in a curved channel. It describes the ratio of centrifugal forces to viscous forces. It also takes into account the geometrical characteristics of the microchannel:

$$Dn = Re\sqrt{\frac{d_i}{d_c}} \tag{2.3}$$

where, d_i is the characteristic channel internal diameter and d_c is the curvature diameter of the curved microchannel. To include the helical pitch effect on the Dean

number, modified helical coiled diameter is taken into account [20]. It is defined as:

$$d_c^{'} = d_c \left(1 + \left(\frac{p}{\pi d_c}\right)^2\right) \tag{2.4}$$

Based on Equation (2.4), the modified Dean number is calculated as:

$$Dn^{'} = Re\sqrt{\frac{d_i}{d_c^{'}}} \tag{2.5}$$

At the beginning of the channel the flow conditions are parabolic and laminar, until it becomes chaotic and influenced by centrifugal forces inducing secondary vortices. An important parameter which defines the developing length θ (^{o}) [21] describing fully developed secondary flow can be written as:

$$\theta = 87.3\left(Dn\frac{d_i}{d_c}\right)^{1/3} \tag{2.6}$$

In many membrane separation processes, these secondary flows are used in order to enhance mass transfer. The study of helical flows and mixing due to chaos in curved geometries has been performed experimentally and numerically [22–24]. The experimental results verify that the mixing effect is deeply related to the structure of helical flow patterns formed inside the micromixer [25]. They also quantified the mixing with different flow parameters. Several numerical and experimental studies have been performed to study the efficiency of helically wound hollow fiber modules [26–29]. They have compared the limiting flux, energy consumption and the effect on mass transfer by shear stress in helical hollow fibers. The relationship between variations in local velocity components and wall shear stress has been established. That allowed authors to observe the evolution of Dean vortices induced by flow and geometry variations.

To date, there have been a number of theoretical, experimental and numerical studies aimed at the optimization of twisted and grooved micromixers [19, 30–32]. However, systematic design and optimization approach for gas-liquid contacting in porous helical membrane contactor was not performed till date and this research aims to address this problem. This work also aims to present quantification of total gas uptake in liquid numerically and experimentally for different module configuration. In this study,

gas uptake experiments and numerical analysis were performed for liquid flowing inside various microchannels at different flow velocities. A detailed experimental and numerical approach for design and optimization of micromixers is presented that integrates computational fluid dynamics (CFD) with Taguchi method [33] of optimization (based on Design of Experiment). The experimental and numerical study covers the magnitude of secondary flow in helical microchannel for different operating and geometrical parameters, where optimized parameters can be used to optimize flow within this membrane micromixer.

2.2 Experimental

2.2.1 Materials

Pure oxygen and nitrogen were obtained from Praxair, Belgium. Demineralized water was used for the operation.

2.2.2 Module preparation and fluidic setup

The hollow fiber membranes used in micromixer modules were composed of porous, microfiltration Accurel S6/2 polypropylene (PP) - purchased from Membrana GmbH (Germany). These fibers had an outer diameter of 2.7 mm, an inner diameter of 1.8 mm and according to the supplier an average pore size of 0.27 μm. Two kinds of micromixer modules were prepared: straight and helically wound. The micromixer module was housed into a glass tubing. The circular glass shell has inlet and outlet ports for the connections. The fiber was tied at regular intervals around the glass rod and later placed into the glass shell. The fiber, at the ends of the glass tubing, was

Table 2.1: Generalized geometrical dimension for gas-liquid micromixer module used in experiments

Geometric parameters	Dimensions (mm)
Channel length	180
Channel internal diameter	1.8
Helical pitch	40
Helical curvature diameter	2.5
Average pore size (μm)	0.27
Membrane thickness	0.45

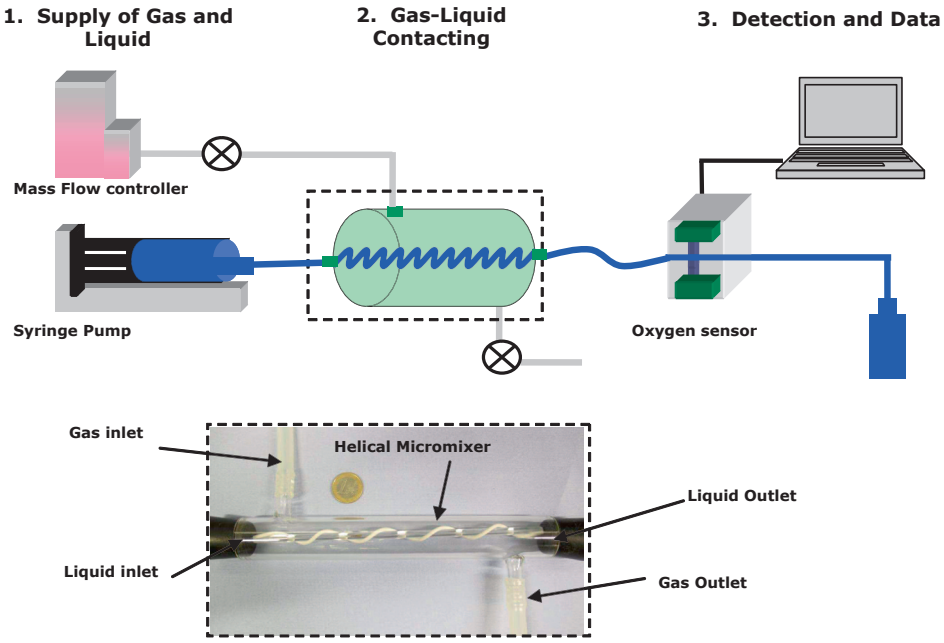

Figure 2.2: Schematic representation of experimental setup used for O_2 uptake into water.

glued using polyurethane glue. The helically wound hollow fiber module was prepared manually adjusting curvature diameter and helical pitch on glass rod with regularly spaced ties on it. The geometrical specifications for the helically wound and straight hollow fiber modules were shown in Table 2.1.

Figure 2.2 displays schematic representation of the experimental setup for hollow fiber membrane micromixer module. The setup consists of a programmable syringe pump (Harvard Apparatus, accuracy within 0.35% and reproducibility within 0.05%), an oxygen sensor (PreSens Fibox 3, accuracy ±0.15% air saturation at 1% air-saturation, resolution 1 ±0.05% air-saturation), mass flow controller (Bronkhorst, accuracy ±0.5% of reading plus ±0.1% full scale) and a PC for the data acquisition. PEEK tubings (3.175 mm OD, P-1534) and fittings (3.175 mm OD, P-100) from Upchurch Scientific were used for the connections.

2.2.3 Gas-liquid contacting experiments

To evaluate the performance of micromixer under different geometrical conditions, the hollow fiber membrane module was subjected to different flow conditions. The feed

water was injected at flow rates ranging from 0.05 mL/min to 10 mL/min through the lumen side of the fiber. Pure oxygen was supplied to the shell of the glass tubing.

The feed water was continuously bubbled with inert nitrogen gas (in a separate vessel) in order to remove the oxygen. For maintaining consistency in terms of any leakage in the module, for all experiments, the oxygen content in liquid outlet (without the supply of oxygen) was monitored. Apart from that, the oxygen content in degassed water was also monitored continuously directly using oxygen sensor. The driving force for the oxygen transfer varies with the axial position in the module and it drops along the length of the micromixer. An expression for the overall oxygen flux at the microchannel outlet, N, can be expressed by:

$$N = \int \frac{4Q(r) \cdot C(r)dr}{\pi d_i^2} \tag{2.7}$$

where, $Q(r)$ and $C(r)$ are liquid flow rate and oxygen concentration, respectively. Hollow fiber radius and internal diameter of the microchannel are denoted as r and d_i, respectively. The experiments were carried out at ambient pressure and temperature conditions.

2.3 Numerical analysis

For detailed understanding of fluid flow, mixing and micromixer performance, computational fluid dynamics (CFD) simulations were performed using COMSOL Multiphysics 3.5. Gas-liquid contacting in porous helical microchannels was modeled incorporating different geometrical parameters. All simulations were performed in steady state for three-dimensional mode. For optimum computational power, convergence and accuracy, the unstructured tetrahedral mesh was varied between 215,000 to 250,000 elements (Lagrange type p2, p1), depending upon the dimension of the microchannel. The mesh has been refined until the numerical observations were consistent. The mesh size was smaller near the membrane wall to capture concentration variations accurately. Tetrahedral mesh does not pose any constraints on the structure of the geometry. Hence, it can be used to mesh sharp curvatures of the helical geometry. The accuracy of the result was further be increased by adjusting geometry resolution. This numerical model solves the Navier-Stokes equation coupled with convection-diffusion equation using the finite element method. The governing equations are represented as

follows:

$$\nabla \cdot u = 0 \tag{2.8}$$

$$\rho[(u \cdot \nabla)u] = -\nabla P + \eta \nabla^2 u \tag{2.9}$$

$$D\nabla^2 c = u \cdot \nabla c \tag{2.10}$$

Here, ρ and η are the density and viscosity of the liquid and D is the diffusion coefficient. Pressure, oxygen concentration and time are denoted as P, c and t, respectively. Physical absorption of oxygen into water is selected as the test case. Water is flowing inside the microchannel and oxygen diffuses through the porous membrane. Geometrical dimensions of the helical micromixer for CFD studies were kept same as the experimental module (shown in Table 2.1). The physical properties of the gas and liquid at 20°C are mentioned in the Table 2.2.

Table 2.2: Properties of the fluids at $20^{\circ}C$

Fluid	Density (kg/m^3)	Viscosity ($kg/m \cdot s$)	Diffusivity in water (m^2/s)
Water	9.98×10^2	0.9×10^{-3}	-
Oxygen	1.429	0.20×10^{-6}	2.00×10^{-9}

For the boundary conditions, a fully developed parabolic flow profile has been implemented at the microchannel inlet and the outlet is kept at normal pressure. There will be zero oxygen concentration at the microchannel inlet and convective flux will be implemented at the outlet boundary. The wall boundary conditions are defined as follows:

1. For Navier-Stokes application mode, wall velocities will be zero (no-slip condition).
2. For Convection-diffusion application mode, saturated wall boundary condition will be implemented to simulate gas uptake through the hydrophobic porous wall.

The mixing cup concentration of absorbed gas into the liquid from the microchannel

outlet was compared with the experimental results.

2.4 Optimization method

It is essential to choose appropriate design parameters and their range of variations for proper description of the design objective. Mixing index or mixing intensity is the major performance parameter for the design of any micromixer. This quantification is possible by calculating the variance of the component in the micromixer. The variance σ and mixing index M of the species concentration on the cross-section normal to the flow direction are defined as:

$$\sigma = \sqrt{\frac{1}{m}\sum (c - c_\infty)^2} \tag{2.11}$$

$$M = 1 - \frac{\int_A |c - c_\infty|\, dA}{\int_{A_0} |c_0 - c_\infty|\, dA} \tag{2.12}$$

where, m is the number of the sample points for a given cross-section, c is the local (area element) value of the concentration of one fluid species on the selected cross-section plane A, c_0 is the local concentration at the inlet plane A_0 (which is zero) and c_∞ is the concentration of complete mixing (mixture steady-state concentration). The mixing index is 1 for complete mixing and 0 for no mixing.

One of the important factors affecting the precision of the design methodology is the choice of geometrical design variables and its variation range. Taguchi method of optimization is based on Orthogonal Array (OA) experiments and gives reduced variance for the well-balanced experiment with optimum settings of parameters. Principally, some preliminary tests are necessary for sensitivity analysis which gives tentative range of design variable before proceeding towards detailed design. An experimental table of 9 designs was formulated by using the OA L_9 of the Taguchi method. The orthogonal array showing L_9 formulation is shown in Table 2.3. To realize this formulation, three design parameters with three levels were chosen. Table 2.4 shows the ranges and values of the geometrical design parameters taken in our study. For all models used in the optimization study, the total length of microchannels is fixed at 60 mm.

The mixing of gas into the liquid in these 9 different designs were studied by CFD

analysis at various Reynolds numbers. For evaluating the influence of the design parameters on mixing index, Taguchi method's Signal-to-Noise ratios (S/N) are used.

Table 2.3: Orthogonal Array (OA) L_9

Design of Experiments (DOE) for CFD studies	Design parameters		
	A	B	C
1	1	3	3
2	1	1	1
3	1	2	2
4	2	3	1
5	2	1	2
6	2	2	3
7	3	3	2
8	3	1	3
9	3	2	1

The S/N ratios are defined as log functions of the desired output which can help understanding the desired output and detailed data analysis. In order to calculate S/N Ratio from the simulation results, Equation (2.11) is used at the outlet of the microchannel which can be later used in Equation (2.13):

$$n = \frac{S}{N} = -10log(\frac{1}{\sigma^2}) \tag{2.13}$$

Table 2.4: Design parameters and levels used in OA L_9 (all values shown in the table are in mm)

Levels	Factors		
	Curvature diameter A	Helical pitch B	Internal diameter C
1	2.5	20	1.0
2	3.5	30	1.5
3	4.5	40	2.0

For the optimal output for the performance parameter, S/N ratio should be maximized. The mean of S/N ratios of the design experiments of OA L_9 were calculated to evaluate the contribution of each level to the mixing index.

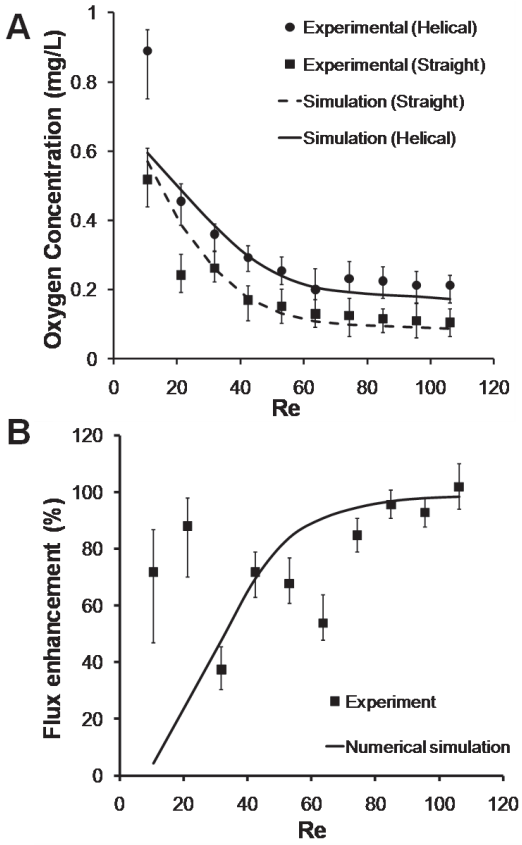

Figure 2.3: *Oxygen uptake* (A) Oxygen outlet concentration against Re (B) Flux enhancement *vs* Re; experimental values are shown in dots and simulation values are shown in line.

2.5 Results and discussion

2.5.1 Description of the system

Straight and helical membrane modules were fabricated using Accurel S6/2 polypropylene (PP) hollow fibers. Water is flowing inside the hollow fiber microchannel and oxygen is continuously fed at the shell side. This allows oxygen transport across the membrane from the shell side to the water. The outlet oxygen concentration in the water was constantly monitored by an oxygen sensing probe.

2.5.2 Oxygen uptake

Oxygen uptake in porous membrane microchannels was evaluated by both oxygen absorption experiments and COMSOL simulations. To study the effect of helical microchannel geometry, a helical microchannel was compared with an equivalent length (180 mm) of a straight porous microchannel module. Figure 2.3A displays outlet oxygen concentrations of straight and helical microchannels for both experiments and simulations (oxygen saturation concentration is 40 mg/L at 25°C and 1 bar). The outlet oxygen concentration in helical hollow fiber modules is higher than the straight ones. For low *Re* (below 5), the liquid gets saturated almost completely. The experimental results obtained at lower *Re* are showing little variations than numerical observations. This difference can be explained by the experimental error incurred due to oxygen sensor sensitivity at low liquid flow rates. The overall flux enhancement in a helical microchannel compared to the straight channel is shown in Fig.2.3B. The results, both from the COMSOL models and oxygen absorption experiments, show higher oxygen absorption for the helical microchannel compared to the straight channel.

As liquid flows at higher *Re* through the helical microchannel, the secondary flow perpendicular to the flow direction increases. This counter-rotating recirculation along the microchannel induces more gas absorption compared to the straight microchannel. It has been observed that with the secondary flow in helical microchannel at higher *Re* (above 60), more than 80 % enhancement in overall flux can be obtained compared to the straight channel.

2.5.3 Mixing in helical membrane microchannel

Numerical simulations were performed to study mixing and mass transfer in helical microchannel. Figure 2.4 shows the mixing index for a helical microchannel (d_c = 1.5 mm, p= 15 mm, d_i = 1.0 mm) and a straight microchannel for different values of Reynolds number (0.5-150). At lower *Re* (higher residence time), gas will diffuse till the center of the microchannel and the liquid will get saturated with gas within a few millimeters of channel length. As *Re* is increased the residence time gets shorter, which reduces dissolution of gas into the liquid for both geometries. In a straight microchannel gas uptake will be purely based on the diffusion and an increase in *Re* leads to drop in mixing. However, when *Re* is increased, the helical microchannel

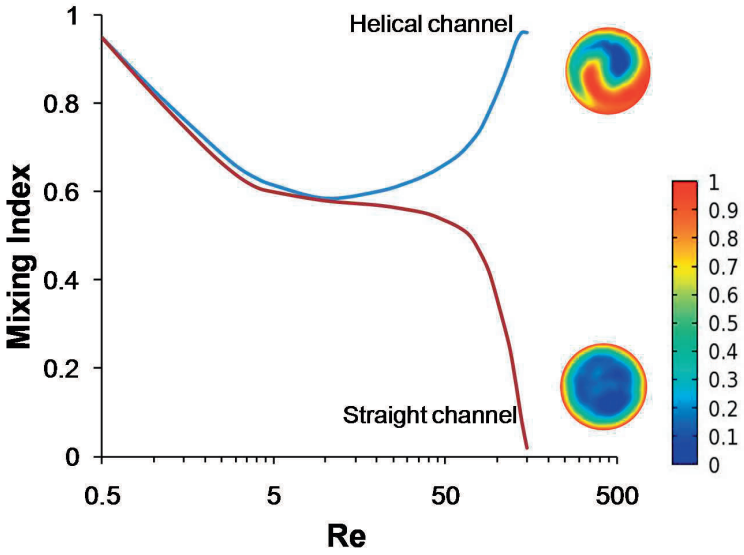

Figure 2.4: *Mixing using helical microchannels.* Mixing index vs Re comparing helical microchannel (d_c = 1.5 mm, p = 15 mm, d_i = 1.0 mm) with equivalent length of straight channel. Also showing simulation results of outlet oxygen concentration distribution at Re = 100 for both helical and straight microchannel.

will induce Dean effect. It is observed from the Figure 2.4 that, at higher Re for the same values of internal diameter and microchannel length, the mixing in a helical microchannel is enhanced compared to a straight microchannel.

It is evident from the numerical simulations that the curved geometries, because of their specific design, trigger transverse secondary Dean flows as a result of interplay between inertial and centrifugal forces. The intensity for such secondary flows increases as fluid is pushed back from the outer wall to the inner wall of the microchannel at higher liquid velocities as previously demonstrated by Moulin et al.[26] by means of laser visualization. At lower flow rates ($Re < 3$), secondary flows are not dominant so that it can perturb the parabolic laminar flow.

The degree of mixing increases along the axial flow direction for the helical microchannel compared to the straight channel at $Re = 50$ (Fig.2.5A). The mixing index at the outlet of the microchannel clearly demonstrates enhanced mixing in the helical microchannel. Figure 2.5B displays the axial and radial in plane velocity profile at constant Reynolds number (Re= 50) for three different geometries. The velocity changes (for fully developed secondary vortices) is observed around $\theta = 240^o$ for helical channel (d_c

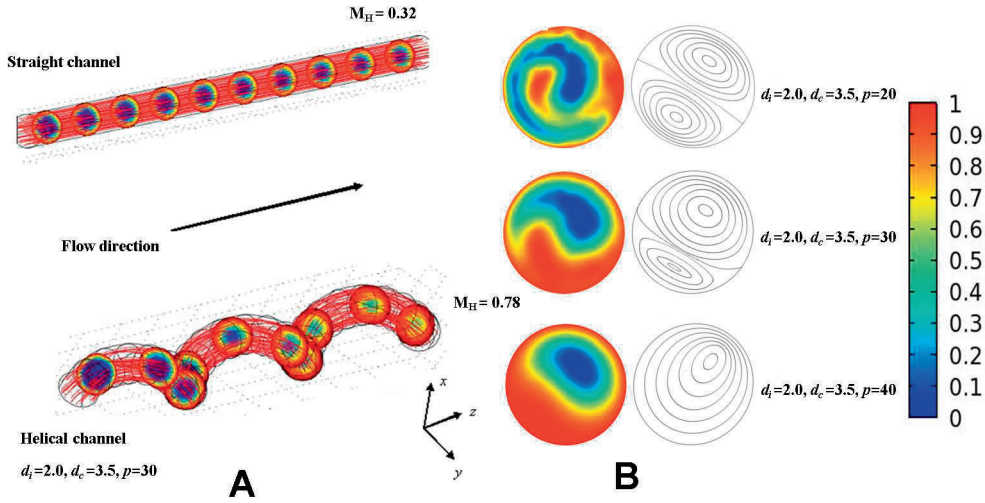

Figure 2.5: Comparison of concentration distribution between helical and straight microchannel (A) axial concentration profile (B) cross section concentration plot (on left) after first rotation (360°) and velocity contours (on right) for three different geometries.

= 3.5 mm, p= 20 mm, d_i = 2.0 mm). The developing length calculated based on Equation (2.6), for the same flow conditions and geometry, gives $\theta = 243.11^o$ as developing length, which is in good agreement with numerical results. Two counter rotating vortices are observed at lower helical pitch (Re = 50, Dn = 37). For higher helical pitch (40 mm), the axial velocity profile is pseudo-parabolic and there are only small rotating vortices in the secondary flow. When the helical pitch is decreased, the velocity profile also changes. At the identical Reynolds number, for smaller pitch (also for curvature diameter), the representation of axial velocity (orthogonal to the flow direction) suggests that slowly the flow gets away from the center of the channel towards the inner wall of the microchannel.

2.5.4 Optimization of geometrical parameters

The effects of curvature diameter, helical pitch and internal diameter were investigated numerically. The application of optimization study using an orthogonal array gave the influence of the design parameters on performance criterion-mixing index. To evaluate the contribution of each level of a design parameters on the S/N ratio of the mixing index, the mean of the S/N ratios of the experiments in the OA L_9 is

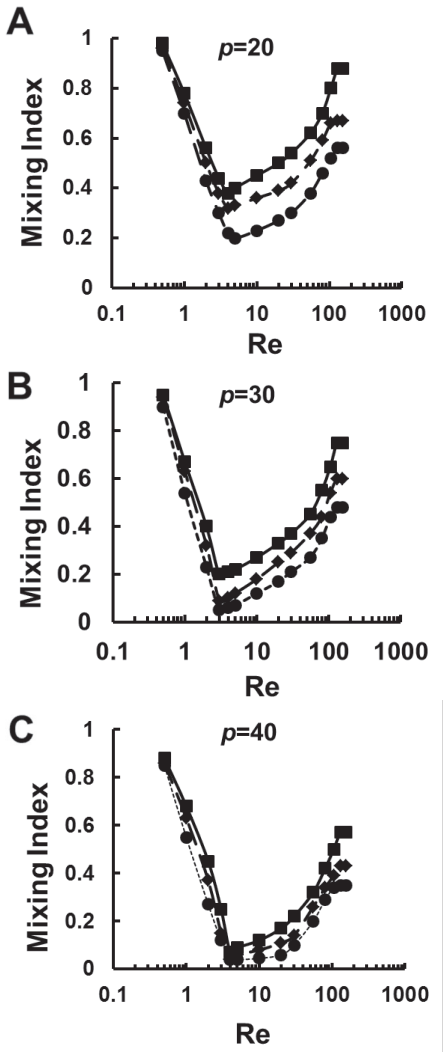

Figure 2.6: Influence of helical pitch and curvature diameter on mixing at different flow rates. ■ shows results of d_c =2.5 mm, d_i =2.0mm, ♦ represents d_c =3.5 mm, d_i =2.0mm and ● shows d_c = 4.5 mm, d_i =2.0 mm for (A) p= 20mm (B) p=30mm (C) p=40 mm.

calculated according to Equation (2.13). According to the definition of S/N ratio, larger-the-better was the constraint in selecting the crucial parameters. The mixing index for equal residence time in different geometries at a wide range of Reynolds numbers is plotted in Figure 2.6.

The optimization study gave the optimal geometry for improved gas-liquid contacting in a porous helical membrane modules. Mixing index of the optimal geometry was compared to different microchannel geometry configurations. It can be seen that the mixing index at very low Re ($\sim$0.5, high residence time) is near unity due to saturation of the gas into the liquid. As the Reynolds number increases (lower residence time), the mixing index drops gradually to a minimum (different minimum for different geometries) for all geometries. This is due to lower amount of gas uptake into the liquid (owing to shorter residence time). However, after this critical Reynolds number ($Re = 3$, $\mathrm{Dn}^{'} = 0.42$), two counter rotating secondary vortices start to develop because of the Dean effect. This results are also confirmed with previous work of Moulin et al. [28], which showed that secondary vortices can be observed at such very low flow rates ($Re = 1$, $\mathrm{Dn}^{'} = 0.4$). These secondary flows enhance gas absorption near the gas-liquid interface. This effect provokes gas absorption when Reynolds number is further increased which leads to further enhancement in the gas uptake. This can be seen as an increase in the mixing index in Figure 2.6.

It is evident (Fig.2.6A) that the smallest helical pitch (20 mm) gave maximum mixing at any given Re. Recirculation inducing transversal velocity that instantaneously transports absorbed gas from the gas-liquid interface to the center of the microchannel. It is also very clear (Fig.2.6A,B and C) that mixing increases with increased curvature. The microchannel with higher curvature pushes liquid from the outer wall towards the inner wall faster than the microchannel with smaller curvature. It is also interesting to see from the plots in Fig. 2.6 that for the smaller pitch (20 and 30 mm), the minimum in the mixing index for different design configurations is distinct and separate. The minimum of mixing index for the optimized geometry is higher than the other configurations. However, as the helical pitch is increased (40 mm), the distinctive nature is less pronounced. This is because of dampened Dean effect due to the larger helical pitch. This clearly shows that in order to achieve higher mixing, both helical pitch and curvature diameter should be reduced.

The influence of internal diameter on mixing is shown in Fig. 2.7. The micromixers with larger diameters (2.0 mm) show lower gas uptake at lower range of Re, this is because of a longer diffusion path. At higher Re, as the internal diameter of the microchannel increases, the mixing effect also increases due to centrifugal force acting on the fluid element near the microchannel wall. The reason for this can be the centrifugal force acting on the fluid near the channel wall that is higher than the fluid element near the center of the channel. And as the channel radius increases,

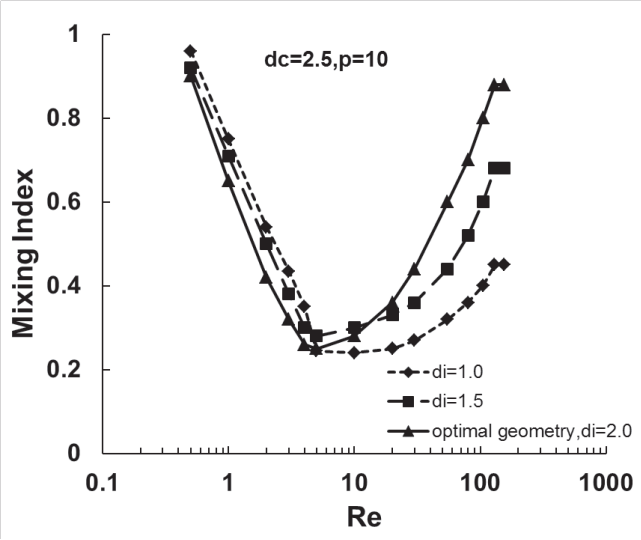

Figure 2.7: Mixing index *vs* Re for helical microchannel with with different internal diameter for $d_c = 2.5$ mm, $p = 10$ mm.

recirculation near the channel wall increases. This leads to higher gas uptake in the liquid near the microchannel wall. This explains the increase in the mixing for increasing the micromixer internal diameter. Thus, according to Fig. 2.6 and 2.7, it can be deduced that A1B1C3 is the optimized geometry giving the highest mixing. However, this optimized design is located in the constraints set for the experimental conditions. Improved design methodology with wider range of critical design parameters is warranted in order to study entire design space.

2.6 Conclusions

One of the main goal of the this work was to optimize a gas-liquid micromixer that was fairly simple, efficient and easy to operate. This way a new concept for gas-liquid contacting in porous helical membrane microchannels has been developed. It was demonstrated that helical structures perform more effectively compared to the straight microchannel. This has been analyzed using both numerical and experimental methods.

The oxygen uptake experiments were performed in straight and helical microchannel to show gas-liquid contacting efficiency in both geometries. The helical design geometry

has been exploited to produce secondary flows in microchannels. This significantly reduces complex micromixer fabrication methods and need for auxiliary equipments. This work clearly shows that the measured gas uptake in liquid flowing inside helical membrane microchannel was higher compared to the straight microchannel. Flux enhancement was more than 80 % in helical microchannel compared to the straight channel for Reynolds number more than 60. It also suggests that the flux enhancement is not only dependent on Reynolds number but it also depends strongly on the geometrical configuration of the microchannel.

The numerical study was performed on detailed optimization to study the influence of geometrical parameters on the performance of gas-liquid helical microcontactors and to maximize the mixing. The objective was to maximize the mixing index using three design variables. i.e., the curvature diameter, helical pitch and channel internal diameter. The design parameter sensitivity analysis suggested that mixing is more sensitive to the curvature diameter and helical pitch. Increase in internal diameter of the microchannel increases mixing because of pronounced Dean effect due to centrifugal force. The results from geometric optimization and numerical study showed that the degree of mixing has been significantly improved with modification of the channel curvature diameter and helical pitch. The obtained results are relevant for detailed understanding of gas-liquid contacting applicable to membrane based processes, where the knowledge of optimization of hollow fiber geometry provides useful information which can be implemented to overcome mass transport problems.

2.7 Acknowledgments

This work was financially supported by Stichting voor de Technische Wetenschappen (STW, Project 07569). The authors also greatly acknowledge H.C.Aran and D.Salamon for fruitful discussions.

2.8 References

[1] V. Hessel, P. Angeli, A. Gavriilidis and H. Löwe; *Gas-liquid and gas-liquid-solid microstructured reactors: contacting principles and applications*; Industrial & Engineering Chemistry Research **44** (25) (2005) 9750–9769

[2] C.J.Kim; Proc. Symp. Micromachining and Microfabrication page 4177

[3] T. Thorsen, R. Roberts, F. Arnold and S. Quake; *Dynamic pattern formation in a vesicle-generating microfluidic device*; Phys. Rev. Lett **86** (2001) 4163–4166

[4] S. Anna, N. Bontoux and H. Stone; *Formation of dispersions using flow-focusing in microchannels*; Appl.Phys.Lett **82** (3) (2003) 364

[5] P. Garstecki, I. Gitlin, W. DiLuzio, G. Whitesides, E. Kumacheva and H. Stone; *Formation of monodisperse bubbles in a microfluidic flow focusing device*; Appl.Phys.Lett **85** (13) (2004) 2469

[6] R. Dreyfus, P. Tabeling and H. Willaime; *Ordered and Disordered Patterns in Two-Phase Flows in Microchannels*; Phys. Rev. Lett **90** (2003) 14

[7] H. Song, J. Tice and R. Ismagilov; *A Microfluidic System for Controlling Reaction Networks in Time*; Angew. Chem. **115** (7) (2003) 792–796

[8] S. Sugiura, M. Namajima, S. Iwamoto and M. Seki; *Interfacial Tension Driven Monodispersed Droplet Formation from Microfabricated Channel Array*; Langmuir **17** (2001) 5562–5566

[9] Q. Xu and M. Nakajima; *The generation of highly monodisperse droplets through the breakup of hydrodynamically focused microthread in a microfluidic device*; Appl.Phys.Lett **85** (17) (2004) 3726–3728

[10] P. Tabeling; *A brief introduction to slippage, droplets and mixing in microfluidic systems*; Lab Chip **9** (2009) 2428–2436

[11] J. de Jong, M. Geerken, R. Lammertink and M. Wessling; *Porous Microfluidic Devices–Fabrication and Applications*; Chemical Engineering & Technology **30** (3) (2007) 309–315

[12] H. Fogler, editor; *Elements of Chemical Reaction Engineering*; 3 edition (1999); New Jersey: Prentice Hall and Englewood Cliffs

[13] V. Hessel, H. Löwe and F. Schönfeld; *Micromixers: a review on passive and active mixing principles*; Chem.Eng.Sci **60** (2005) 2479–2501

[14] A. Gavriilidis, P. Angeli, E. Cao, K. Yeong and Y. Wan; *Technology and Applications of Microengineered Reactors*; Trans. IchemE **80** (part A) (2002) 3–30

[15] N. Nguyen and Z. Wu; *Micromixers-A review*; J.Micromech. and Microeng. **15** (2) (2005) R1–R16

[16] A. Sudarshan and V. Ugaz; *Fluid mixing in planar spiral microchannels*; Lab Chip **6** (2006) 74–82

[17] H. Winzeler and G. Belfort; *Enhanced performance for pressure-driven membrane processes: The argument for fluid instabilities*; J. of Memb. Sci. **80**

(1993) 35–47

[18] H. Aref, S. Jones, S. Mofina and I. Zawadski; *Vortices, kinematics and chaos*; Physica D **37** (1989) 423–440

[19] S. Jones, O. Thomas and H. Aref; *Chaotic advection by laminar flow in a twisted pipe*; Journal of Fluid Mechanics **209** (1989) 335–357

[20] P. Mishra and S. Gupta; *Momentum transfer in curved pipes. 1. Newtonian fluids*; Industrial & Engineering Chemistry Process Design and Development **18** (1) (1979) 130–137

[21] L. Austin and J. Seader; *Fully developed viscous flow in coiled circular pipes*; AIChE Journal **19** (1) (1973) 85–94

[22] F. Jiang, K. Drese, S. Hardt, M. Küpper and F. Schönfeld; *Helical flows and chaotic mixing in curved micro channels*; AIChE journal **50** (9) (2004) 2297–2305

[23] S. Kim and S. Lee; *Measurement of Dean flow in a curved micro-tube using micro digital holographic particle tracking velocimetry*; Experiments in Fluids **46** (2) (2009) 255–264

[24] A. Gigras and S. Pushpavanam; *Early induction of secondary vortices for micromixing enhancement*; Microfluidics and Nanofluidics **5** (1) (2008) 89–99

[25] S. Schnabel, P. Moulin, Q. Nguyen, D. Roizard and P. Aptel; *Removal of volatile organic components (VOCs) from water by pervaporation: separation improvement by Dean vortices*; Journal of membrane science **142** (1) (1998) 129–141

[26] P. Moulin, J. Rouch, C. Serra, M. Clifton and P. Aptel; *Mass transfer improvement by secondary flows: Dean vortices in coiled tubular membranes*; Journal of membrane science **114** (2) (1996) 235–244

[27] R. Moll, D. Veyret, F. Charbit and P. Moulin; *Dean vortices applied to membrane process - Part II: Numerical approach*; J. of Memb. Sci. **288** (1-2) (2007) 321–335

[28] P. Moulin, D. Veyret and F. Charbit; *Dean vortices: comparison of numerical simulation of shear stress and improvement of mass transfer in membrane processes at low permeation fluxes*; J. of Memb. Sci. **183** (2) (2001) 149–162

[29] J. Ghogomu, C. Guigui, J.C.Rouch, M. Clifton and P. Aptel; *Hollow-fibre membrane module design: comparison of different curved geometries with Dean vortices*; J. of Memb. Sci. **181** (1) (2001) 71–80

[30] N. S. Lynn and D. Dandy; *Geometrical optimization of helical flow in grooved micromixers*; Lab Chip **7** (2007) 580–587

[31] C. Cortes-Quiroz, M. Zangeneh and A. Goto; *On multiobjective optimization of geometry of staggered herringbone micromixer*; Microfluidics Nanofluidics **7** (1) (2009) 29–43

[32] A. Mouza, C.-M. Patsa and F. Schönfeld; *Mixing performance of a chaotic micro-mixer*; Chem.Eng.Research and Design **86** (10) (2008) 1128–1134

[33] A. Atkinson, A. Donev and R. Tobias, editors; *Optimum Experimental Designs*; ISBN978-0-19-929659-0 (2007); New York: Oxford University Press

CHAPTER 3

Enhanced gas uptake by a microgrooved membrane

A revised version of this chapter has been prepared for publication:

Jigar M. Jani, J. Ensink, M. Wessling, Rob G.H. Lammertink *Enhanced gas uptake by a microgrooved membrane*

Abstract

A detailed numerical study is presented which focuses on flow behavior and gas uptake of liquid along microgrooved hydrophobic membranes. We demonstrate that such microgrooved membrane surfaces gives rise to a higher gas-liquid interface velocity compared to flat surfaces. The effects of these grooves on the flow behavior and gas transport into the liquid are analyzed. The flux enhancement across the porous membrane has been quantified for varying effective slip lengths and increases linearly with shear-free gas-liquid interface. The effects of diffusion time, reaction rate constant and residence time on the flux enhancement are quantified for varying dimensionless slip velocity. A detailed comparison has been made between continuous and non-continuous micropatterns to examine their effectiveness in terms of flux enhancement across a hydrophobic membrane. A numerical design method for different geometrical configurations is presented which systematically integrates computational fluid dynamics (CFD) with an optimization based on the design of experiments (DOE). The method investigates the effect of geometric parameters on the performance of microgrooved membranes which allows to optimize its operation.

3.1 Introduction

The broad application of microfluidic devices has great potential for various industries i.e. micro total analysis systems, miniaturized cell-biological systems, flow in microreactors and flow through porous media [1–3]. Due to the small characteristic length scales, microfluidic devices offer many advantages over conventional reactors and heat/mass transfer apparatus [4].

An important application for these microfluidic devices concerns gas-liquid contacting. There are mainly three ways to achieve intense gas-liquid contacting at macroscale: gas bubbles dispersed in the liquid, liquid droplets dispersed in the gas or a thin liquid film in contact with the gas [4]. Another interesting approach to achieve gas-liquid contacting uses membrane based microfluidic devices [5–8].

The necessity to efficiently induce microscopic mixing is an essential requirement for these devices, and it is the subject of intense research in the microfluidic field. Since the flow is mainly laminar ($Re < 1$), inertial effects (turbulence etc.) are not dominant, so mixing of fluids mainly relies on molecular diffusion. Chaotic behavior in fluids is possible even at very low Reynolds numbers. This often requires essential combinations of both convection and diffusion in order to reduce the mixing time and length [4, 9–12].

In order to enhance mixing, either active or passive methods can be employed. Active mixing can be achieved by periodically creating instabilities in the flow field, e.g. by pressure perturbation [13], thermal power [14], electrokinetic force [15] and ultrasonic actuation [16]. Active micromixers have disadvantages of using external power sources and adding complexity in terms of device fabrication, operation and maintainance. Passive micromixers, on the other hand, utilize no additional power sources other than the principal pressure drop used for the fluid flow. There have been many configurations developed and studied for passive mixing, including splitting and recombining [17], serpentine channels [11], T-type mixers [18], and helical and meander channels [19, 20].

A micropatterned surface on the channel wall can also affects the flow and thereby the mixing, e.g. the staggered herringbone microchannel (SHM) [10], oblique wells with different angles and depths [21], superhydrophobic surfaces or micropatterns on channel walls [22]. There have been experimental and numerical studies to investigate the use of patterned superhydrophobic surfaces to promote micromixing [23, 24].

The hydrophobicity prevents liquid from wetting the grooves and entraps air in the patterns. This gives a shear-free gas-liquid interface between the ridges, which reduces the drag. Using microparticle image velocimetry (micro-PIV) and CFD simulations, Ou et al. reported a reduction in pressure drop up to 40 % [24]. Maynes et al. [25] showed experimental and numerical results for laminar flow through a microchannel with superhydrophobic surfaces incorporating grooves aligned parallel to the flow direction. Their numerical predictions showed that the effective slip length increases with increasing relative cavity width and depth, and decreasing relative microrib/cavity module length [25]. Watanabe et al. examined the laminar flow in a circular pipe and two coaxial cylinders with hydrophobic coated walls [26]. They reported 14% and 12% drag reduction in two respective cases. Tsai et al. used microparticle imaging velocimetry to estimate effective slip lengths when water flows steadily over a variety of hydrophobic microgrooved surfaces [27]. Their measurements showed smaller slip length compared to the analytical calculations by Philip [28] that assumes a flat gas-liquid interface and infinitely long channels. The mass transport through porous walls was numerically studied to investigate the effects of slip velocity at the porous wall by Chellam et al. [29]. They derived expressions for the axial and transverse velocities and axial pressure drop by incorporating fluid slip at the porous channel wall. They found increasing the magnitude of slip coefficient decreases the shear rate at the porous wall, which leads to reduction in concentration polarization. They showed open structures on the membrane surface leads to high membrane permeabilities. Varol et al. [30] studied the two-dimensional flow through a channel confined by a porous bottom wall and with fins at the top wall. They found that the concentration on the porous wall and the concentration boundary layer thickness decrease with increasing fin length, slip coefficient and inlet flow rate [30]. Chellam et al. studied analytically the effect of slip flow in uniformly porous tubes with permeating walls in a wide range of wall Reynolds numbers [31]. They found close correlations for the influence of slip on velocity profiles, pressure gradients and wall shear for wide range of Reynolds number. They showed in the membrane filtration process, the nature of the axial pressure gradient can be influenced if slip effects appears at the channel wall.

Hassell and Zimmerman studied numerically the flow through SHM to characterize their effect of grooves for a *Re* range of 0-15 [32]. They found improved micromixer performance with increasing grooves per half cycle. The generation of rotating flows in the grooved micromixer and the mixing performance by optimizing the groove design was extensively studied numerically [33, 34]. Many attempts have been made in the

past to achieve lower drag using dense micropatterned structures. The constituents transport from diffusive boundaries into the fluid is completely different compared to transport through dense membranes. However, effective gas-liquid contacting and optimization studies using porous hydrophobic membranes have not been studied so far. A general fabrication approach facilitating the production of porous microfluidic devices with customized structures has already been developed [35–37].

This work aims to numerically study the mixing performance of microgrooved membrane microcontactors for gas-liquid systems. The mass transport equations across the membrane are solved together with the momentum balance equations in 2-D and 3-D. This approach is applied to two types of membrane modules (see Figure 3.1); one with continuous straight grooves and one with non-continuous grooves. It systematically includes CFD studies with an optimization strategy based on the design of experiments (DOE) approach.

3.2 Problem setup and numerical analysis

A schematic of a microchannel containing a porous superhydrophobic membrane surface with continuous and non-continuous microgrooves is shown in Figure 3.1 A and B correspondingly. The liquid (ρ_L, μ_L) flows under laminar conditions through the liquid microchannel (height H_1) while the gas (ρ_G, μ_G) diffuses through a porous membrane. The pores and grooves of the membrane are filled with gas, as shown schematically in Figure 3.1C. The gas is entrapped in the grooves creating a gas-liquid interface (Cassie state). Here, we are assuming a flat interface as in most previous studies [25, 38, 39]. Figure 3.1D shows the computational domain considered for the two-dimensional case. The length and depth of the groove are denoted as L_1 and H_2 and the distance between two consecutive grooves is denoted as L_2. The computational domain will be bounded by the xy-plane. The main pressure driven flow will be in x-direction. For simplicity, the width of the channel in z-direction is not considered here. The gas is treated as an incompressible fluid with viscosity μ_G. The flow in the microchannel is assumed to be laminar, isothermal, steady-state and incompressible. Gas uptake of pure CO_2 by water was chosen as a model system.

The reduction in drag due to shear-free boundaries is widely studied as a slip velocity

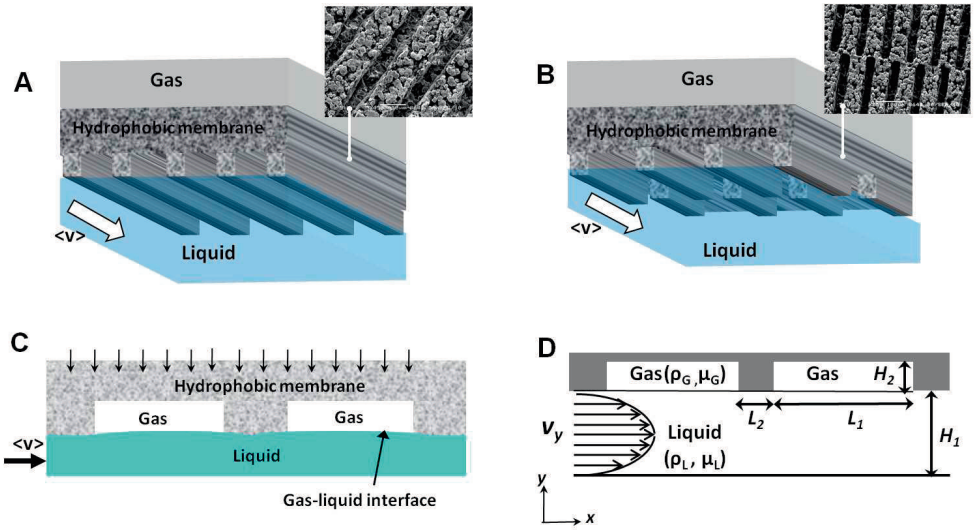

Figure 3.1: Schematic illustration of gas-liquid contacting using hydrophobic microgrooved membranes. A hydrophobic surface pattern provides a hybrid interface (A) continuous microgrooved module (B) non-continuous microgrooves (C) gas pockets trapped in a hydrophobic membrane with non-continuous microgrooves (D) computational model domain mentioning geometrical parameters for non-continuous microgrooves.

at the wall [4, 23, 27–29]. The slip velocity at the interface, v_{slip}, is defined as:

$$v_{slip} = b \left| \frac{\partial v_x}{\partial y} \right| \tag{3.1}$$

where b is the slip length. The governing equations describing the flow field and mass transfer for microgrooved membranes can be derived as follows: Continuity equation:

$$\nabla \cdot \boldsymbol{v} = 0 \tag{3.2}$$

Momentum balance equation:

$$\rho(\boldsymbol{v} \cdot \nabla)\boldsymbol{v} = -\nabla p + \mu \nabla^2 \boldsymbol{v} \tag{3.3}$$

Here, ρ is the density, μ is the viscosity, $\boldsymbol{v}$ is the velocity vector and p is the pressure.

The mass balance involving a reaction in the bulk liquid is described as:

$$D\nabla^2 C_l = \boldsymbol{v} \cdot \nabla C_l - R \tag{3.4}$$

where D is the diffusion coefficient, C_l is the solute concentration in liquid and R is the reaction term.

A fully developed laminar flow profile (parabolic) is implemented at the microchannel inlet while the outlet is kept at normal pressure. There will be zero gas (CO_2) concentration at the microchannel inlet. Convective flux will be implemented at the outlet boundary.

Along the lower boundary ($y = 0$),

- solid-liquid region: no slip,

$$v_x = v_y = 0 \tag{3.5}$$

Along the upper boundary ($y = H_1$),

- gas-liquid interface: shear-free, velocity for gas and liquid at the interface are equal:

$$v_x = v^i_{x,g} = v^i_{x,l} \tag{3.6}$$

- solid-liquid interface (in case of non-continuous grooves): no-slip,

$$v_x = v_y = 0 \tag{3.7}$$

where, $v^i_{x,g}$ and $v^i_{x,l}$ represents gas and liquid interface velocity in x-direction, respectively.

The saturated wall boundary condition will be implemented over the entire gas-liquid contacting wall. Due to little resistance of gas transport through the porous membrane (and pure CO_2 gas used), the rate limiting step in mass transfer is assumed to be in the liquid phase. Therefore, flow field and mixing are modeled only for the liquid phase. The following three cases were studied for the continuous micropattern systems;

- Laminar flow with gas diffusing into the liquid (Physical absorption)

- Laminar flow with gas diffusing into the liquid and subsequent reaction in the bulk
- Laminar flow with gas diffusing into the liquid and reaction at the gas-liquid interface

Equation (3.4) is applicable for the first two cases mentioned above. For the third case, gas-liquid contacting and surface reaction at the gas-liquid interface, the reaction term is incorporated in the boundary condition.

CO_2 absorption in water was numerically simulated in steady state conditions. The absorption of gas into the liquid is set by the CO_2 solubility represented by Henry's law:

$$C_l = HC_g \tag{3.8}$$

where, C_g is the carbon dioxide concentration in gas. H is the Henry's coefficient. The diffusive flux, N_l, of gas through the interface is described as:

$$N_l = D\nabla C_l \tag{3.9}$$

The outlet flux, $N_{l,o}$, of the absorbed gas concentration at the outlet cross-section normal to the flow direction is defined as:

$$N_{l,o} = \frac{\int_A N_l \cdot \boldsymbol{v} dA}{\int_A \boldsymbol{v} dA} \tag{3.10}$$

Two-dimensional simulations were performed to investigate the hydrodynamic flow field and mass transport using finite element modeling (comsol). The model solves the momentum balance equation (Incompressible Navier-Stokes) coupled with the mass balance equation (species convection-diffusion). To obtain mesh size independent results from numerical simulations, several preliminary tests were performed. The size of the grid cells for all the 2D models in this study resulted in the range of 0.6-5.8 μm approximately for a mesh density in the range of 37-150 thousand triangular cells (Lagrange type p2,p1) for the total computational domain. The physical properties taken in the numerical simulations are shown in Table 3.1.

Table 3.1: Properties of the fluids at 20℃

Fluid	Density (kg/m^3)	Viscosity $(kg/m \cdot s)$	Diffusivity in water (m^2/s)
Water	9.98×10^2	0.9×10^{-3}	-
Carbon dioxide	0.773	0.091×10^{-6}	1.00×10^{-9}

3.3 Geometrical optimization

In order to obtain enhanced performance of microgrooved membrane modules, it is essential to identify critical design parameters and their range of variations. The initial step is to choose what performance parameters are going to be optimized with their range of variation. Then, the design of experiments (DOE) method will be implemented to define the corresponding number of geometries for the microgrooved membrane modules. Numerical simulations are then performed with these geometries to analyze the performance. Flux enhancement is chosen as the performance parameter. This quantification is possible by calculating the outlet fluxes of the microgrooved and flat membrane modules. The flux enhancement, E, is calculated at the outlet for each modules as;

$$E = \frac{(N^s_{l,o} - N^f_{l,o})}{N^f_{l,o}} \tag{3.11}$$

Here, $N^s_{l,o}$ and $N^f_{l,o}$ are outlet fluxes for the structured (s) and flat (f) membranes, respectively. One of the important factors affecting the precision of the design methodology is the choice of geometrical design variables and their range. Principally, some preliminary tests are necessary for sensitivity analysis which gives a tentative range of design variables before proceeding towards a detailed design. Table 3.2 shows the ranges and values of the geometrical design parameters taken in our study. An

Table 3.2: Range of microgroove design parameters and levels used in OA L_{27}

Levels	Factors				
	L_1 [m]	L_2 [m]	H_1 [μm]	H_2 [μm]	$\langle v \rangle$ [m/s]
1	0.01	0.015	200	10	0.01
2	0.005	0.001	300	20	0.03
3	0.001	0.005	400	40	0.05

experimental table of 27 designs (Table 3.3) was formulated by using the Orthogonal Array (OA) L_{27} of the Taguchi method [40]. For all models used in the optimization study, the total length of the microchannel is fixed at 0.1 m.

Table 3.3: Orthogonal Array (OA) L_{27} indicating the levels of each design variable.

Experiments of	Design parameters				
CFD studies	L_1	L_2	H_1	H_2	$\langle v \rangle$
1	1	1	1	1	1
2	1	1	2	2	1
3	1	1	3	3	1
4	1	2	1	2	2
5	1	2	2	3	2
6	1	2	3	1	2
7	1	3	1	3	3
8	1	3	2	1	3
9	1	3	3	2	3
10	2	1	1	2	1
11	2	1	2	3	1
12	2	1	3	1	1
13	2	2	1	3	2
14	2	2	2	1	2
15	2	2	3	2	2
16	2	3	1	1	3
17	2	3	2	2	3
18	2	3	3	3	3
19	3	1	1	3	1
20	3	1	2	1	1
21	3	1	3	2	1
22	3	2	1	1	2
23	3	2	2	2	2
24	3	2	3	3	2
25	3	3	1	2	3
26	3	3	2	3	3
27	3	3	3	1	3

The DOE based on Taguchi method [40] method defines a set of design configurations from the design space which is representative to evaluate the influence of design parameters on the performance. It is based on an orthogonal array (OA) of experiments that gives reduced variance for the experiment with optimum settings of design parameters. With this method, the number of experiments (or simulations) can be reduced significantly. The sensitivity of the design parameters on the flux enhancement can also be analyzed.

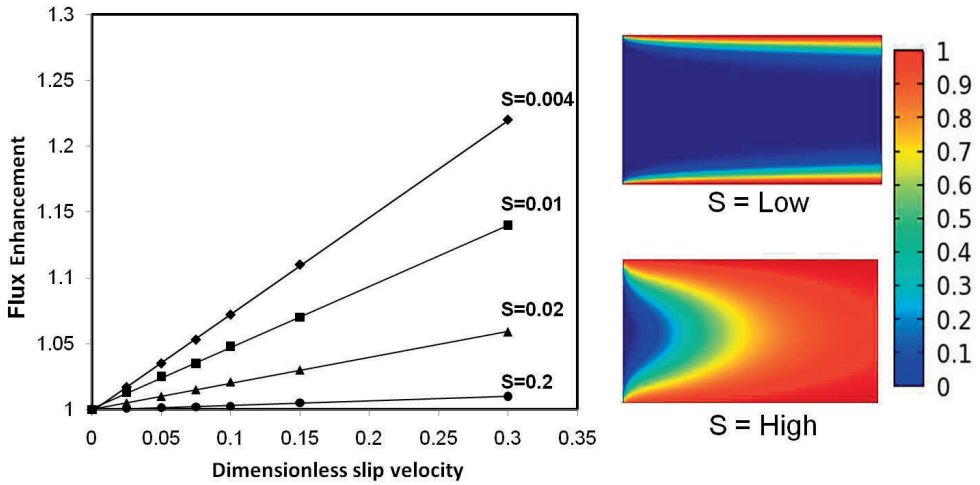

Figure 3.2: Variation of the flux enhancement with the dimensionless slip velocity for varying saturation. The lower S represents an unsaturated system and a higher S a saturated system. The right images show numerical results representing corresponding cases (slip condition on both upper and lower wall).

3.4 Results and discussion

The results of the numerical simulations aid in the interpretation of gas-liquid contacting performance in grooved membrane modules. Using the numerical methodology described in the previous section, simulations were performed in order to quantify the effect of microgroove geometry and resulting slip velocity on the performance of the membrane. Later, the optimization methodology is applied and results are presented for individual cases.

3.4.1 Continuous microgrooves

The numerical simulation methodology starts with computing the flow behavior and mass transfer for continuous microgrooved membranes. The flux enhancement is used to quantify the effect of the microgrooves.

Variations in liquid and gas velocities near the gas-liquid interface were observed along the microgrooved surfaces where it is influenced by the shear-free boundary condition. In order to evaluate the model systematically, a dimensionless Saturation number S has been used. It is represented by the ratio of diffusion time to convection time.

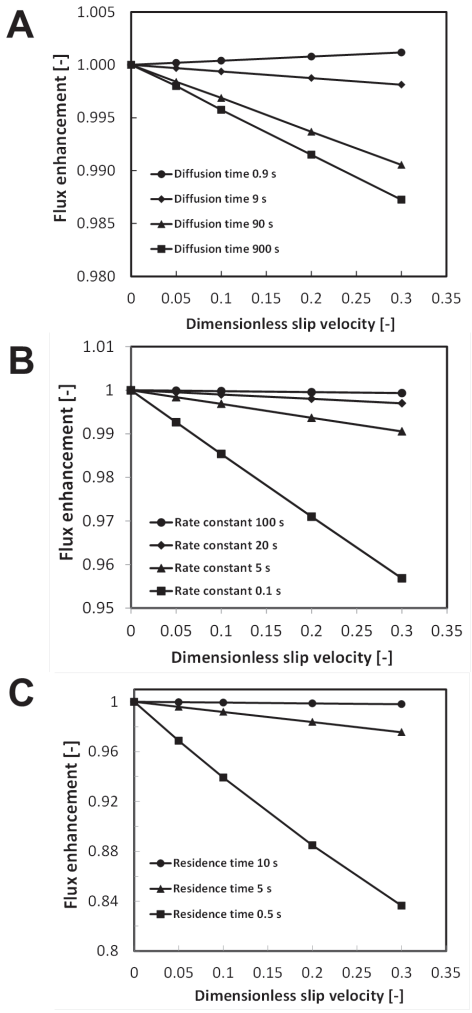

Figure 3.3: Flux enhancement vs. dimensionless slip velocity for a bulk reaction system (A) influence of diffusion time (B) influence of bulk reaction rate constant (C) influence of residence time.

In order to compare different module configurations varying height and length of the microchannel in a dimensionless manner, this number is used instead of Péclet number. The liquid outlet will be unsaturated with the gaseous reactants when S is low, whereas for high S, the outlet stream is almost saturated (see Fig. 3.2).

$$S = \frac{D \cdot L}{v_x \cdot H_1^2} \tag{3.12}$$

where D is the diffusion coefficient (m^2/s), L is the length of the microchannel (m), v_x is the axial velocity (m/s) and H_1 is the liquid channel height (m). It can be observed that the flux enhancement is dependent on the saturation level of the gas-liquid system. An enhancement in flux is observed with a decrease in saturation level and an increase in the dimensionless slip velocity. The increase in flux is due to the enhanced convective transport near the wall in the case of slip velocity. Therefore, slip in unsaturated systems (low S) gives higher flux enhancement compared to saturated system (high S).

The effect of slip velocity near the membrane wall has been investigated for a gas-liquid first-order irreversible reaction in the liquid bulk (by incorporating a homogeneous reaction term in Eq.(3.4)). The flux enhancement study was performed varying the dimensionless slip velocity, residence time, diffusion coefficient and reaction rate constant, as shown in Fig. 3.3. In most cases slip flow resulted in a decreased performance only when the liquid is saturated with the reactant (low diffusion time: $t_D = H^2/D \approx 0.9$s). This is due to the dependence between mass transfer into the liquid and reaction in the bulk. The bulk reaction rate increases for lower diffusion time due to higher gas uptake from the membrane surface resulting from the slip. For low saturation levels, the slip effectively reduces the residence time of components near the interface, thereby lowering the conversion. The flux enhancement observed for different reaction rate constants is presented in Figure 3.3B. Very little flux enhancement is obtained for large reaction rate constants. This is due to the fact that at higher reaction rate constant, the mass transfer of gas into the liquid becomes limiting. For longer residence times as shown in Figure 3.3C, it can be observed that the flux enhancement is lower because of higher saturation. The flux enhancement is mainly negative at shorter residence time, which can be explained due to the relatively shorter time available for the liquid to sweep the absorbing gas off from the channel wall.

The next system investigated was the continuous microgrooved membrane system involving a gas-liquid reaction at the channel wall. This system correlates with a typical chemical absorption at the gas-liquid interface. The concentration on the boundary is saturated with the gaseous component. The liquid reactant has to diffuse to the gas-liquid interface and react with the gas to form the product. A first-order irreversible reaction is considered for the surface reaction. The flux enhancement is again studied for diffusion time, reaction rate constant and residence time and is shown in Figure 3.4. It can be observed from the figure that slip at the gas-liquid interface has a strong positive effect on the flux enhancement for all conditions. Higher flux

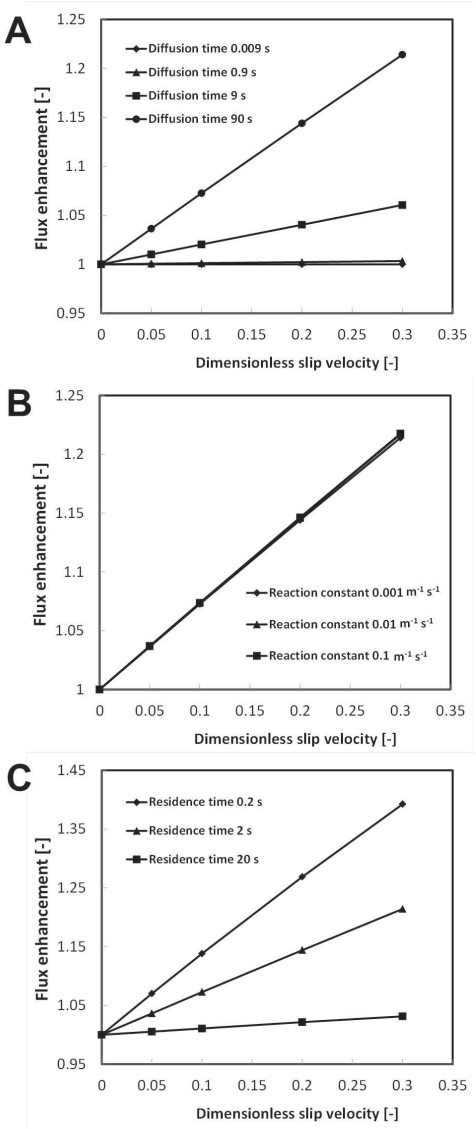

Figure 3.4: Flux enhancement vs. dimensionless slip velocity for a surface reaction system (A) influence of diffusion time (B) influence of surface reaction constant (C) influence of residence time

enhancement for larger (gaseous component) diffusion time is observed, which is due to instantaneous gas uptake near the microchannel wall. As diffusion time becomes smaller, higher saturation is established in the microchannel, reducing the effect of slip. Similarly, for large residence times (low flow rates), the gas concentration reaches the

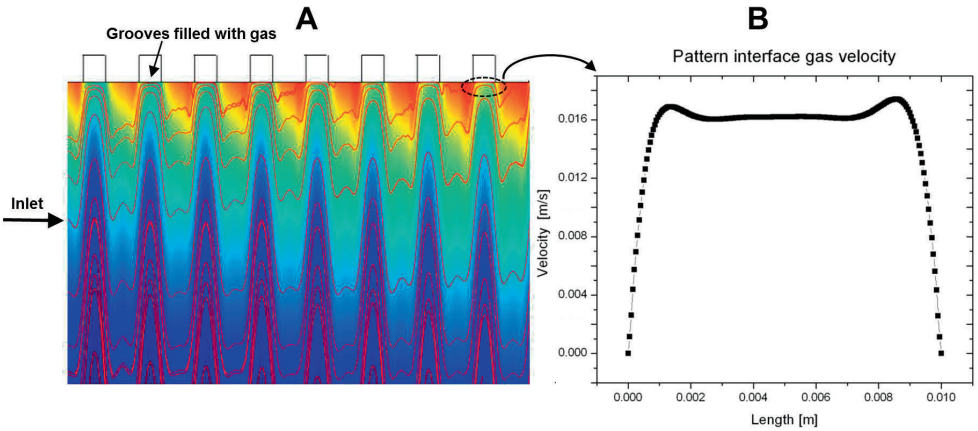

Figure 3.5: Flow profile with alternated microgrooves (slip boundary) is viewed along the scaled microchannel. (A) Close view near the microgrooves showing concentration profile in the microchannel and streamlines showing the perpendicular displacement along the microchannel. (B) Gas-liquid interface velocity, along the length of the microgroove.

saturation level. This decreases further gas uptake into the liquid and limits the flux enhancement. Higher flux enhancement is observed for lower residence time, which is due to a steep concentration profile generated near the microchannel wall which is refreshed better in case of slip flow. The effects of reaction rate constant on the flux enhancement was negligible in the studied range because the systems is diffusion limited. It is clear that surface reaction systems can benefit significantly from surface slip flow.

3.4.2 Non-continuous microgrooves

The flow and concentration profile over non-continuous microgrooves is presented in Figure 3.5. The interface consists of alternating slip and no-slip regions. Figure 3.5A shows the concentration profile and some streamlines magnified near the gas-liquid interface. Due to the acceleration at the gas-liquid interface (slip), displacement in the y-direction appears. Figure 3.5B shows the velocity profile at the gas-liquid interface in x-direction. The velocity increases at the beginning of the grooves and reaches a maximum. Towards the end of each groove, the x-velocity decreases to no-slip velocity.

The effect of different heights and lengths of the microgrooves on the gas-liquid

interface velocity has been studied numerically. It can be observed that the height of the microgroove has a significant influence on the gas-liquid interface velocity. For a height of 10 μm, the interface velocity is approximately 70 % of the maximum gas-liquid slip velocity, while a pattern depth of 40 μm results in 95 % of the full slip boundary condition. This can be explained due to flow field generated in the gas phase, which indicates rotating vortices. The counter rotating vortex offer additional resistance to the interface velocity resulting decreased gas-liquid interface velocity. Flow fields in such grooves share characteristics of confined flow of gas phase [41, 42].

The length of the micropattern has a significant influence on the surface velocity as can be seen in Fig. 3.6. The shorter microgroove length of 1 and 2 millimeters show a velocity development without reaching the maximum velocity. For longer micropatterns, the gas-liquid interface velocity reaches a plateau of maximum velocity and achieves the value of full slip boundary condition.

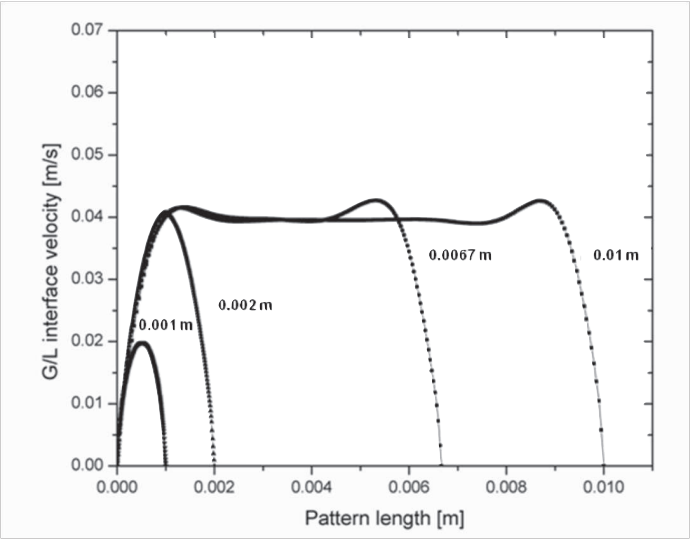

Figure 3.6: Gas-liquid velocity profile for different groove lengths (channel height with 300 μm, pattern height 30 μm, average inlet velocity 0.03 m/s)

Figure 3.7 shows concentration profiles for continuous and non-continuous microgrooved membranes. Non-continuous microgrooves generate convective flow perpendicular to the direction of the flow. This gives enhanced gas uptake compared to the continuous grooved surface. The next section describes the detailed optimization study elaborating the influence of microgroove geometry on the flux enhancement.

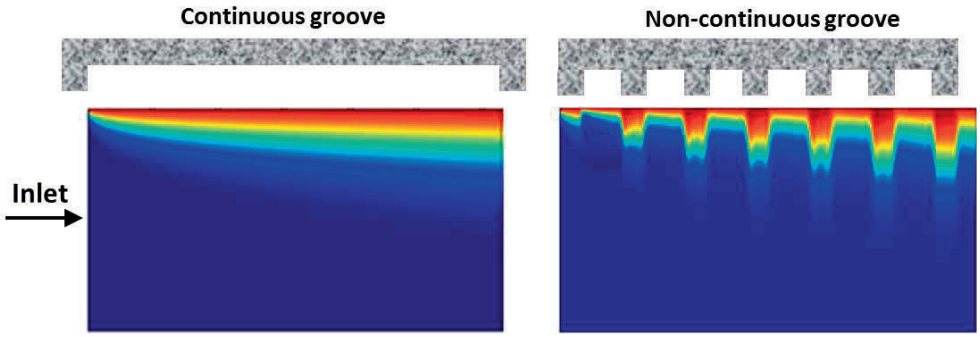

Figure 3.7: Concentration profiles along the length of the channel; left, continuous microgroove and on right, non-continuous microgrooves. Alternated microgrooves give enhanced mixing near the gas-liquid interface due to perturbations in the velocity profile.

3.4.3 Optimization of microgroove geometry

The effects of wall pattern geometry was investigated numerically. The application of an optimization study using an orthogonal array gave the influence of the design parameters on the flux enhancement. To evaluate the contribution of each level of a design parameter on the flux enhancement, the mean of the variances of the experiments in the OA L_{27} (as mentioned in Table 3.2) is calculated. In this study, the groove length L_1, distance between two consecutive grooves L_2, groove height H_2, channel height H_1, and the average inlet velocity $\langle v \rangle$ have been varied. Every parameter was varied in a specific range representing the design space for optimization. The results shown in Figure 3.8 indicate that the enhancement in flux is increasing with the increasing channel height (H_1), pattern length (L_1) and average velocity ($\langle v \rangle$).

There will be less enhancement in the case of larger spacing between two consecutive grooves (L_2). For the 20 μm height of the pattern (H_2), there will be minimum enhancement. An explanation for this drop in enhancement is the reduced gas-liquid interface velocity near the micropatterns. The flow profile in the gas phase indicates two-counter rotating vortices which results in a decrease of the interface velocity. This alteration of flow profile influences the mass and momentum transfer into the liquid and, consequently affects the performance. Flow characteristics in such cavities qualitatively share common features with lid-driven cavity (LDC) flow [41, 42], where primary eddy circulation form at the core of the cavity with secondary vortices in the

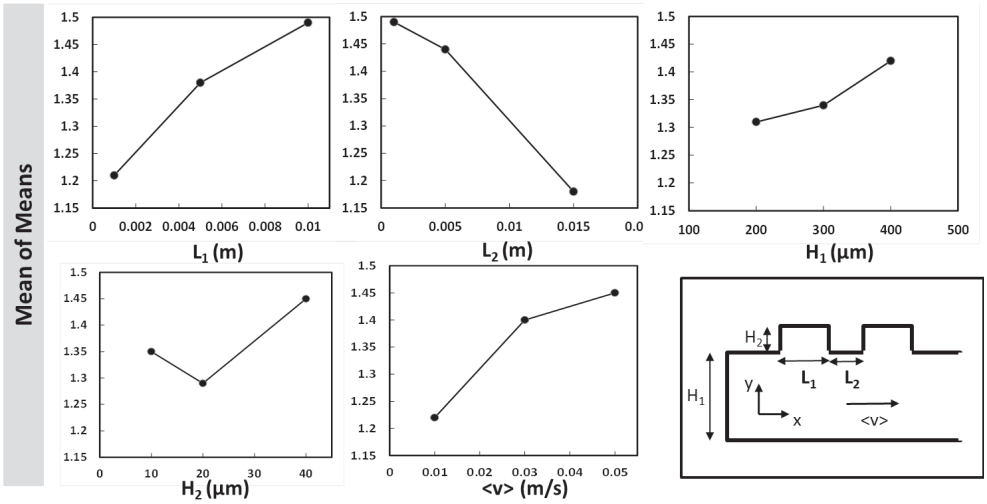

Figure 3.8: Optimization study, involving geometrical parameters of non-continuous grooved membranes module, for flux enhancement as performance indicator. The lower right picture shows geometrical features considered for the numerical optimization study.

corners.

One of the interesting observation is a higher flux enhancement with the increase in microgroove length (L_1). A higher ratio of L_1/L_2 gives more slip surface which enhances the flux. The flux enhancement is stronger for larger velocities. This can be explained in two ways: the y-velocity in increases due to the higher interface velocities which increases mixing and a higher velocity gives lower saturation according to Eq. (3.12). The flux is enhanced more with larger channel height because the velocity profile near the wall is less steep compared to the narrow channel.

3.5 Conclusions

A complete numerical analysis and geometric optimization study (DOE) has been employed for microgrooved membranes. Microgrooved membranes offer a stable gas-liquid interface with high surface-to-volume ratio. The hydrodynamic flow of the liquids is influenced by microgrooves on porous membranes. Two different types of microgrooves have been studied in relation to mass transport: continuous and non-continuous microgrooves. The use of continuous and alternating microgrooves

gives enhancement in absorption of gas into the liquid. A detailed geometrical optimization study using Taguchi method was conducted to elucidate the enhancement in flux for microgrooved membranes over flat membranes. The study showed that the degree of mixing has been significantly increased with micropatterning the surface using continuous or non-continuous grooves. This research indicates that structured hydrophobic porous membranes can be successfully employed to increase mass transfer and reduce concentration polarization along the gas-liquid interface.

3.6 Acknowledgements

This work was financially supported by Stichting voor de Technische Wetenschappen (STW, Project 07569). The authors also greatly acknowledge H.C.Aran for fruitful discussions.

3.7 References

[1] V. Hessel, P. Angeli, A. Gavriilidis and H. Löwe; *Gas- Liquid and Gas-Liquid- Solid Microstructured Reactors: Contacting Principles and Applications*; Ind. Eng. Chem. Res **44** (25) (2005) 9750–9769

[2] K. Jensen; *Microchemical systems: status, challenges, and opportunities*; AIChE Journal **45** (10) (1999) 2051–2054

[3] S. Haswell and V. Skelton; *Chemical and biochemical microreactors*; TrAC Trends in Analytical Chemistry **19** (6) (2000) 389–395

[4] H. Stone, A. Stroock and A. Ajdari; *Engineering flows in small devices*; Annual Review of Fluid Mechanics **36** (1) (2004) 381

[5] S. Mitrovski and R. Nuzzo; *An electrochemically driven poly (dimethylsiloxane) microfluidic actuator: oxygen sensing and programmable flows and pH gradients*; Lab Chip **5** (6) (2005) 634–645

[6] S. Herber, J. Bomer, W. Olthuis, P. Bergveld and A. Berg; *A miniaturized carbon dioxide gas sensor based on sensing of pH-sensitive hydrogel swelling with a pressure sensor*; Biomedical Microdevices **7** (3) (2005) 197–204

[7] S. Ohira and K. Toda; *Micro gas analysis system for measurement of atmospheric hydrogen sulfide and sulfur dioxide*; Lab Chip **5** (12) (2005) 1374–1379

[8] J. De Jong, R. Lammertink and M. Wessling; *Membranes and microfluidics: a review*; Lab Chip **6** (9) (2006) 1125–1139

[9] H. Aref; *The development of chaotic advection*; Physics of Fluids **14** (2002) 1315

[10] A. Stroock, S. Dertinger, A. Ajdari, I. Mezic, H. Stone and G. Whitesides; *Chaotic mixer for microchannels*; Science **295** (5555) (2002) 647

[11] R. Liu, M. Stremler, K. Sharp, M. Olsen, J. Santiago, R. Adrian, H. Aref and D. Beebe; *Passive mixing in a three-dimensional serpentine microchannel*; Journal of Microelectromechanical Systems **9** (2) (2002) 190–197

[12] A. Kamholz, B. Weigl, B. Finlayson and P. Yager; *Quantitative analysis of molecular interaction in a microfluidic channel: the T-sensor*; Anal. Chem. **71** (23) (1999) 5340–5347

[13] T. Fujii, Y. Sando, K. Higashino and Y. Fujii; *A plug and play microfluidic device*; Lab Chip **3** (3) (2003) 193–197

[14] H. Mao, T. Yang and P. Cremer; *A microfluidic device with a linear temperature gradient for parallel and combinatorial measurements*; J. Am. Chem. Soc **124** (16) (2002) 4432–4435

[15] M. Oddy, J. Santiago and J. Mikkelsen; *Electrokinetic instability micromixing*; Anal. Chem **73** (24) (2001) 5822–5832

[16] Z. Yang, S. Matsumoto, H. Goto, M. Matsumoto and R. Maeda; *Ultrasonic micromixer for microfluidic systems*; Sensors and Actuators A: Physical **93** (3) (2001) 266–272

[17] F. Bessoth, A. deMello and A. Manz; *Microstructure for efficient continuous flow mixing*; Analytical Communications **36** (6) (1999) 213–215

[18] D. Gobby, P. Angeli and A. Gavriilidis; *Mixing characteristics of T-type microfluidic mixers*; Journal of Micromechanics and Microengineering **11** (2001) 126

[19] F. Jiang, K. Drese, S. Hardt, M. Küpper and F. Schönfeld; *Helical flows and chaotic mixing in curved micro channels*; AIChE Journal **50** (9) (2004) 2297–2305

[20] F. Schönfeld and S. Hardt; *Simulation of helical flows in microchannels*; AIChE Journal **50** (4) (2004) 771–778

[21] T. Johnson, D. Ross and L. Locascio; *Rapid microfluidic mixing*; Anal. Chem. **74** (1) (2002) 45–51

[22] P. Howell, D. Mott, S. Fertig, C. Kaplan, J. Golden, E. Oran and F. Ligler; *A microfluidic mixer with grooves placed on the top and bottom of*

the channel; Lab Chip **5** (5) (2005) 524–530

[23] J. Ou, G. Moss and J. Rothstein; *Enhanced mixing in laminar flows using ultrahydrophobic surfaces*; Physical Review E **76** (1) (2007) 16304

[24] J. Ou and J. Rothstein; *Direct velocity measurements of the flow past drag-reducing ultrahydrophobic surfaces*; Physics of Fluids **17** (2005) 103606

[25] D. Maynes, K. Jeffs, B. Woolford and B. Webb; *Laminar flow in a microchannel with hydrophobic surface patterned microribs oriented parallel to the flow direction*; Physics of Fluids **19** (2007) 093603

[26] K. Watanabe, Y. Udagawa and H. Udagawa; *Drag reduction of Newtonian fluid in a circular pipe with a highly water-repellent wall*; Journal of Fluid Mechanics **381** (1999) 225–238

[27] P. Tsai, A. Peters, C. Pirat, M. Wessling, R. Lammertink and D. Lohse; *Quantifying effective slip length over micropatterned hydrophobic surfaces*; Physics of Fluids **21** (2009) 112002

[28] J. Philip; *Flows satisfying mixed no-slip and no-shear conditions*; Zeitschrift für Angewandte Mathematik und Physik (ZAMP) **23** (3) (1972) 353–372

[29] S. Chellam, M. Wiesner and C. Dawson; *Slip at a uniformly porous boundary: effect on fluid flow and mass transfer*; Journal of Engineering Mathematics **26** (4) (1992) 481–492

[30] S. Varol, N. Yucel and H. Turkoglu; *Laminar flow and mass transfer in channels with a porous bottom wall and with fins attached to the top wall*; Heat and Mass Transfer **36** (2) (2000) 103–108

[31] S. Chellam and M. Liu; *Effect of slip on existence, uniqueness, and behavior of similarity solutions for steady incompressible laminar flow in porous tubes and channels*; Physics of Fluids **18** (2006) 083601

[32] D. Hassell and W. Zimmerman; *Investigation of the convective motion through a staggered herringbone micromixer at low Reynolds number flow*; Chemical Engineering Science **61** (9) (2006) 2977–2985

[33] N. Lynn and D. Dandy; *Geometrical optimization of helical flow in grooved micromixers*; Lab Chip **7** (5) (2007) 580

[34] C. Cortes-Quiroz, M. Zangeneh and A. Goto; *On multi-objective optimization of geometry of staggered herringbone micromixer*; Microfluidics and Nanofluidics **7** (1) (2009) 29–43

[35] J. De Jong, B. Ankone, R. Lammertink and M. Wessling; *New replication technique for the fabrication of thin polymeric microfluidic devices with tunable porosity*; Lab Chip **5** (11) (2005) 1240–1247

[36] L. Vogelaar, R. Lammertink, J. Barsema, W. Nijdam, L. Bolhuis-Versteeg, C. Van Rijn and M. Wessling; *Phase separation micromolding: a new generic approach for microstructuring various materials*; Small **1** (6) (2005) 645–655

[37] L. Vogelaar, R. Lammertink and M. Wessling; *Superhydrophobic surfaces having two-fold adjustable roughness prepared in a single step*; Langmuir **22** (7) (2006) 3125–3130

[38] E. Lauga and H. Stone; *Effective slip in pressure-driven Stokes flow*; Journal of Fluid Mechanics **489** (1) (2003) 55–77

[39] C. Cottin-Bizonne, C. Barentin, É. Charlaix, L. Bocquet and J. Barrat; *Dynamics of simple liquids at heterogeneous surfaces: Molecular-dynamics simulations and hydrodynamic description*; The European Physical Journal E: Soft Matter and Biological Physics **15** (4) (2004) 427–438

[40] A. Atkinson, A. Donev and R. Tobias, editors; *Optimum Experimental Designs*; ISBN978-0-19-929659-0 (2007); New York: Oxford University Press

[41] J. Koseff and R. Street; *On end wall effects in a lid-driven cavity flow*; Journal of Fluids Engineering **106** (1984) 385

[42] C. Aidun, N. Triantafillopoulos and J. Benson; *Global stability of a lid-driven cavity with throughflow: Flow visualization studies*; Physics of Fluids A: Fluid Dynamics **3** (1991) 2081

CHAPTER 4

A microgrooved membrane (based) gas-liquid contactor

A revised version of this chapter has been prepared for publication:

Jigar M. Jani, M. Wessling, Rob G.H. Lammertink *Gas-liquid contacting using microgrooved membrane devices*

Abstract

This chapter presents an approach for applying microgrooved membranes for improved gas-liquid contacting. The study involve analysis of the performance of the microdevice by quantifying the flux enhancement for different membrane configurations. Two kinds of configurations, continuous and non-continuous grooves, were investigated. The microgrooves provide shear-free gas-liquid interfaces, which result in local slip velocity at the gas-liquid interface. Exploiting this physical phenomenon, it is possible to reduce mass transport limitations in gas-liquid contacting. An experimental study using grooved membranes suggest enhancement in flux up to 20-30 %. The flux enhancement at higher liquid flow rates is observed due to a partial shear-free gas-liquid interface. The performance of the membrane devices decreased with wetted microgrooves due to the mass transport limitations. The flow visualization experiments reveal wetting of the microgrooves at higher liquid flow rates. According to the numerical and experimental study, we have shown that microgrooved membranes can be employed to improve gas-liquid contacting processes.

4.1 Introduction

Microfluidic systems offer a number of advantages such as enhanced heat and mass transfer intensifying many chemical and biological processes [1–3]. Numerous studies have been performed regarding multiphase flows (at micro- and nanoscale) for important applications in the field of microfluidic devices [4–9]. The mass transfer limitations present in single-phase flow can be reduced by introducing an additional immiscible fluid. Such multiphase systems induce recirculation motion in the liquid stream that enhanced mixing. An important field of application for these systems considers gas-liquid contacting/reactions [10]. For gas-liquid reactions, often multiphase systems are employed to achieve fast mixing, lower mass transfer limitations and better control over reaction conditions [11].

The flow behavior at the microscale is considerably different than that in macroscopic flows. The fluid flow at the microscale can be characterized by high surface-to-volume ratios. Due to their characteristic small dimensions, the flow is mainly laminar ($Re << 1$), and mixing proceeds via diffusion dominantly. There have been many attempts to enhance mixing in the microchannel using active and passive micromixers [12–15].

Active mixing can be achieved by creating instabilities in the flow field [16], by means of, pressure fluctuations [17], thermal power [18], electrokinetic forces [19] and ultrasonic actuation [20]. Active micromixers have several disadvantages like using external power sources and complexity in terms of device fabrication, operation and maintenance. Passive micromixers, on the other hand, utilize no additional power other than the principle pressure drop used for the fluid flow. They accomplish mixing due to formation of flow features induced by geometrical features of the microchannel. One approach to achieve passive mixing is using splitting and recombining which combines two streams flowing from opposite direction [21]. Another way of achieving mixing makes use of specifically oriented grooves to generate vortices [12, 22]. The twisted microchannels generate curvature induced secondary flows for mixing [13, 23–26]. All these configurations aims for simple yet efficient mixing in the shortest microchannel distance possible.

The flow dynamics over microgrooved superhydrophobic surfaces has been studied extensively [27–30]. The frictional resistance offered by such interfaces can be dramatically reduced. The textured surfaces consists of microscale alternating channels

grooves or posts. The hydrophobicity prevents liquid from wetting the grooves and entraps air in the cavity. The gas phase exhibits a much lower viscosity compared to the liquid moving past the microgrooves, resulting in interfacial slip velocities. There has been lot of work performed, experimentally and numerically, on characterizing this drop in drag using microchannels with superhydrophobic surfaces [31, 32]. Maynes et al. [33] showed experimental and numerical results for laminar flow through a microchannel with superhydrophobic surfaces incorporating grooves aligned parallel to the flow direction. Their numerical predictions showed that the effective slip length increases with increasing relative cavity width and depth, and decreasing relative microrib/cavity module length. Hassell and Zimmerman [34] studied numerically the flow through Staggered Harringbone Micromixer (SHM) to characterize the effect of the grooves on the fluid flow in the channel for *Re* range 0-15. They found improved micromixer performance with increasing grooves per half cycle.

There are many examples where membranes can be used for gas-liquid contacting utilizing porous hydrophobic membranes [35]. Since the gas phase is in contact with the liquid phase along the device, exchange of mass between the two phases is possible. Microgrooves over such membranes gives rise to slip velocities along the gas-liquid interface [36].

As mentioned above, many attempts have been made to achieve lower drag over gas-liquid interfaces using different microgrooved designs. Transport of gas into the liquid using porous membrane microfluidic devices is often limited by small diffusivities of the species involved. The use of microgrooves on hydrophobic surface can be an interesting approach to achieve enhanced transport through porous walls. Here we describe the concept of microgrooved membranes for gas-liquid contacting that allows the investigation of fluid flow and mass transfer in various membrane configurations.

4.2 Experimental

4.2.1 Membrane fabrication

The microgrooved membranes studied in this work were fabricated using conventional phase-separation micromolding [37] (Fig. 4.1). Three types of porous PVDF (polyvinylidene fluoride, Hylar 460, Ausimont) membranes are fabricated for the

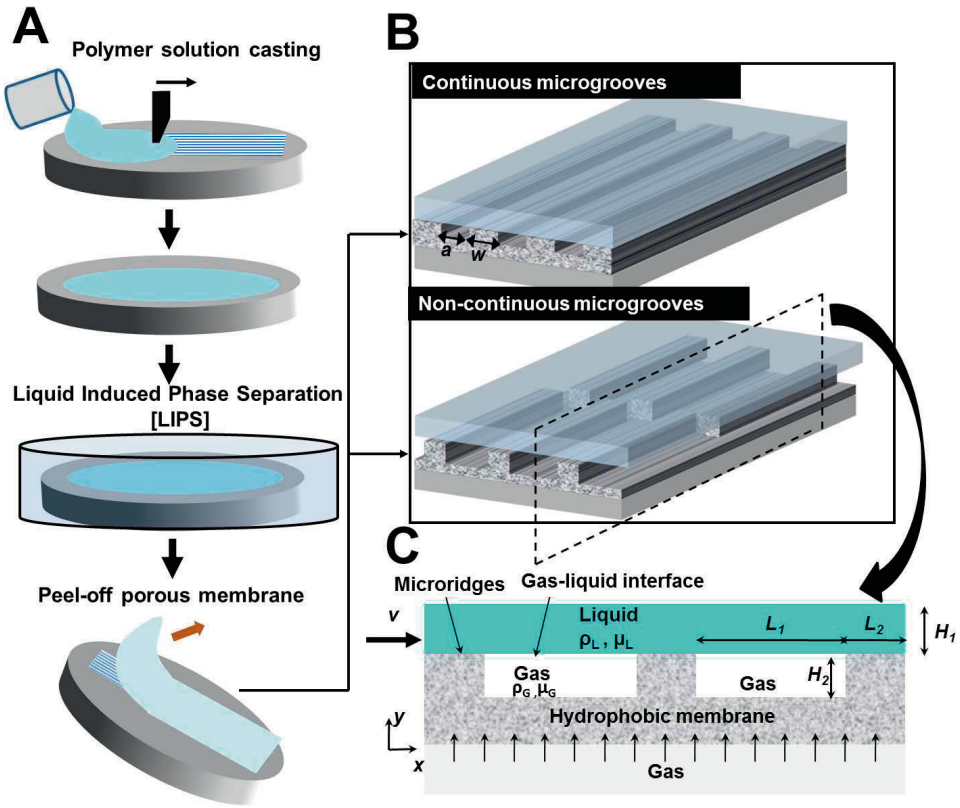

Figure 4.1: (A) Schematic representation of phase immersion micromolding to fabricate microgrooves on porous hydrophobic membranes (B) gas-liquid contacting principle showing liquid flow past continuous and non-continuous microgrooves (C) geometrical parameters for microgrooved membrane contactor.

gas-liquid contacting studies: flat, continuous and non-continuous (alternated) microgrooved surfaces, as shown in Fig. 4.1. The silicon wafers were micropatterned through photolithography methods combined with deep reactive ion etching (DRIE) in cleanroom facilities. Two types of microgrooves were obtained on the molds:

- Mold I: Grooves with a width of 25 μm, a height of 40 μm, a spacing of 75 μ m and a length of 50 mm.
- Mold II: as Mold I, but the groove is shifted 50 μm to the side after every 2 mm.

A solution of 20 *wt.*% PVDF in NMP (1-methyl-2-pyrrolidinone, 99 % extra pure, Acros) was prepared by mixing with a mechanical stirrer for 12 h at 70°C. The polymer

solution was then degassed for about 24 h at room temperature. Homogeneous and stable polymer solutions were cast on molds at controlled thicknesses (every 100 μm between 100 and 800 μm). Immediately after casting, the solution together with the microstructured mold was immersed in a coagulation bath consisting of pure ethanol (proanalysis grade, Merck) for 30 min. The membrane separates from the mold after a few minutes. The porous membrane was then taped to a glass plate to prevent it from curling up and left to dry in the fume hood overnight. The porous PVDF membrane replicates the microgrooves on the mold. Due to shrinkage in the phase separation and drying phases, the dimensions of the PVDF microchannels are slighly smaller than those on the mold.

4.2.2 Device fabrication

The porous membranes were incorporated in a gas-liquid contacting module consisting of two poly-methyl methacrylate (PMMA) plates. In these PMMA plates, separate gas and liquid microchannels were created with a CNC-mill (Sherline Inc.). The porous membrane is placed between these plates separating the gas and liquid channel. The liquid channel has a width and depth of 1 mm and a length of 5 cm. The gas channel is made wider and longer on both sides to assure complete coverage of the liquid channel by the porous membrane. Polyether ether ketone (PEEK) tubings (0.75 mm ID) and fittings (0.75 mm ID) from Upchurch Scientific were used for the connections.

4.2.3 Gas-liquid contacting in various configurations

Uptake of oxygen (obtained from Praxair, Belgium) into demineralized water is chosen as a gas-liquid contacting system (Fig.4.2). The setup consists of a programmable syringe pump (Harvard Apparatus, accuracy within 0.35% and reproducibility within 0.05%), an oxygen sensor (PreSens Fibox 3, accuracy $\pm$0.15% air saturation at 1% air-saturation, resolution 1 $\pm$0.05% air-saturation), a mass flow controller (Bronkhorst, accuracy $\pm$0.5% of reading plus $\pm$0.1% full scale) and a PC for data acquisition. The gas flow rates were controlled by the mass flow controller and water flow rates by gas-tight syringes using a programmable syringe pump. The feed water was injected at flow rates ranging from 0.05 mL/min to 7.5 mL/min ($0.83<Re<125$).

The experiments were started by feeding the microchannel with degassed (oxygen-free) water. Water was continuously bubbled with inert nitrogen gas (in a separate vessel)

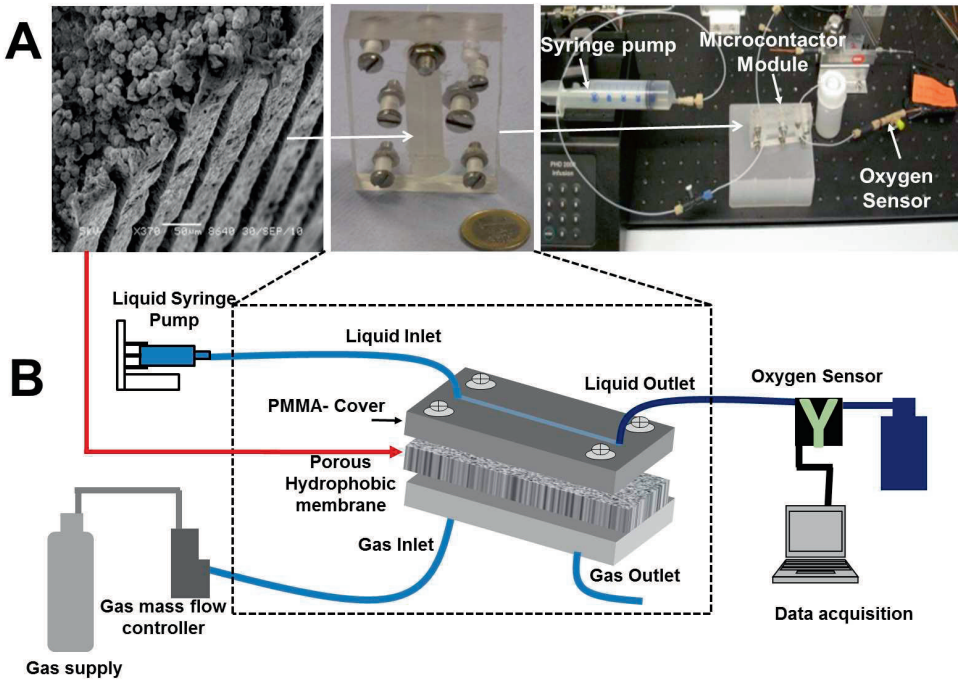

Figure 4.2: The gas-liquid contacting experiments (A) The experiments involves fabrication of microgrooved membranes, incorporating them into the module and setting-up for the gas uptake experiments. These steps are marked with "arrows" (B) The schematic representation of experimental set-up used for gas-liquid contacting.

in order to remove the oxygen. Throughout the experiments, the feed water was regularly monitored using the oxygen sensor to verify an oxygen free inlet. To attain a stable gas-liquid interface during the experiments, the gas was supplied at a fixed pressure through the gas-side inlet and the liquid flow rate was gradually increased until bubbles disappeared at the liquid-side of the microchannel. For higher liquid flow rates, the gas pressure required to establish a well-defined interface also increased. The oxygen concentration was measured for the exiting liquid when steady state was obtained.

The driving force for oxygen transfer varies with the axial position in the module. An expression for the overall oxygen flux at the microchannel outlet, N_o^i, can be expressed by,

$$N_o^i = \int \frac{Q(y) \cdot C(y) dy}{H_1 W} \tag{4.1}$$

Where, $Q(y)$ and $C(y)$ are liquid flow rate and oxygen concentration in the liquid, respectively and N_o^i represents outlet flux for corresponding microfluidic module (flat or microgrooved membrane contactor). Liquid channel height and width are denoted as H_1 and W, respectively. The experiments were carried out at ambient pressure and temperature.

4.2.4 Characterization

The morphology and dimensions of the porous membrane structures were analyzed by scanning electron microscope (SEM, JSM 5600LV, JEOL). The porous membranes were broken in liquid nitrogen for cross-section analysis. The membrane top surfaces and cross-sections were sputtered with a 30 nm gold layer (SCD040, Balzers Union).

Contact angles of the porous membrane structures are measured with an optical contact angle apparatus (OCA 20, Dataphysics). The water droplet of 5 μL is suspended on the surface with a speed of 2 μm/s. After initial stabilization of the droplet, the contact angle is measured.

An aqueous Methylene Blue (MB) solution ($\approx$ 200 mg/L) was prepared and pumped through the liquid inlet for a minimum time of 5 min for all liquid flow rates, in order to visualize the wetting behavior. After that, the membranes were taken out and allowed to dry for 3-4 h and then examined by optical microscopy (Zeiss Axiovert 40).

4.2.5 Micro Particle Image Velocimetry

The microfluidic channel (Fig. 4.3) was fabricated in a flat metal plate of steel with a depth of 500 μm and 1 mm width. Double sided tape ($\approx$ 100 μm) was used to bond the PVDF to the steel plate. The PVDF membrane film (300 μm) was cut to the width of the module and holes were made for liquid inlet and outlet. Before sealing the microchannel with glass microscopic slide (170 μm) on the ridge of the microfluidic chip, a cut-out in the double sided tape was made to keep the microchannel open. The microscope slide was then placed on the double sided tape sticking to the chip ridge. The metal chip containing gas-side channel, with inlet and outlet holes, is sticked to the other side of microfluidic channel using double sided tape.

The module was incorporated in a custom-made holder and connected to the tubing

(inner/outer diameter ≈ 0.5/1.6 mm). The module was positioned above the oil immersion Plan-Apochromat 100x objective (numerical aperture NA =1.4, 1 μm thick local plane) of an inverted optical microscope (Axiovert 40 CFL, Carl Zeiss BV). The oil is halogen-free and low in fluorescence (Immersol^{TM} 518F, Zeiss). The piezoelectric objective-lens positioning system (MIPOS 500, Piezosystem Jena GmbH) allows for positioning accuracy below 100 nm.

MilliQ water containing fluorescent polystyrene particles with a diameter of 0.3 μm (R300 red fluorescing microspheres, Duke Scientific Corporation) was injected into the microchannel by a syringe pump (PHD 2000, Harvard apparatus GmbH). Liquid flow rates were adjusted in the range of 0.3-17.5 μL/min (Re =0.008-0.5). Nitrogen gas feed rate was adjusted in the range of 120-220 μL/min corresponding to the changes in the liquid flow rates. A dual-head ND:YLF laser (Pegasus-PIV, New

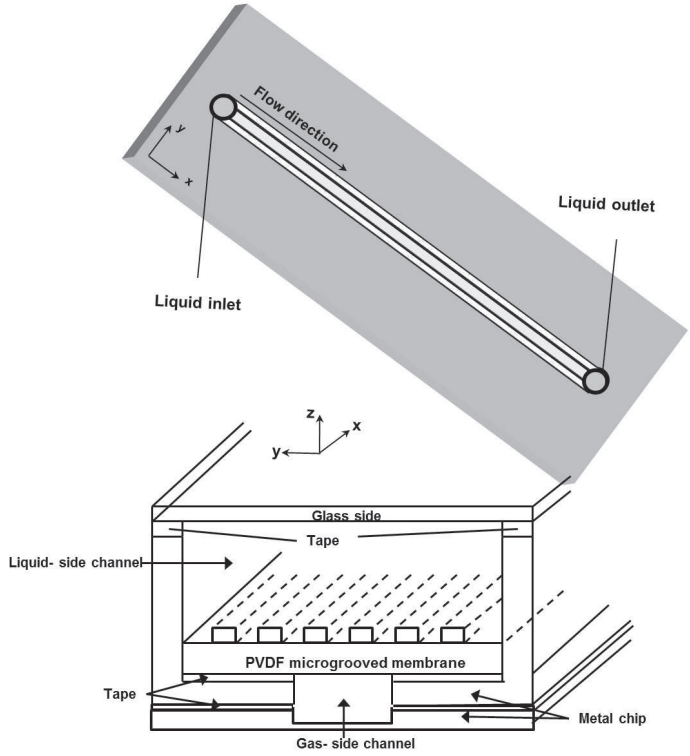

Figure 4.3: Illustration of the microfluidic chip used to study μPIV for the wetting behavior of liquid over microgrooved membranes at different operating conditions. It shows different stacks containing a liquid- and gas channel, microscopic glass slide and double sided tape.

Wave Research) producing green laser pulses with wavelength 527 nm was used to illuminate the particles. An external pulse delay generator (Model 565, Berkley Nucleonics Corporation) was used to trigger the laser. The time between two pulses is typically 6-15 ms depending on the flow rate. A high speed charged coupled device camera (Sensicam, PCO), fit with a 1/2× or 1× lens adapter, was used for imaging. The measurement principle including a sketch of the set-up was described previously [38].

After every measurement 200 image pairs were processed with DaVis imaging software (version 7.2.2.152, LaVision). To obtain time-average velocity profiles, a homemade μPIV post-processing sequence was run in Matlab R2007b [38].

4.3 Numerical methods

The momentum and mass balance equations were solved simultaneously under steady-state and laminar flow conditions to study hydrodynamics and mass transport. A three-dimensional model of a straight channel (5 mm long) was considered for flat and microgrooved membrane microchannel. The width of the microgroove and microridge are denoted as a and w, respectively. For non-continuous microgrooved membranes, the length and depth of the groove are denoted as L_1 and H_2, the liquid microchannel height is H_1 and the distance between two consecutive grooves (in flow direction) is denoted as L_2. For the numerical simulation, the following properties were considered: the density (ρ_L) and viscosity (η_L) of the liquid are similar to water (1000 kg m^{-3} and 0.001 Pa s, respectively), a maximum concentration of oxygen in water (saturation point at standard conditions) of 40 mg/L and a diffusion coefficient of oxygen in water of 1.9 $\times 10^{-9}$ m^2 s^{-1}.

In order to obtain a mathematically accurate model, the following assumption were made:

1. No mass transfer resistance in the membrane.
2. Flat meniscus and pores filled with gas for non-wetted condition.
3. Any other forces (gravitational and surface tension forces) are neglected.

The laminar flow of an incompressible fluid over a microgrooved membrane is governed

by the Navier-Stokes equations:

$$\rho_L(\boldsymbol{v}\cdot\nabla)\boldsymbol{v} = -\nabla P_L + \eta_L\nabla^2\boldsymbol{v} \tag{4.2}$$

together with the continuity equation:

$$\nabla\cdot\boldsymbol{v} = 0 \tag{4.3}$$

Here, ρ_L is the density, η_L is the viscosity and $\boldsymbol{v}$ is the velocity vector.

The mass balance equation involving convection and diffusion in the liquid is described as:

$$D\nabla^2 C_L = \boldsymbol{v}\cdot\nabla C_L \tag{4.4}$$

where D is the diffusion coefficient and C_L is the oxygen concentration in water.

A fully developed laminar flow profile has been implemented at the microchannel inlet and the outlet is kept at normal pressure. There will be zero gas concentration at the microchannel inlet and convective flux will be implemented at the outlet boundary. The microchannel walls (solid-liquid) are "no-slip" boundaries.

$$v_x = v_y = 0, \qquad \text{for all solid-liquid interfaces} \tag{4.5}$$

Along the membrane surface ($y = H_1$), both gas-liquid and liquid-solid interface can apply (depends on continuous or non-continuous microgrooves). A gas-liquid interface is described as a shear-free boundary (velocity of gas and liquid at the interface are equal):

$$v_x = v^i_{x,g} = v^i_{x,l} \tag{4.6}$$

where, $v^i_{x,g}$ and $v^i_{x,l}$ represents gas and liquid interface velocity in x-direction, respectively.

4.4 Results and discussion

4.4.1 Characterization of the porous membrane

Figure 4.4 shows the SEM images of the surface and cross-section of the microgrooved membranes. SEM images of various structures in PVDF membranes provide insight in the morphology (i.e. porosity, roughness and porous structure) and dimensions of the membrane microchannels. The features of the mold are very well represented on the PVDF membranes.

Figure 4.4A shows the SEM images of flat PVDF membranes in different magnifications. Porous membranes have narrow pore size distribution with average pore size of 7.4 μm $\pm$ 0.7 μm (obtained from SEM images). The membranes are highly porous and contain inter-connected pores. The continuous microgrooved membrane is shown in Fig. 4.4B, which demonstrates that micropatterns from the mold are nicely replicated in the membranes. A closer look at the structures revealed that the distance between the grooves (50 μm) is slightly smaller than the one on the mold (75 μm). This is due to the shrinkage during the phase inversion process [37]. Table 4.1 shows the average values of the dimensions of PVDF membranes.

Compared to Peters [39], the shrinkage values are found to be somewhat lower and pores have a more open structure. Since all conditions were kept the same except for the coagulation bath (in this work pure ethanol is used instead of 50:50 wt% water:NMP), the differences in the membrane structure are attributed to the phase-separation step. The non-continuous microgrooved membrane can be seen in Fig. 4.4C. The dimensions of the non-continuous microgrooved membranes are similar to the dimensions of continuous microgrooves.

Table 4.1: Dimensions of different features of microgrooved membrane (continuous and non-continuous)

Membrane feature	Dimensions on molds	Average dimensions of membrane	Shrinkage (%)
Width of the grooves	25 μm	24 μm	4
Height of the grooves	40 μm	38 μm	5
Distance between the grooves	75 μm	48 μm	36

The water contact angle for the flat membrane was measured to be 128.2°$\pm$3.4°. The measured contact angles for these PVDF membranes are higher than previous work from Peters [39], which is due to the difference in membrane structure.

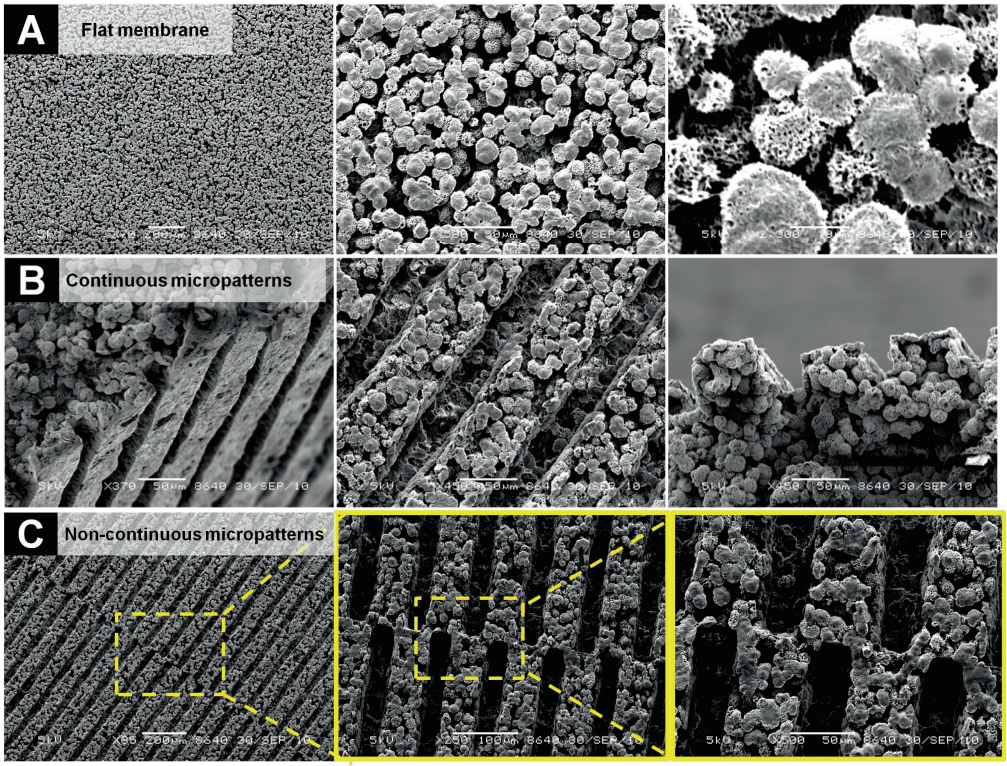

Figure 4.4: SEM images of the channels in porous PVDF membrane. (A) Microporous flat PVDF surface (B) Continuous microgrooved PVDF membrane surface with 24 μm width, 38 μm depth and 48 μm ridge width (C) Non-continuous microgrooved PVDF membrane surface with 24 μm width, 38 μm depth, 2 mm length and 48 μm ridge width.

4.4.2 Gas uptake experiments in membrane microcontactor

Figure 4.5 presents the outlet oxygen concentration for a continuously microgrooved membrane for both experiments and simulations (oxygen saturation concentration is 40 mg/L at 25°C and 1 bar). For low *Re* (below 5), the liquid gets saturated almost completely. The measured oxygen concentrations were slightly different compared to the simulated concentrations at high and low liquid flow rates. These differences are due to the experimental error caused by the oxygen sensor sensitivity.

The measured oxygen uptake when using flat and microgrooved membranes allow to

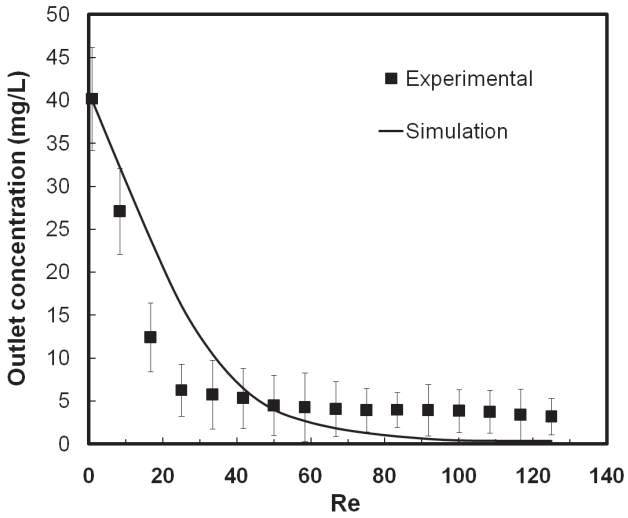

Figure 4.5: Outlet oxygen concentration against Re for continuous microgrooved membrane module; experimental values are shown in symbols and simulation values are shown in line.

calculate the flux enhancement (E):

$$E = \frac{(N_o^m - N_o^f)}{N_o^f} \tag{4.7}$$

where N_o^m and N_o^f are the outlet flux for microgrooved and flat membrane respectively. The flux enhancement for a continuous microgrooved membrane compared to a flat membrane is shown in Fig. 4.6. The results, both from the COMSOL models and oxygen absorption experiments, show higher oxygen absorption for the microgrooved membrane compared to the flat membrane. It can be seen from the plot that the experimental flux enhancement increases sharply after Re=50. This increase in flux enhancement can be explained due to enhanced mass transfer caused by an increased gas-liquid interface velocity (slip condition). The numerical results also show reasonable agreement with the experimental observations.

Interestingly, during subsequent decreasing Re experiments, hysteresis was observed. The flux enhancement was much lower for Re in the range of 50 to 75. The hysteresis could be explained by wetting of the grooves at higher Reynolds number. This causes a change in the oxygen diffusion length and consequently reduces the oxygen mass transfer rate. The influence of microgroove wetting on the performance of the

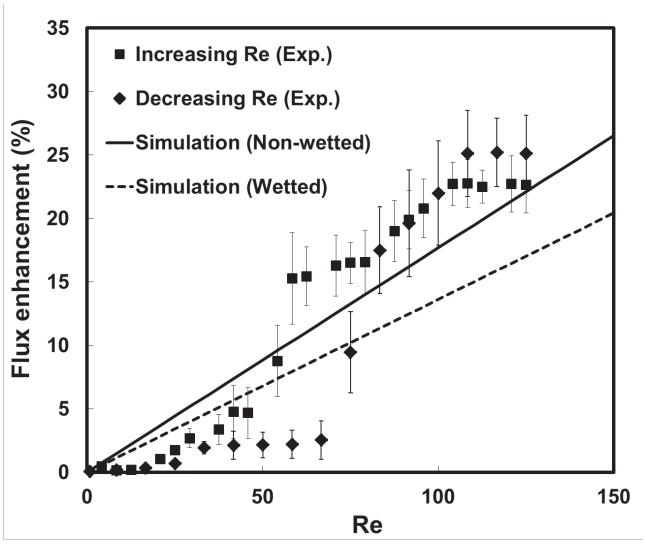

Figure 4.6: Flux enhancement *vs* Re for continuous microgrooved membrane module. The values are shown for increasing and decreasing Reynolds number. The experimental values are shown in dots and simulation values are shown in line.

membrane module was studied numerically as well Fig. 4.6. The numerical simulation results display a reduced flux enhancement (for $Re \geq 50$) due to wetting of the grooves.

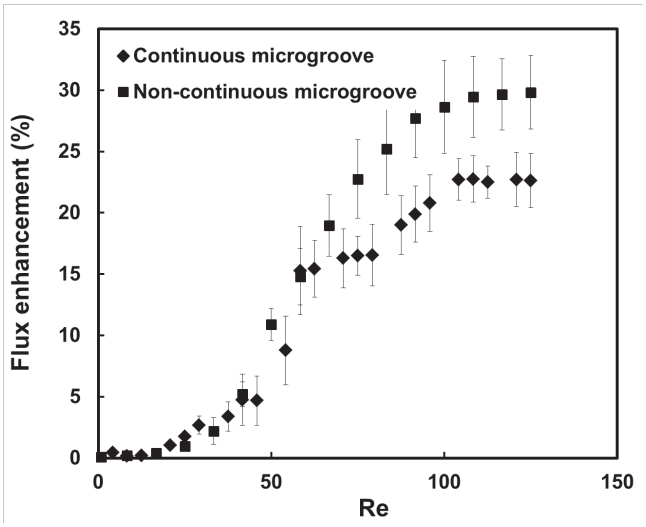

Figure 4.7: Flux enhancement *vs* Re for continuous and non-continuous microgrooved membrane module. The values are shown for increasing Reynolds number.

Figure 4.7 illustrates the flux enhancement for a non-continuous and a continuous microgrooved membrane. The enhancement in flux for non-continuous grooves is approximately 20-30 % for Reynolds number higher than 75. Due to perturbations in the shear-free interface velocity, displacements perpendicular to the flow direction appears. These displacements generate convective flow near the gas absorbing porous wall, which leads to enhanced gas uptake compared to the continuously microgrooved membrane.

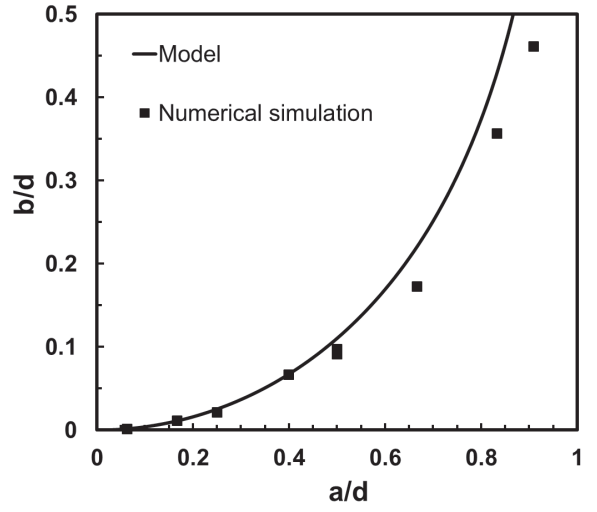

Figure 4.8: Numerical results showing values of dimensionless slip length b/d as a function of the dimensionless microgroove width. The results are compared with the analytical expression for b/d, from literature [40], represented by Eq.4.8.

4.4.3 Details of the gas-liquid interface

Non-wetted grooves give rise to local slip velocities and to validate results with analytical model [40], we have to consider two important geometric parameters for the different configurations: the microgroove width (a) and microridge width (w). The cavity fraction is represented by a/d (shown in Fig. 4.1), where $d = a + w$. Philip showed that for fully developed laminar flow through a parallel-plate channel and with a vanishing shear-stress at the gas-liquid interface, the slip-length, b, can be expressed

as:

$$\frac{b}{d} = \frac{1}{\pi} ln \left[\frac{1}{cos\left(\frac{a}{d}\frac{\pi}{2}\right)} \right] \tag{4.8}$$

With Eq. 4.8, it is possible to quantify slip-length characteristics with a single curve, which allows validation of our numerical results for the limiting case of zero shear-stress at the gas-liquid interface.

The overall shear stress at the gas-liquid interface in microchannels is strongly dependent on the membrane microgroove ridge and groove widths [40]. The effective slip length is calculated from the numerical results and plotted against the microgroove width (Fig. 4.8). The analytic solution of Philip given by Eq. 4.8 is also presented [40]. The numerical results show very good agreement with the solution from Philip [40], not surprisingly as both assume a flat gas-liquid meniscus.

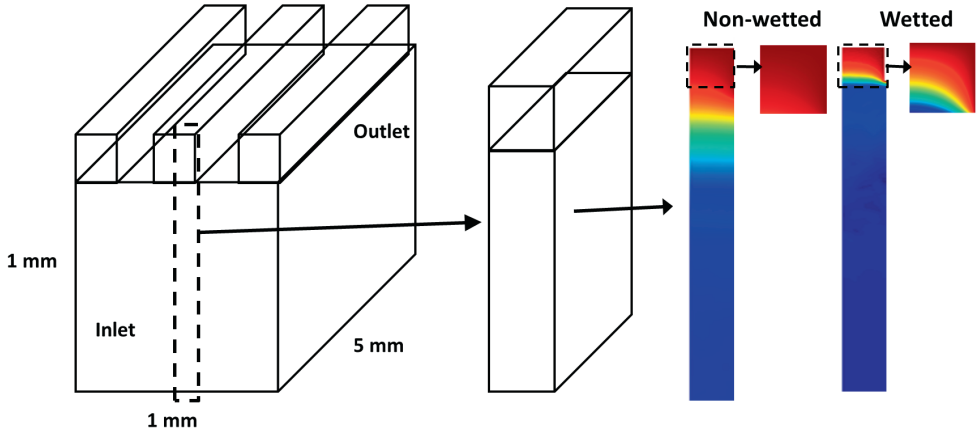

Figure 4.9: The numerical simulations showing concentration profiles in a channel with two test cases: wetted and non-wetted mode (Re=25, D= 1.9 × 10^{-9} m^2/s for 25 μm groove width and 40 μm groove height). The oxygen concentration in the microgrooves is shown in selected inset images.

To investigate the oxygen absorption in water using different membranes (continuous and non-continuous microgrooves), numerical simulations were performed at flow rates ranging from 0.83<Re<125. The oxygen concentration and fluid flows were investigated to verify our experimental observations. Two different cases were considered: wetted and non-wetted under different flow conditions.

The outlet oxygen concentration vary with the liquid flow rate due to changes in the

Péclet number. Typical numerical simulation results for continuous microgrooved membranes, with and without wetting are shown in Fig.4.9. In the wetted microgrooves, the average velocity can be calculated from the velocity profile, is needed to determine Pe for various inlet Re. For Re=0.83 (0.05 μL/min) and 125 (17.5 μL/min), values of Pe are 0.24 and 0.11, respectively which suggests wetted microgrooves offer mass transfer resistance to oxygen uptake in water.

4.4.4 Flow along microgrooved membranes

To investigate the effect of the liquid flow rate on the membrane microgroove wetting, an aqueous methylene blue (MB) solution was pumped through the microchannel for

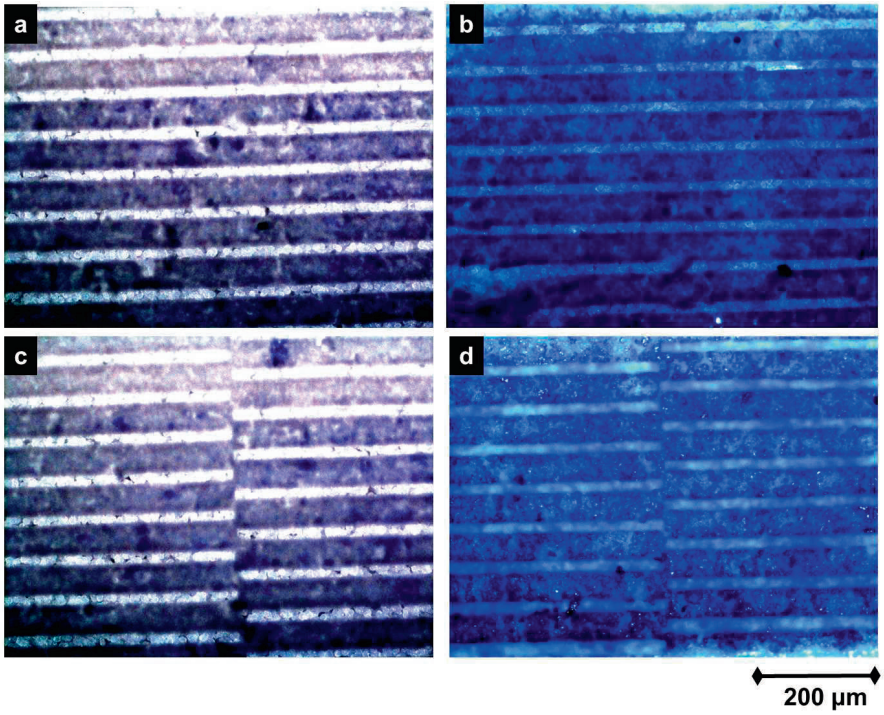

Figure 4.10: Optical microscope images of the membranes showing wetting of the grooves. (a) Continuous grooves at low liquid flow rate (Re=8.30) showing liquid remaining in the non-wetted (Cassie-Baxter) state (b) Continuous grooves at high liquid flow rate (Re=120.83) showing wetting of the grooves (c) Non-continuous microgrooved membrane surface with low liquid flow rate (Re=8.30) (d) Non-continuous microgrooved membrane surface with high liquid flow rate (Re=120.83) showing wetting of the grooves.

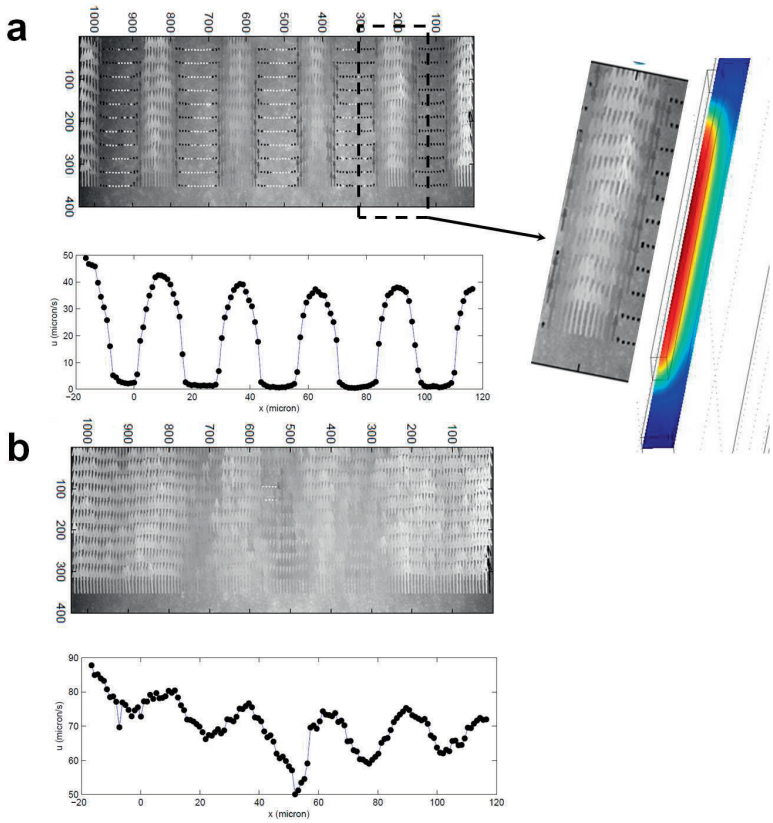

Figure 4.11: (a) MicroPIV results showing one frame visualizing the flow (5 μL/min) over a microgrooved PVDF membrane surface at a height z=5 μm from the microgroove ridge (top) and the time- and space-averaged velocities in x-direction extracted from this (bottom). (b) Particle velocity profile at a flow rate of 17.5 μL/min showing little difference in water velocity over microgrooves and microridges (top) and time- and space-averaged velocities (bottom).

5 min with increasing flow rates. After every step change in Reynolds number, the MB stained membrane was taken out and observed by optical microscopy (Fig.4.10). The same procedure was followed for decreasing Reynolds numbers.

As shown in Fig.4.10 a and c, the water flowing above microgrooves remains in the Cassie-Baxter state for low flow rates where the differential pressure across the gas-liquid interface has not reached the wetting pressure. However, when the differential pressure exceeds the wetting pressure, water penetrates into the grooves (Wenzel state) (Fig.4.10b and d). The observation of water wetting the grooves explains the hysteresis

behavior in flux enhancement.

Micro-PIV measurements were performed at liquid flow rates ranging from 0.3-17.5 μL/min (0.008<Re<0.5). These conditions resulted in completely non-wetted and wetted grooves for lower and higher flow rates respectively. Figures 4.11a and b show the plots containing information about the velocity profiles for two different flow rates (5 and 17.5 μL/min) at the same observation plane (5 μm from the micropattern ridge). For low liquid flow rates (Fig. 4.11a), the grooves are gas filled and a shear-free interface is realized giving enhanced liquid velocity. Figure 4.11a (bottom) shows averaged velocities in x-direction for each position along the y-axis at a given height z (5 μm). It displays zero liquid velocity over the microgroove ridge and a liquid velocity of 40 μm/s over the gas filled groove.

The velocity of water flowing over wetted microgrooves (Figure 4.11b) is not significantly higher than the velocity of water flowing over microridges. The completely wetted membrane surface (Wenzel state) is also observed during the experiments. The higher averaged liquid velocity [Fig. 4.11b (bottom)] is observed due to higher liquid flow rates.

4.5 Conclusions

The main goal of this work was to design a microgrooved membrane for gas-liquid contacting that was easy to fabricate, efficient and simple. This work presents a system which can be employed in effective gas-liquid contacting. By this approach, it is possible to reduce the mass transport limitations commonly observed in conventional gas-liquid contacting system. An enhancement in flux up to 20-30 % has been observed. The liquid flow patterns and wetting behavior of the porous microgrooved hydrophobic membranes have been analysed experimentally and numerically. The flux is enhanced at higher liquid flow rates due to slip flow at the gas-liquid interface. However when the microgrooves are wetted the mass transport decreases. Microgrooved membranes offer a promising alternative to conventional membranes because of a significant enhancement in constituent transport. The experiments also show the limits of the flow regimes characterized by observing the position of gas-liquid interface. According to both the numerical simulations and experimental observations of gas-liquid contacting, we have shown that it is possible to increase the gas uptake in liquid by merely structuring the membrane surface.

4.6 Acknowledgments

This work was financially supported by Stichting voor de Technische Wetenschappen (STW, Project 07569) in the Netherlands. The authors also greatly acknowledge Elif Karatay (SFI/TNW) for mold preparation and Álvaro Gómez Marín (POF/TNW) for μPIV analysis and technical support.

4.7 References

[1] V. Hessel, H. Löwe and F. Schönfeld; *Micromixers: a review on passive and active mixing principles*; Chem.Eng.Sci **60** (2005) 2479–2501

[2] K. Jensen; *Microreaction engineering–is small better?*; Chemical Engineering Science **56** (2) (2001) 293–303

[3] K. Jähnisch, V. Hessel, H. Löwe and M. Baerns; *Chemistry in microstructured reactors*; Angewandte Chemie International Edition **43** (4) (2004) 406–446

[4] M. Kreutzer, F. Kapteijn, J. Moulijn, C. Kleijn and J. Heiszwolf; *Inertial and interfacial effects on pressure drop of Taylor flow in capillaries*; AIChE journal **51** (9) (2005) 2428–2440

[5] J. Heiszwolf, M. Kreutzer, M. van den Eijnden, F. Kapteijn and J. Moulijn; *Gas-liquid mass transfer of aqueous Taylor flow in monoliths*; Catalysis today **69** (1-4) (2001) 51–55

[6] T. Gervais and K. Jensen; *Mass transport and surface reactions in microfluidic systems*; Chemical engineering science **61** (4) (2006) 1102–1121

[7] N. Shao, A. Gavriilidis and P. Angeli; *Flow regimes for adiabatic gas-liquid flow in microchannels*; Chemical Engineering Science **64** (11) (2009) 2749–2761

[8] J. Atencia and D. Beebe; *Controlled microfluidic interfaces*; Nature **437** (7059) (2004) 648–655

[9] T. Squires and S. Quake; *Microfluidics: Fluid physics at the nanoliter scale*; Reviews of modern physics **77** (3) (2005) 977

[10] A. Gunther and K. Jensen; *Multiphase microfluidics: from flow characteristics to chemical and materials synthesis*; Lab on a Chip **6** (12) (2006) 1487–1503

[11] V. Hessel, P. Angeli, A. Gavriilidis and H. Löwe; *Gas-liquid and gas-liquid-solid microstructured reactors: contacting principles and applications*; Industrial & Engineering Chemistry Research **44** (25) (2005) 9750–9769

[12] A. Stroock, S. Dertinger, A. Ajdari, I. Mezić, H. Stone and G. Whitesides; *Chaotic mixer for microchannels*; Science **295** (5555) (2002) 647

[13] R. Liu, M. Stremler, K. Sharp, M. Olsen, J. Santiago, R. Adrian, H. Aref and D. Beebe; *Passive mixing in a three-dimensional serpentine microchannel*; Microelectromechanical Systems, Journal of **9** (2) (2002) 190–197

[14] H. Stone, A. Stroock and A. Ajdari; *Engineering flows in small devices*; Annu. Rev. Fluid Mech. **36** (2004) 381–411

[15] A. Kamholz, B. Weigl, B. Finlayson and P. Yager; *Quantitative analysis of molecular interaction in a microfluidic channel: the T-sensor*; Anal. Chem **71** (23) (1999) 5340–5347

[16] N. Nguyen and Z. Wu; *Micromixersa review*; Journal of Micromechanics and Microengineering **15** (2005) R1

[17] T. Fujii, Y. Sando, K. Higashino and Y. Fujii; *A plug and play microfluidic device*; Lab on a Chip **3** (3) (2003) 193–197

[18] H. Mao, T. Yang and P. Cremer; *A microfluidic device with a linear temperature gradient for parallel and combinatorial measurements*; J. Am. Chem. Soc **124** (16) (2002) 4432–4435

[19] M. Oddy, J. Santiago and J. Mikkelsen; *Electrokinetic instability micromixing*; Anal. Chem **73** (24) (2001) 5822–5832

[20] Z. Yang, S. Matsumoto, H. Goto, M. Matsumoto and R. Maeda; *Ultrasonic micromixer for microfluidic systems*; Sensors and Actuators A: Physical **93** (3) (2001) 266–272

[21] D. Bothe, C. Stemich and H. Warnecke; *Fluid mixing in a T-shaped micro-mixer*; Chemical engineering science **61** (9) (2006) 2950–2958

[22] F. Bessoth, A. deMello and A. Manz; *Microstructure for efficient continuous flow mixing*; Analytical communications **36** (6) (1999) 213–215

[23] L. Austin and J. Seader; *Fully developed viscous flow in coiled circular pipes*; AIChE Journal **19** (1) (1973) 85–94

[24] F. Jiang, K. Drese, S. Hardt, M. Küpper and F. Schönfeld; *Helical flows and chaotic mixing in curved micro channels*; AIChE journal **50** (9) (2004) 2297–2305

[25] A. Sudarsan and V. Ugaz; *Fluid mixing in planar spiral microchannels*; Lab Chip **6** (1) (2005) 74–82

[26] P. Howell, D. Mott, J. Golden and F. Ligler; *Design and evaluation of a Dean vortex-based micromixer*; Lab on a Chip **4** (2004) 663–669

[27] D. Öner and T. McCarthy; *Ultrahydrophobic surfaces. Effects of topography*

length scales on wettability; Langmuir **16** (20) (2000) 7777–7782

[28] A. Torkkeli, J. Saarilahti, A. Haara, H. Harma, T. Soukka and P. Tolonen; *Electrostatic transportation of water droplets on superhydrophobic surfaces*; in *Micro Electro Mechanical Systems, 2001. MEMS 2001. The 14th IEEE International Conference on*; IEEE; ISBN 0780359984 (2001) pages 475–478

[29] J. Kim and C. Kim; *Nanostructured surfaces for dramatic reduction of flow resistance in droplet-based microfluidics*; in *Micro Electro Mechanical Systems, 2002. The Fifteenth IEEE International Conference on*; IEEE; ISBN 0780371852 (2002) pages 479–482

[30] J. Bico, U. Thiele and D. Quéré; *Wetting of textured surfaces*; Colloids and Surfaces A: Physicochemical and Engineering Aspects **206** (1-3) (2002) 41–46

[31] J. Ou, G. Moss and J. Rothstein; *Enhanced mixing in laminar flows using ultrahydrophobic surfaces*; Physical Review E **76** (1) (2007) 16304

[32] J. Ou and J. Rothstein; *Direct velocity measurements of the flow past drag-reducing ultrahydrophobic surfaces*; Physics of Fluids **17** (2005) 103606

[33] D. Maynes, K. Jeffs, B. Woolford and B. Webb; *Laminar flow in a microchannel with hydrophobic surface patterned microribs oriented parallel to the flow direction*; Physics of Fluids **19** (2007) 093603

[34] D. Hassell and W. Zimmerman; *Investigation of the convective motion through a staggered herringbone micromixer at low Reynolds number flow*; Chemical engineering science **61** (9) (2006) 2977–2985

[35] J. de Jong, M. Geerken, R. Lammertink and M. Wessling; *Porous Microfluidic Devices–Fabrication and Applications*; Chemical Engineering & Technology **30** (3) (2007) 309–315

[36] P. Tsai, A. Peters, C. Pirat, M. Wessling, R. Lammertink and D. Lohse; *Quantifying effective slip length over micropatterned hydrophobic surfaces*; Physics of Fluids **21** (2009) 112002

[37] L. Vogelaar, R. Lammertink, J. Barsema, W. Nijdam, L. Bolhuis-Versteeg, C. Van Rijn and M. Wessling; *Phase separation micromolding: a new generic approach for microstructuring various materials*; Small **1** (6) (2005) 645–655

[38] C. Pirat, A. Naso, E. Van Der Wouden, J. Gardeniers, D. Lohse and A. Van Den Berg; *Quantification of electrical field-induced flow reversal in a microchannel*; Lab Chip **8** (6) (2008) 945–949

[39] A. Peters; *Micro-patterned interfaces affecting transport through and along membranes*; Ph.D. thesis (2008)

[40] J. Philip; *Flows satisfying mixed no-slip and no-shear conditions*; Zeitschrift für Angewandte Mathematik und Physik (ZAMP) **23** (3) (1972) 353–372

CHAPTER 5

Modeling of gas-liquid reactions in porous membrane microreactors

A revised version of this chapter has been prepared for publication:

Jigar M. Jani, H.C. Aran, M. Wessling, Rob G.H. Lammertink *Modeling of gas-liquid reactions in porous membrane microreactors*

Abstract

This work provides a numerical model studying mass transport and heterogeneously catalyzed reactions in a porous membrane microreactor. The hydrogenation of nitrite over a Pd catalyst was used as a model reaction. The influence of liquid flow rates, initial nitrite concentration and catalytic membrane layer thickness (wetting thickness) on the conversion was studied. Firstly, a kinetic model was implemented based on the correlations available for reaction kinetics from literature. The results were validated using experimental results and it was found that the process is best described by Langmuir-Hinshelwood reaction kinetics. Secondly, to obtain an optimized reactor geometry, boundary conditions were derived, which represent the reactant concentration at the microreactor inner wall as a function of catalytic layer properties. An optimum in conversion was found for varying catalytic membrane layer thickness. The initial increase in conversion with increasing catalytic layer thickness is due to enhanced catalyst area. The conversion later reduces due to gaseous reactant mass transfer limitation, for even thicker layers. This study gives detailed understanding of the reaction and mass transfer taking place in membrane microreactors. It also provides optimized reactor configurations, which allows for more efficient catalyzed gas-liquid reaction processes.

5.1 Introduction

Membrane based operations including separations, reactions and contacting have received significant attention in the last few decades. They offer advantages, such as ease of operation and scale-up, low operational cost, high selectivity and affordable energy requirements. Membrane reactors for gas-liquid processes are exploited to achieve stable gas-liquid interfaces [1, 2]. Recently, porous hydrophobic membrane microreactors were employed for effective gas-liquid contacting [3]. Catalytic membrane microreactors are useful for multiphase reaction systems involving gas-liquid-solid (G-L-S) [4]. This design provides a way to achieve less emission, controlled chemistry and enhanced efficiency [5–8]. They also help to reduce diffusional resistance to mass transfer, giving higher catalytic activities compared to traditional three-phase reactors e.g. slurry reactors, packed bed and trickle-bed reactors. An experimental study confirmed these improvements mainly due to the intense multiphase contacting [9]. Several reactions have been investigated including the removal of nitrite and nitrate ions from ground water [10–14]. Such membrane reactors exploit mainly three functions: (i) facilitate contact between gas and liquid phases (ii) provide support to immobilize the catalyst (iii) separate inlet conditions for the reactants, providing flexibility regarding gas and liquid flow rates.

Hollow fiber membrane reactors provide a suitable configuration for catalyst immobilization. The reactants are separated from each other by a porous hollow fiber membrane. The resulting catalytic reaction zone is usually 8-70 μm thick [15]. Liquid reactants come into direct contact with the gaseous reactants in the catalytic regions of the membrane reactors [14, 15].

Gas-liquid contacting and catalytic reactions in membrane contactors and reactors has been modeled before [16–18]. Wang et al. developed a theoretical model to understand the gas-liquid contacting under two operating conditions of fully wetted and non-wetted mode in microporous hollow fiber membranes [16]. Their simulation results showed that gas (CO_2) absorption in the non-wetted mode of operation is six times higher than those of the wetted mode of operation. They reported 20 % reduction in overall mass transfer coefficient for 5 % wetted membrane pores. Kumar et al. studied the catalytic reactions on both sides (tube and shell side) of tubular membrane reactors [17]. They implemented the model for the study of evaluation of different catalysts and catalytic dehydrogenation of ethylbenzene to produce styrene in a tubular membrane reactor. Negy developed a mathematical model that predicts mass

transfer rates and the concentration distribution as a function of the physiochemical parameters, that involves diffusive and convective flow through the catalytic membrane layer [18]. Li and Tan [19] developed theoretical models for membrane reactors to describe mass transfer and chemical reactions taking place either in the hollow fiber lumen or in the shell side. Their results suggested axial dispersion plays crucial role for the reactions taking place in the shell-side, but only for Pe>40. They also showed that reaction kinetic parameters can be obtained once the reaction mechanism is confirmed. Gervais et al. have performed a detailed study to identify the parameters that affect the mass transfer and surface reactions in microfluidic devices [20]. Using analytical and modeling approaches, they characterized the transport mechanism towards the stationary surfaces in the absence of a boundary layer and proposed methods to obtain the diffusion/reaction mass transfer coefficient. These mass transfer coefficients can be used to obtain bulk and surface concentrations along the device. The formation of moving concentration fronts in long channels was also analyzed and its propagation velocity was correlated with experimental parameters [20]. The interplay between the flow and interfacial mass transfer is an important factor for systems involving reactive boundaries [21]. There have been several attempts using two-dimensional (2-D) models, where both axial and radial concentration profiles of the reactants are obtained [22–26]. There are multiple ways to perform such 2-D simulations such as finite different [27], finite element [28] or orthogonal collocations.

In this work, two-dimensional CFD simulations are performed to study the effects of reaction parameters (i.e. initial reactant concentrations, flow rates, reaction rate constant) and geometrical parameters (i.e. porosity, tortuosity and wetted catalytic layer thickness) on the microreactor performance. An analytical boundary condition is developed representing the concentration profiles for liquid and gaseous reactants along the axial position of the inner wall of the microreactor.

From the design perspective, the numerical simulations and mathematical model developed here represent an important tool for analyzing gas and liquid transport/reaction in a porous membrane microreactor. It allows to:

- Predict diffusive and convective mass transfer phenomena and catalytic chemical reactions in membrane microreactors.
- Evaluate gas and liquid concentration profiles along the axial length of the membrane microreactor.
- Analyze the correct description of the reaction rate expression.

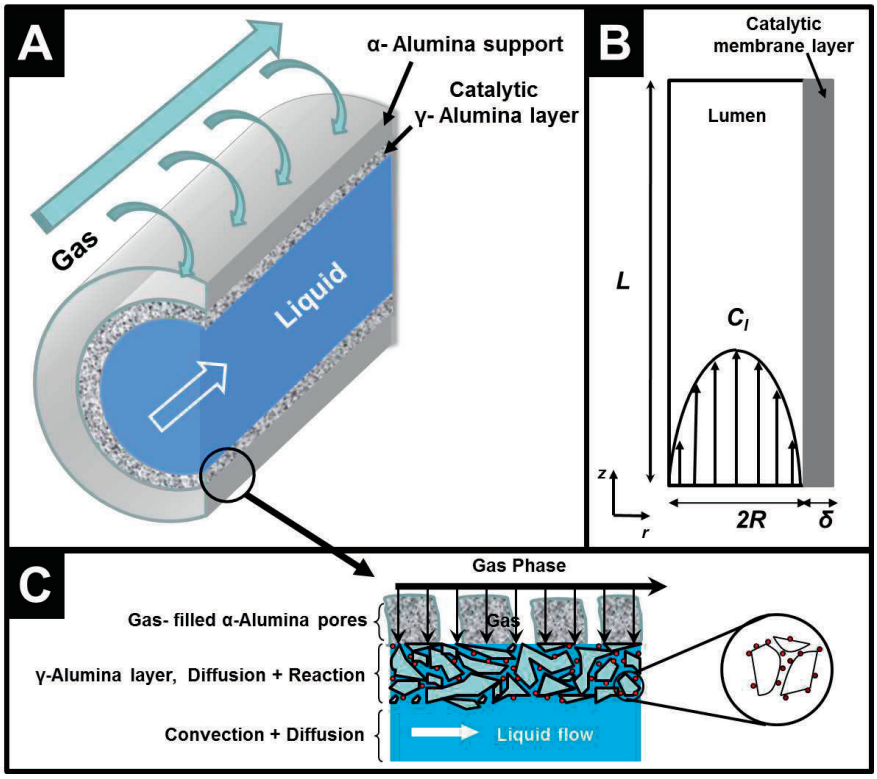

Figure 5.1: (A) Schematic representation of a gas-liquid-solid reaction in a hollow fiber membrane microreactor (B) Two-dimensional representation of computational domain of hollow fiber membrane microreactor (C) Illustration of tubular membrane reactor.

- Design a porous membrane microreactor to maximize the conversion.

5.2 Modeling of reaction kinetics

In order to describe the mass transfer, the reaction rate expression has to be defined accurately. The schematic representation of the microreactor concept is presented in Figure 5.1. The liquid phase, containing one of the reactants, flows through the lumen side of the porous reactor. Gaseous reactants diffuse from the shell side to meet the liquid at the catalyst surface in the wetted γ-Al_2O_3 layer where the reaction takes place.

The concept of the reactor has been successfully implemented for the hydrogenation of nitrites in water [14]. The heterogeneously catalyzed hydrogenation of nitrite ions (NO_2^-) over palladium (Pd) catalyst in aqueous phase is described as [9–12, 29, 30]:

$$2NO_2^- + 3H_2 \overset{Pd/membrane}{\rightarrow} N_2 + 2OH^- + 2H_2O \tag{5.1}$$

Ideally, nitrites are converted to nitrogen at ambient reaction conditions. The experimental investigation on the kinetics of the hydrogenation of nitrites was recently performed [11, 13]. A detailed kinetic study involving catalyst activity and selectivity measurements, over wide range of reactant concentrations and operating conditions, was also performed [10]. They found that the hydrogenation of nitrite follows Langmuir-Hinshelwood (LH) reaction kinetics. Aran et al. found that the hydrogenation of nitrites in porous catalytic membrane microreactors is independent of hydrogen concentration [14]. Thus, for the LH reaction rate expression, the nitrite disappearance rate is assumed to be independent of hydrogen concentration in this study, giving the following expression:

$$R_{LH} = k_{LH} \frac{K_{ads} C_l}{1 + K_{ads} C_l} \tag{5.2}$$

where R_{LH} is the LH reaction rate, K_{ads} is adsorption coefficient, k_{LH} is the dimensionless LH reaction rate constant, C_l is the nitrite concentration.

The experimental results of the catalytic reduction of nitrite over Pd catalyst were obtained in terms of conversion and selectivity over a wide range of initial reactant concentrations [11, 31]. Several experimental works [11, 31] have reported the following kinetic rate expression:

$$R_s = k_s \cdot C_l^n \cdot C_g^m \tag{5.3}$$

where R_s is Power-Law reaction rate, k_s is reaction rate constant, n is the liquid hydrogenation reaction order and m is the gaseous reaction order. Chinthaginjala et al. [11] have reported the reaction order for nitrite (n) to be around 0.7 in their work. This suggests that the surface coverage of nitrite is relatively low. Matatov-Meyal et al. [31] have reported the reaction order to vary from 0 to 1 for nitrite and hydrogen. This corresponds to zero-order (saturated system) and first-order (diluted system) adsorption on the catalyst surface. Normally, the initial reactant concentration is

at millimolar scale, and the kinetic rate expression can be simplified to a first-order equation for nitrite.

To gain accurate kinetic parameters for Eqs.(5.2) and (5.3), numerical simulations are performed and validated with experimental results. All the governing equations described in section 5.3 are solved simultaneously and the results are discussed in section 5.4.

5.3 A catalytic membrane microreactor model

This section comprises the mass balance equations for transport through the lumen of hollow fiber with an immobilized catalytic layer. A schematic representation of the membrane microreactor is shown in Figure 5.1a and b. The reactants enter through the fiber lumen under laminar conditions and then diffuse into the catalytic porous γ-Al_2O_3 layer. The pores of the α-Al_2O_3 support are filled with gas and the γ-Al_2O_3 layer is wetted with liquid (Figure 5.1c). The catalytic reaction takes place on the surface of immobilized catalyst in the γ-Al_2O_3 layer. A radial concentration gradient will build up in the liquid phase, which should be balanced by the diffusive flux at the inner wall of the hollow fiber.

The model under steady-state and isothermal conditions is described with the following assumptions:

- Parabolic velocity profile in the fiber lumen
- Porous support exhibits no catalytic activity
- Uniform pore size distribution
- Support is fully gas filled (α-Al_2O_3), catalytic layer is liquid filled (γ-Al_2O_3)

The steady-state mass balance in cylindrical co-ordinates for the hollow fiber membrane microreactor can be written as follows:

$$u_z \frac{\partial C_l}{\partial z} = D_l \left(\frac{\partial^2 C_l}{\partial r^2} + \frac{1}{r} \frac{\partial C_l}{\partial r} \right) \qquad (0 < r < R) \tag{5.4}$$

where z is the axial position (m), u_z is the axial liquid velocity (m/s), D_l is the diffusion coefficient for reactants in the liquid (m^2/s), r is the radial position (m). The

parabolic velocity profile in the liquid side is given by:

$$u_z = 2U\left[1 - \left(\frac{r}{R}\right)^2\right] \tag{5.5}$$

where U is the average liquid velocity (m/s) and R the inner radius of the hollow fiber.

5.3.1 Nitrites in the liquid phase

The inlet concentration for nitrite in the hollow fiber reactor is specified as:

$$\text{At } z = 0 \text{ and all } r, \qquad C_l = C_{l,in} \tag{5.6}$$

where $C_{l,in}$ is the inlet concentration (mol/m^3). At the center of the reactor, symmetry is assumed in radial direction, resulting in the following boundary condition:

$$\text{At } r = 0 \text{ and all } z, \qquad \frac{\partial C_l}{\partial r} = 0 \tag{5.7}$$

The additional mass transfer resistance offered by the liquid present in the catalyst layer is also considered. The mass transport is mainly governed by diffusion through the liquid-filled pores:

$$D_{l,M}\left(\frac{\partial^2 C_{l,M}}{\partial r^2} + \frac{1}{r}\frac{\partial C_{l,M}}{\partial r}\right) = -R_s \qquad (R < r < R + \delta) \tag{5.8}$$

where $D_{l,M}$ is the diffusion coefficient of nitrite in the catalytic layer (m^2/s), $C_{l,M}$ is the concentration of nitrite in the catalytic layer (mol/m^3), R is the inner channel radius (m), R_s is the reaction rate expression, and δ is the catalytic membrane layer thickness (m). Equation (5.8) is based on the assumption that there is no convection in the porous membrane structure and transport through the catalytic membrane layer is driven by diffusion, quantified by the effective diffusion constant $D_{l,M}$ $(= D_l\epsilon/\tau$, where ϵ is the porosity and τ is the tortuosity of the membrane). Since the chemical reaction term (R_s) is a function of concentration, the partial differential equations are not independent and must be solved simultaneously. Assuming that the nitrite concentration used in the experimental work is low, we have considered the power-law reaction rate expression according to Eq. (5.3) in deriving the boundary conditions. The exponents n and m in Eq. (5.3) depend on the catalyst surface coverage of

Table 5.1: Model parameters and specifications of the porous membrane microreactors

Porous Membrane Microreactor	
Fiber inner radius (mm)	Big fiber- 1.4 Small fiber- 0.4
Wetted membrane thickness [δ] (μm)	Big fiber- 40, 20, 10 Small fiber- 50
Reactor length (m)	0.135
Inlet liquid flow rate (mL/min)	0.1, 0.2, 0.3
Initial nitrite concentration (mol/m^3)	0.2173, 1.0886, 2.1739
diffusion coefficient for nitrite-water (m^2/s)	1.5 x 10^{-9}
diffusion coefficient for hydrogen-water (m^2/s)	4.8 x 10^{-9}
Membrane porosity	0.2
Tortuosity of membrane pore	4
Catalyst area (m^2)	73

nitrite and hydrogen, respectively. The observed reaction rate is limited by the initial reactant concentration and thus, the values for exponents n and m considered to be 1 in deriving the boundary conditions.

$$\text{At } r = R \text{ and all } z, \qquad D_l \frac{\partial C_{l,R}}{\partial r} = D_{l,M} \frac{\partial C_{l,M}}{\partial r} \tag{5.9}$$

where $C_{l,R}$ is the concentration of liquid at position R (mol/m^3). Furthermore;

$$\text{At } r = R \text{ and all } z, \qquad C_{l,M} = C_{l,R} \tag{5.10}$$

$$\text{At } r = R + \delta \text{ and all } z, \qquad \frac{\partial C_{l,M}}{\partial r} = 0 \tag{5.11}$$

Use of Eqs. (5.8)-(5.11) gives the following boundary condition which includes the mass transport and reaction in the wetted catalytic membrane layer.

$$\text{At } r = R \text{ and all } z, \qquad \frac{\partial C_{l,R}}{\partial r} = \frac{2D_{l,M}}{D_l} \left[\frac{C_{l,R} - C_{l,R+\delta}}{k_l C_{g,R} (C_{l,R}^2 - C_{l,R+\delta}^2)} \cdot \frac{1}{R[ln(R+\delta) - lnR]} \right] \tag{5.12}$$

where $C_{g,R}$ is the concentration of gas at position R (mol/m^3).

5.3.2 Hydrogen in the liquid phase

The mass balance for hydrogen in the liquid phase within the microreactor leads to the following boundary conditions.

$$\text{At } z = 0 \text{ and all } r, \qquad C_g = 0 \tag{5.13}$$

where C_g is the concentration of gas (mol/m^3). At the center of the reactor, symmetry is assumed in radial direction, resulting in the following boundary condition,

$$\text{At } r = 0 \text{ and all } z, \qquad \frac{\partial C_g}{\partial r} = 0 \tag{5.14}$$

$$\text{At } r = R + \delta \text{ and all } z, \qquad C_{g,M} = HC_g \tag{5.15}$$

where H is the Henry's coefficient. The mass transport through the liquid phase in the membrane porous structure can be written as;

$$D_{g,M}\left(\frac{\partial^2 C_{g,M}}{\partial r^2} + \frac{1}{r}\frac{\partial C_{g,M}}{\partial r}\right) = -R_s \tag{5.16}$$

where $C_{g,M}$ is the concentration of hydrogen in the catalytic layer (mol/m^3) and $D_{g,M}$ is the diffusion coefficient of hydrogen in the membrane (m^2/s). At the inner surface;

$$\text{At } r = R \text{ and all } z, \qquad D_g\frac{\partial C_{g,R}}{\partial r} = D_{g,M}\frac{\partial C_{g,M}}{\partial r} \tag{5.17}$$

$$\text{And } r = R \text{ and all } z, \qquad C_{g,M} = C_{g,R} \tag{5.18}$$

Using Eqs. (5.15)-(5.18),

$$\text{At } r = R \text{ and all } z, \qquad \frac{\partial C_{g,R}}{\partial r} = \frac{2D_{g,M}}{D_g}\left[\frac{HC_{g,R+\delta} - C_{g,R}}{k_l C_{l,R}(C^2_{g,R+\delta} - C^2_{g,R})} \cdot \frac{1}{R[ln(R+\delta) - lnR]}\right] \tag{5.19}$$

5.3.3 Overall mass transport

The mixing cup concentration ($C_{l,cup}$(mol/m^3)) can be calculated from integration of the nitrite concentration and liquid velocity across the reactor. It can be described by the following expression:

$$C_{l,cup}(z) = \frac{\int C_l(r) \cdot u_z(r) dr}{\int u_z(r) dr} \tag{5.20}$$

The mixing cup concentration corrects for the velocity with which fluids are flowing and provides the concentration at a respective point considering complete mixing.

The rate of mass transfer to reaction boundaries is represented by the local Sherwood number $Sh(z)$. It can be used as an indicator for the efficiency of a reactant adsorbing on a catalytically active surface [21]. It is defined as:

$$Sh(z) = -\frac{N(z)R}{[C_l(z) - C_{l,s}(z)_{|r=R}]D_l} \tag{5.21}$$

where $N(z)$ (mol/m^{2}s) is the local flux to the surface, $C_l(z)$ (mol/m^3)) is the bulk concentration of the liquid reactant calculated according to Eq. (5.20), and $C_{l,s}(z)$ (mol/m^3) is the liquid reactant concentration at the inner surface of the microreactor (at $r = R$).

Equation (5.20) is applied at the microreactor outlet for the validation of numerical results with experimental results, while for the evaluation of the local Sherwood number, the equation is applied at all individual z along the length of the microreactor.

To provide insight into the performance of the microreactor, the cumulative fraction of adsorbed reactant as a function of the axial position is calculated. The fraction is the ratio of the integrated flux towards the reactive boundaries to the integrated inlet flux. It is an important measure from the design perspective as it suggests effectiveness of the reactor configuration. The local Sherwood number in the limit of small z can provide the fraction of adsorbed reactant on reactive boundaries via [32],

$$f = \frac{Sh(z)}{Pe}\frac{z}{R} \tag{5.22}$$

where Pe is the Péclet number ($Pe = UR/D_l$).

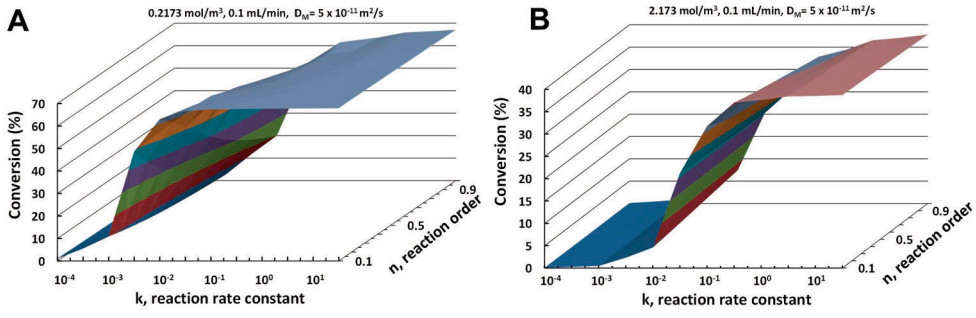

Figure 5.2: Parametric study to evaluate the reaction rate constant and reaction order for power-law rate expression. Flow rate 0.1 mL/min, 40 μm membrane thickness (A) 0.2173 mol/m^3 (B) 2.1739 mol/m^3.

5.3.4 Numerical procedure

The numerical model was solved using COMSOL Multiphysics, which is a finite element modeling tool that facilitates implementation of all governing equations with appropriate boundary conditions. These governing mass balance equations were reduced to their finite element meshes and integrated over the computational domain of interest. The total number of standard triangular mesh elements is 36409 and the mesh density was increased near the catalytic membrane layer. The mesh is refined until the results become independent of mesh size.

5.4 Results and discussion

Numerical simulations of the catalytic nitrite hydrogenation reaction in a porous membrane microreactor were performed. Different process parameters (Table 5.1) such as reactor design parameters (i.e. fiber diameter, catalytic membrane layer thickness, porosity, tortuosity, reactor length) and operational parameters (i.e. reactant concentrations, liquid flow rates) were studied.

5.4.1 Obtaining the reaction rate expression

To validate the proposed model, the nitrite hydrogenation reaction was taken as a model reaction. The operating conditions and reactor geometry used are similar to experimental conditions used by Aran et al. [14, 33]. The values of the reaction

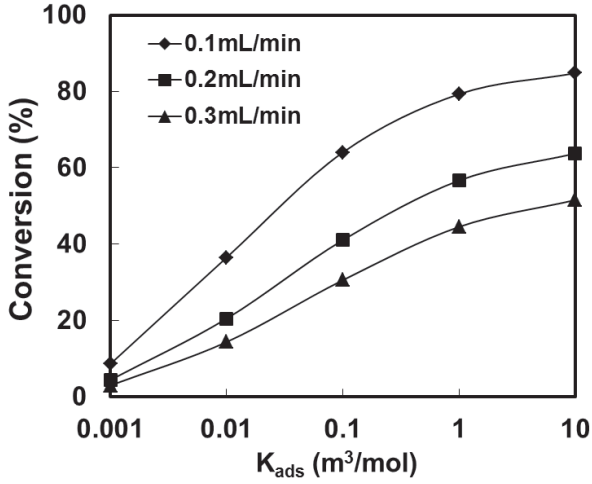

Figure 5.3: Overall conversion for varying adsorption coefficient K_{ads} using the Langmuir-Hinshelwood reaction rate expression. For 40 μm membrane thickness and all inlet nitrite concentrations.

constant and reaction order according to Eq. (5.3) are varied and the resulting overall conversion is shown in Fig. 5.2. It is assumed that the reaction rate is not dependent on hydrogen concentration as was also confirmed by recent experiments [14]. Figure 5.3 shows the conversion obtained considering the LH rate expression according to Eq. (5.2). The results obtained from the reaction rate expression study (power-law and Langmuir-Hinshelwood reaction rate) are shown in Table 5.2 for varying inlet nitrite concentration and liquid flow rates. For the power-law reaction rate expression, the numerical results are in good agreement with the experimental results at lower initial nitrite concentration for all flow rates. However, it is found that the kinetic expression represented in Eq. (5.3) is not in good agreement with experimental results at higher initial nitrite concentration. A possible explanation for this can be a zero-th order reaction at higher nitrite concentration resulting from saturated conditions. This phenomenon is captured by the Langmuir-Hinshelwood expression described in Eq. (5.2).

Table 5.2: Case studied for validation of nitrite hydrogenation reaction rate expression. Comparison of experimental and numerical simulation results for 40 μm catalytic layer thickness. The experimental data are taken from Aran et al.[33]

		Experimental	Modeling (LH rate expression)				Modeling (power-law rate expression)			
Inlet liquid flow rate	Inlet nitrite concentration	Conversion	Outlet nitrite concentration	k_1	K_{ads}	Conversion	Outlet nitrite concentration	n	k_1	Conversion
$[mL/min]$	$[\mathrm{mol}/m^3]$	[%]	$[\mathrm{mol}/m^3]$	$\mathrm{mol/m^3\ s}$	$\mathrm{m^3/mol}$	[%]	$[\mathrm{mol}/m^3]$			[%]
0.1	0.2173	66.6	0.1434	0.00120	0.1120	66.0	0.1415	0.7	0.175	65.1
0.1	1.0869	36.8	0.4130	0.00125	0.1070	38.0	0.4260	0.5	0.230	39.2
0.1	2.1739	25.3	0.5434	0.00116	0.0075	25.0	0.6130	0.3	0.340	28.2
0.2	0.2173	42.8	0.0934	0.00131	0.1150	43.0	0.0986	0.7	0.175	45.4
0.2	1.0869	21.8	0.2282	0.00135	0.1090	21.0	0.2663	0.5	0.230	24.5
0.2	2.1739	14.9	0.3152	0.00131	0.0074	14.5	0.3826	0.3	0.340	17.6
0.3	0.2173	31.0	0.0695	0.00135	0.1170	32.0	0.0754	0.7	0.175	34.7
0.3	1.0869	15.0	0.1630	0.00134	0.1095	15.0	0.2000	0.5	0.230	18.4
0.3	2.1739	10.3	0.2173	0.00135	0.0075	10.0	0.3021	0.3	0.340	13.9

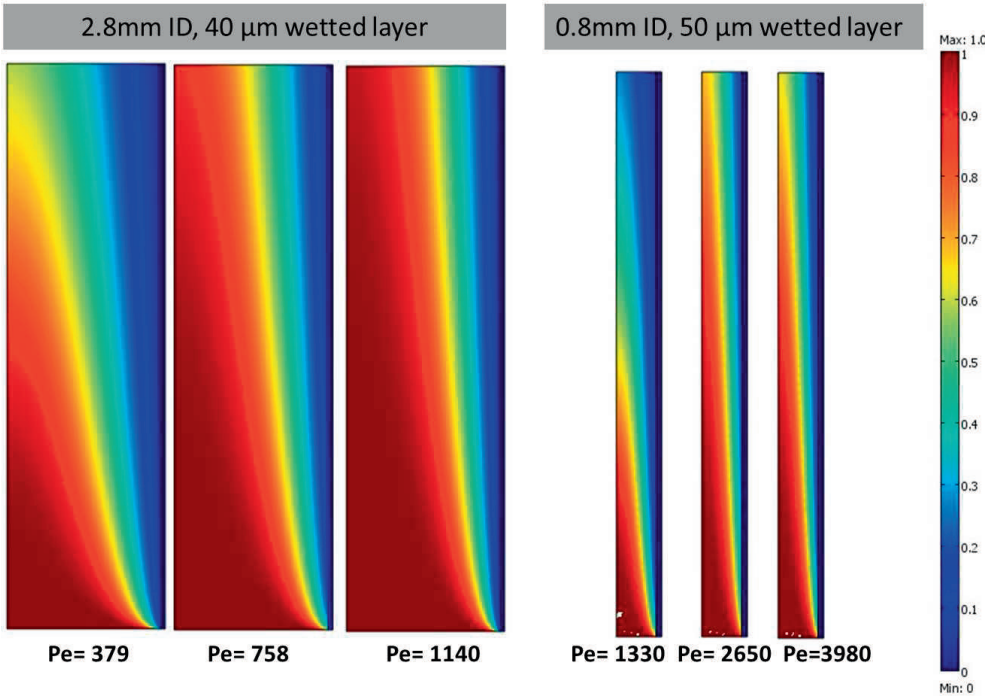

Figure 5.4: Concentration profiles for a larger fiber (2.8 mm ID) and small fiber (0.8 mm ID) for different flow rates.

The parameters k_{LH} and K_{ads} in Eq. (5.2) have been determined by fitting the model to the experimental data obtained from Aran et al. [33]. The value of k_{LH} is found to be 0.0013 mol/m^3·s (95 % of confidence interval within ±0.00005) and K_{ads} to be 0.08 m^3/mol (95 % of confidence interval within ±0.04) for all the process conditions. A good agreement between the experimental results and model predictions based on the Langmuir-Hinshelwood reaction rate expression (Figure 5.3 and Table 5.2) is found.

5.4.2 Nitrite hydrogenation in membrane microreactors

Figure 5.4 shows typical concentration profiles for different Péclet numbers for two microreactor diameters. As can be seen, a boundary layer appears near the wall of the reactor which grows in thickness with increasing distance along the reactor length. This results from the depletion of reactants from the region adjacent to the reaction zone (near the γ-Al_2O_3 layer).

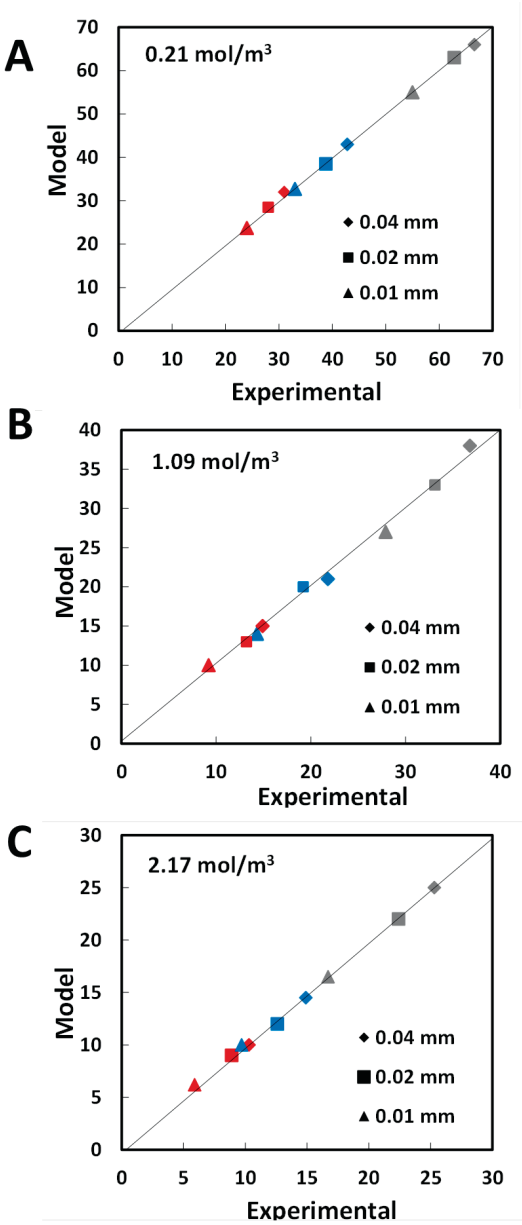

Figure 5.5: Parity plot of the nitrite hydrogenation conversion for three different concentrations for 2.8 mm ID reactor. Study of three catalytic wetting layer thickness (40, 20 and 10 μm) and three different Pe =379 (in red), 758 (in blue) and 1140 (in grey) (A) 0.21 mol/m^3 (B) 1.09 mol/m^3 (C) 2.17 mol/m^3.

The internal diameter of the microreactor, the catalytic membrane layer thickness and the inlet liquid flow rate play a major role in the mass transfer, which strongly affects the overall conversion. The total nitrite removal in different microreactor configurations is calculated at the microreactor outlet by measuring the mixing cup concentration Eq.5.20. In order to validate the values of LH kinetic parameters, parity plots are presented comparing numerical results with experimental observations in Fig. 5.5, for varying inlet nitrite concentration, wetting thickness and Pe numbers. Using the LH reaction rate expression, the numerical results show good agreement with the experimental results for a wide range of conditions.

The liquid reactant concentration profile can be obtained at the inner wall of the microreactor along the axial direction of the microreactor length. Equations (5.3)-(5.19) are coupled and solved simultaneously using a general- partial differential equation solver (in COMSOL). In Fig. 5.6, the concentration profile along the microreactor wall using this approach is plotted together with the concentration profile obtained from two-dimensional CFD model (which solves (5.2) and (5.4)-(5.11) without taking into account the hydrogen transport in the catalytic layer). The results are in good agreement, suggesting the applicability of the model. This explains that with the proposed boundary conditions, represented by Eqs. (5.12) and (5.19), it is possible to obtain an expression representing the concentration of reactants as a function of catalytic membrane layer thickness.

Figure 5.7 shows the influence of the catalytic membrane layer thickness on the reactor performance. The average nitrite concentration at the microreactor wall initially decreases with increasing membrane thickness. This is due to the larger amount of available catalyst surface area. Further increasing the catalytic layer thickness will eventually result in mass transport limitations from the gas side.

Sherwood numbers are plotted against the dimensionless axial position (z/R) according to Eq. (5.21) in Fig. 5.8A ($Pe = 2000$). For very small axial distances, the depletion layer is just starting to form. The depletion layer significantly grows at larger axial positions for the larger reactor configuration compared to the smaller reactor. For the small ID reactors, the boundary layer thickness is relatively small, which improves transport even at large axial positions. These observations also agree qualitatively with previous work [21, 32]. The operating conditions used in previous studies were different, so results cannot be compared quantitatively. However, the simulations of both geometries, (for Pe=2000) confirm the theoretical values of $-1/3$ for the power law scaling of the Sherwood number (assuming a smooth inside microreactor surface)

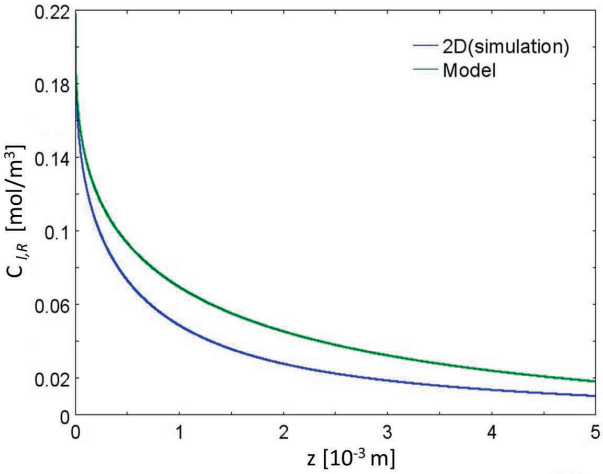

Figure 5.6: Reactant concentration profile at the microreactor wall as a function of the axial position for 40 μm catalytic membrane layer thickness, 0.2173 mol/m^3 initial nitrite concentration and 0.1 mL/min flow rate ($L = 0.135$ m, $D_l = 1 \times 10^{-9}$ m^2/s, $D_g = 4.8 \times 10^{-9}$ m^2/s, $\epsilon = 0.2$, $\tau = 4.0$).

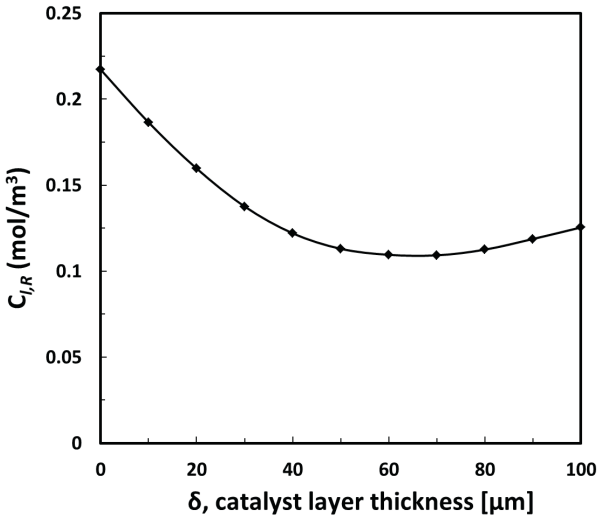

Figure 5.7: Influence of catalytic membrane layer thickness on the average reactant concentration at the microreactor wall for 0.2173 mol/m^3 initial nitrite concentration and 0.1 mL/min flow rate rate ($L = 0.135$ m, $D_l = 1 \times 10^{-9}$ m^2/s, $D_g = 4.8 \times 10^{-9}$ m^2/s, $\epsilon = 0.2$, $\tau = 4.0$).

near the reactor entrance region.

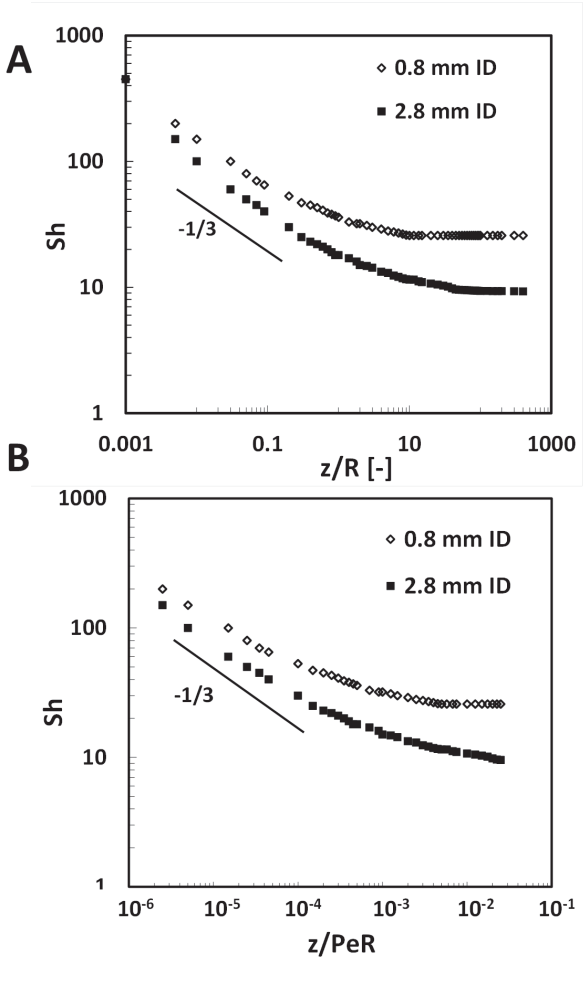

Figure 5.8: (A) Comparison of the local Sherwood number to an adsorbing reaction boundary along the axial position of the microreactor for 2.8 mm and 0.8 mm ID reactor geometry for Pe=2000. (B) Sherwood number as a function of axial distance scaled by Pe.

Furthermore, Fig. 5.8B shows that $Sh(z)$ scales with $(z/PeR)^{-1/3}$. The larger fibers (2.8 mm ID) results in an entrance length of $(z_{ent}/PeR) \sim 1 \times 10^{-2}$. In case of the smaller fiber (0.8 mm ID), the concentration distribution is approaching its asymptotic value at shorter scaled axial distances ($z_{ent}/PeR \sim 3 \times 10^{-3}$), which suggests better performance compared to the bigger fibers. The smaller fiber provides a higher rate of mass transport by sweeping the depleted solute off near the catalytic layer. It leads to thinner boundary layers compared to the bigger fiber (2.8 mm ID).

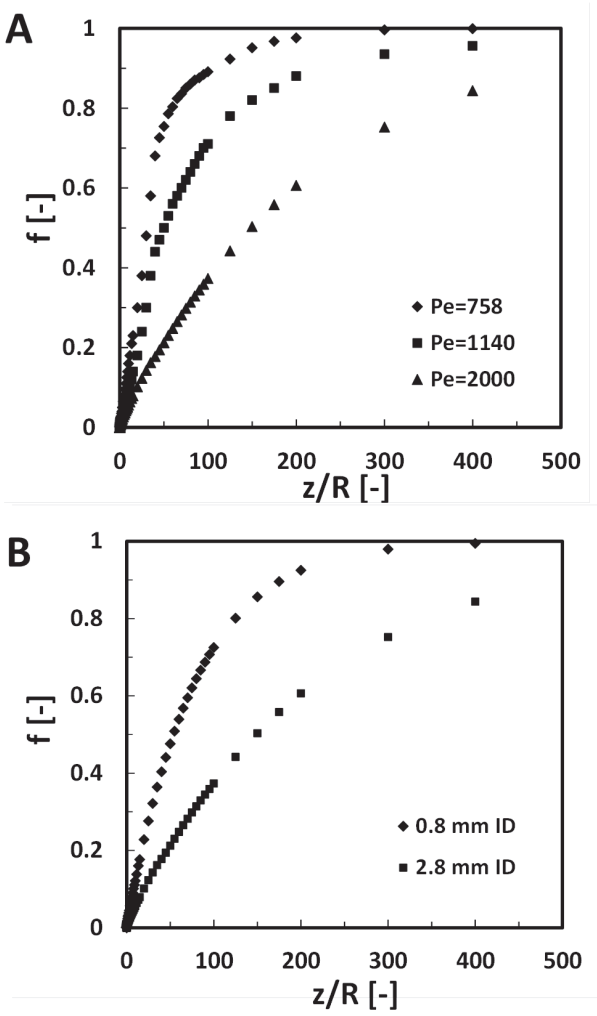

Figure 5.9: A fraction of adsorbed reactant concentration plotted as a function of the axial position. (A) For the big fiber (2.8 mm ID) for Pe 758, 1140 and 2000. (B) For both reactor configurations for Pe=2000

The fraction of adsorbed liquid reactant (nitrite) is calculated (Eq. (5.22)) for different operating conditions and reactor configurations. The fraction f approaches unity for an ideal reactor, where all liquid reactants entering into the reactor are adsorbed and reacted. Figure 5.9A shows f plotted against the axial position for large fibers (2.8 mm ID) and different values of Pe (758, 1140 and 2000). For each Pe, the fraction f increases along the reactor length. It can be observed that a smaller Pe (and hence

a larger residence time) results in a significant increase in this fraction. From these plots, the desired reactor length can be easily extracted.

Figure 5.9B shows a comparison between the two diameters for the case of Pe=2000. For the small diameter reactor, the fraction f increases steeper compared to the large diameter. It reaches unity at around z/R≈300, while the fraction for ID 2.8 mm fiber is approximately 0.7 at that distance. For the same value of Pe number (in the range of 100-400 z/R), the smaller fiber increases this fraction from 70% to 100 % compared to fraction for the larger diameter which increases from 30 % to 80 %. It is apparent from the plot that the smaller diameter reactor is more effective in reducing the depletion layer near the reactive boundary.

5.5 Conclusions

We present a model for a porous membrane microreactor to simulate a wide range of operating conditions and microreactor configurations. The analysis includes a description of the reaction mechanism verified by experimental observations. The proposed model and numerical simulations were validated with experimental data obtained from reactor experiments at varying initial reactant concentrations, inlet flow rates and microreactor geometries. It was found that nitrite hydrogenation in a porous membrane microreactor can be described by the Langmuir-Hinshelwood expression. An accurate description of the boundary condition representing the concentration as a function of catalytic membrane layer thickness has been successfully derived. By comparing several flow rates and reactor diameters, it is concluded that small reactor geometries are important to achieve increased mass transfer to reactive boundaries. The numerical model provides a tool that can be used for the design of such membrane microreactors.

5.6 Acknowledgements

This work was financially supported by Stichting voor de Technische Wetenschappen (STW, Project 07569) in the Netherlands.

5.7 References

[1] V. Hessel, P. Angeli, A. Gavriilidis and H. Löwe; *Gas-liquid and gas-liquid-solid microstructured reactors: contacting principles and applications*; Industrial & Engineering Chemistry Research **44** (25) (2005) 9750–9769

[2] P. Mills, D. Quiram and J. Ryley; *Microreactor technology and process miniaturization for catalytic reactions–A perspective on recent developments and emerging technologies*; Chemical Engineering Science **62** (24) (2007) 6992–7010

[3] J. de Jong, M. Geerken, R. Lammertink and M. Wessling; *Porous Microfluidic Devices–Fabrication and Applications*; Chemical Engineering & Technology **30** (3) (2007) 309–315

[4] G. Centi, R. Dittmeyer, S. Perathoner and M. Reif; *Tubular inorganic catalytic membrane reactors: advantages and performance in multiphase hydrogenation reactions*; Catalysis Today **79** (2003) 139–149

[5] R. Dittmeyer, K. Svajda and M. Reif; *A review of catalytic membrane layers for gas/liquid reactions*; Topics in Catalysis **29** (1) (2004) 3–27

[6] G. Chen, J. Yue and Q. Yuan; *Gas-liquid microreaction technology: Recent developments and future challenges*; Chinese Journal of Chemical Engineering **16** (5) (2008) 663–669

[7] T. Westermann and T. Melin; *Flow-through catalytic membrane reactors–Principles and applications*; Chemical Engineering and Processing: Process Intensification **48** (1) (2009) 17–28

[8] H. Fogler, editor; *Elements of Chemical Reaction Engineering*; 3 edition (1999); New Jersey: Prentice Hall and Englewood Cliffs

[9] M. Vospernik, A. Pintar, G. Bercic, J. Batista and J. Levec; *Potentials of ceramic membranes as catalytic three-phase reactors*; Chemical Engineering Research and Design **82** (5) (2004) 659–666

[10] A. Pintar, G. Berčič and J. Levec; *Catalytic liquid-phase nitrite reduction: Kinetics and catalyst deactivation*; AIChE Journal **44** (10) (1998) 2280–2292

[11] J. Chinthaginjala and L. Lefferts; *Support effect on selectivity of nitrite reduction in water*; Applied Catalysis B: Environmental

[12] O. Ilinitch, F. Cuperus, L. Nosova and E. Gribov; *Catalytic membrane in reduction of aqueous nitrates: operational principles and catalytic performance*; Catalysis Today **56** (1-3) (2000) 137–145

[13] M. Vospernik, A. Pintar, G. Bercic and J. Levec; *Experimental verification*

of ceramic membrane potentials for supporting three-phase catalytic reactions; Journal of Membrane Science **223** (1-2) (2003) 157–169

[14] H. Aran, J. Chinthaginjala, R. Groote, R. Roelofs, L. Lefferts, M. Wessling and R. Lammertink; *Porous ceramic mesoreactors: A new approach for gas-liquid contacting in multiphase microreaction technology*; Chemical Engineering Journal **169** (1-3) (2011) 239 – 246

[15] G. Bercic, A. Pintar and J. Levec; *Positioning of the reaction zone for gas-liquid reactions in catalytic membrane reactor by coupling results of mass transport and chemical reaction study*; Catalysis Today **105** (3-4) (2005) 589–597

[16] R. Wang, H. Zhang, P. Feron and D. Liang; *Influence of membrane wetting on CO2 capture in microporous hollow fiber membrane contactors*; Separation and Purification Technology **46** (1-2) (2005) 33–40

[17] S. Kumar, S. Shankar, P. Shah and S. Kumar; *A comprehensive model for catalytic membrane reactor*; International Journal of Chemical and Reactor Engineering **4** (4) (2006) 1296

[18] E. Nagy; *Mass Transfer through a Convection Flow Catalytic Membrane Layer with Dispersed Nanometer-Sized Catalyst*; Industrial & Engineering Chemistry Research **49** (3) (2009) 1057–1062

[19] K. Li and X. Tan; *Mass transfer and chemical reaction in hollow-fiber membrane reactors*; AIChE Journal **47** (2) (2001) 427–435

[20] T. Gervais and K. Jensen; *Mass transport and surface reactions in microfluidic systems*; Chemical Engineering Science **61** (4) (2006) 1102–1121

[21] J. Kirtland, G. McGraw and A. Stroock; *Mass transfer to reactive boundaries from steady three-dimensional flows in microchannels*; Physics of Fluids **18** (2006) 073602

[22] S. Oyama and P. Hacarlioglu; *The boundary between simple and complex descriptions of membrane reactors: The transition between 1-D and 2-D analysis*; Journal of Membrane Science **337** (1-2) (2009) 188–199

[23] W. Moon and S. Park; *Design guide of a membrane for a membrane reactor in terms of permeability and selectivity*; Journal of Membrane Science **170** (1) (2000) 43–51

[24] W. Jin, X. Gu, S. Li, P. Huang, N. Xu and J. Shi; *Experimental and simulation study on a catalyst packed tubular dense membrane reactor for partial oxidation of methane to syngas*; Chemical Engineering Science **55** (14) (2000) 2617–2625

[25] W. Yu, T. Ohmori, T. Yamamoto, A. Endo, M. Nakaiwa, T. Hayakawa

and N. Itoh; *Simulation of a porous ceramic membrane reactor for hydrogen production*; International Journal of Hydrogen Energy **30** (10) (2005) 1071–1079

[26] C. Fukuhara and A. Igarashi; *Two-dimensional simulation of a membrane reactor for dehydrogenation of ethylbenzene, considering heat and mass transfer*; Journal of Chemical Engineering of Japan **36** (5) (2003) 530–539

[27] T. Brinkmann, S. Perera and W. Thomas; *An experimental and theoretical investigation of a catalytic membrane reactor for the oxidative dehydrogenation of methanol*; Chemical Engineering Science **56** (6) (2001) 2047–2061

[28] K. Hoff, J. Poplsteinova, H. Jakobsen, O. Falk-Pedersen, O. Juliussen and H. Svendsen; *Modeling of membrane reactor*; International Journal of Chemical Reactor Engineering **1** (1) (2002) 1011

[29] M. Reif and R. Dittmeyer; *Porous, catalytically active ceramic membranes for gas-liquid reactions: a comparison between catalytic diffuser and forced through flow concept*; Catalysis Today **82** (1-4) (2003) 3–14

[30] N. Wehbe, N. Guilhaume, K. Fiaty, S. Miachon and J. Dalmon; *Hydrogenation of nitrates in water using mesoporous membranes operated in a flow-through catalytic contactor*; Catalysis Today **156** (3-4) (2010) 208–215

[31] U. Matatov-Meytal; *Radial-flow reactor packed with a catalytic cloth: Nitrate reduction in hydrogen-saturated water*; Industrial & Engineering Chemistry Research **44** (25) (2005) 9575–9580

[32] M. Lopez and M. Graham; *Enhancement of mixing and adsorption in microfluidic devices by shear-induced diffusion and topography-induced secondary flow*; Physics of Fluids **20** (2008) 053304

[33] H. Aran; *Porous ceramic and metallic microreactors: Tuning interfaces for multiphase processes*; Ph.D. thesis (2011)

CHAPTER 6

Modeling of a planar photocatalytic microreactor

A revised version of this chapter has been prepared for publication:

Jigar M. Jani, H.C. Aran, M. Wessling, Rob G.H. Lammertink *Modeling of a planar photocatalytic microreactor*

Abstract

This work describes a computational fluid dynamic (CFD) model and process simulation of a photocatalytic microreactor. The photocatalytic degradation of methylene blue (MB) over TiO_2 catalyst was studied. The model integrates convective and diffusive mass transport, chemical reaction kinetics and ultraviolet (UV) light irradiation distribution within the microreactor. The study is performed to get insight into the reactor performance by verifying experimental observations. The influence of liquid flow rate and photocatalytic film properties on conversion and MB degradation rate were studied. A kinetic model was implemented in the two-dimensional simulations based on the correlations available for reaction kinetics from literature. The analysis showed that the developed CFD model was able to successfully predict the photocatalytic degradation rate of MB according to experimental observations. The light intensity and MB concentration profiles in the photocatalytic film were obtained, which enables to evaluate the effectiveness factor for different configurations of the photocatalytic reactors. The effectiveness factor evaluation of the reactor confirmed that MB degradation is greatly limited by internal mass transfer. This method provides detailed understanding of the reaction, mass transfer and radiation distribution within photocatalytic microreactors.

6.1 Introduction

Heterogeneous photocatalytic applications have gained lots of attention for water treatment and green chemistry[1, 2]. To meet the growing demands of clean drinking water, many new technologies are being developed, realized and evaluated on industrial application grounds. Photocatalysis using immobilized TiO_2 is a very effective sustainable oxidation process for water treatment and waste-water purification [3, 4]. These processes involve photo-excitation of catalysts by light illumination where generated electrons and holes results in the formation of free radicals. These radicals are responsible for the degradation of pollutants [5].

Mainly two types of liquid-phase photocatalytic reactor designs are reported : reactors with a slurry of photocatalytic particles and those with photocatalyst immobilized on the reactor wall [6–8]. The use of suspended catalysts often gives design problems in terms of uniform dispersion in the solution and their separation from the effluent streams [9, 10]. Furthermore, the light intensity is significantly attenuated by the absorption and scattering effects of suspended particles. The disadvantages of suspended systems can be largely avoided by using immobilized photocatalyst on a microreactor wall. In recent studies, it is reported that the photocatalytic efficiencies per unit area of the catalyst of immobilized catalytic films can be similar to that of suspended systems [11]. However, external or internal mass transfer limitations can still be significant for photocatalytic film reactors.

The external mass transfer limitations can be reduced by manipulating flow conditions or by reducing the diffusive distance of reactants. Microreactors are therefore an attractive tool for photocatalytic processes [12–15]. They offer high surface-to-volume ratio and achieve efficient UV illumination on the catalyst surface [2, 12]. The most common immobilized photocatalytic microreactors include the falling film and thin-film annular reactors [1, 16, 17]. Such reactors can be applied for gas-liquid photocatalytic reactions, however, the gas has to diffuse through the liquid film to reach the immobilized catalyst which leads to mass transfer limitations. Recently, porous catalytic membranes were also employed for effective gas-liquid (G-L) reactions [18, 19]. Such reactors provide a suitable configuration for catalyst immobilization. The reactants are separated from each other by a porous membrane that can also serve for catalyst support. Liquid reactants come into direct contact with the gaseous reactants in the catalytic regions of the membrane reactor.

The performance of a photocatalytic process depends on the ability to achieve high efficiency in the utilization of the UV radiation. It is essential to have detailed knowledge of the irradiation intensity profiles in a given reactor geometry to accurately predict and design optimum configurations. The interplay between photocatalyst, reactants and photons requires reliable models to aid the design, scale-up and optimization of photocatalytic reactors [20–24]. These models need radiation transfer coupled with mass and momentum transfer. The application of computational fluid dynamics (CFD) is a very effective tool in the design of photocatalytic reactors. Many of the previous CFD models for immobilized photocatalytic reactors, are related to simulations of reactors for air and water treatment [24, 25]. Duran et al. [24] studied different hydrodynamic models to determine species transport, reaction kinetics and irradiation distribution in immobilized annular photoreactors for water treatment. They confirmed their numerical predictions with experimental observations and found that the degradation of benzoic acid (BA) follows first-order kinetics with respect to BA concentration and UV radiation. They also showed that the BA degradation rate in the photoreactors is mass transfer limited [24]. Salvadó-Estivill et al. [25] performed a CFD study to evaluate the radiation field and reaction kinetics for photocatalytic oxidation of indoor air pollutants (trichloroethylene (TCE)) in a planar photocatalytic reactor. They found that the oxidation rate of TCE follows a Langmuir-Hinshelwood type reaction kinetic. They derived kinetic rate parameters based on experimental and numerical work that are independent of reactor geometry, radiation field and fluid dynamics [25].

There are few studies for planar immobilized photocatalytic reactors [25–28]. The experimental results from Chen et al. [26] indicated that external mass transfer limitations can be reduced by increasing the Reynolds number of the liquid flowing over the immobilized catalyst. The internal mass transfer limitations can be influenced by the nature of the photocatalytic film, the coating method and the thickness of the film. They experimentally determined the process parameters (for BA degradation), such as mass transfer coefficients, adsorption equilibrium constant and effective diffusivity, and verified these with the proposed model [26]. Camera-Roda and Santarelli [27] studied internal mass transfer and UV radiation inside the photocatalytic film and evaluated the effectiveness factor of the film. They considered two different cases for the light illumination, one with the film being exposed to light from the solution side and other with the light coming from the support side. The rate of degradation increases until a critical catalyst film thickness after which severe depletion of photons takes place.

This leads to a reduced reaction rate and little degradation. [27]. Edwards et al. [28] studied the effectiveness factors for catalysts immobilized in porous membranes for planar photocatalytic reactors. They considered different reaction rate expression (zero-, first- and second-order and Langmuir-Hinshelwood kinetics) in their analysis to evaluate the effectiveness factor. They found that when illumination is introduced from the solution side to the photocatalytic film, the effectiveness factor follows conventional heterogeneous catalysis. They also showed that the configuration with illumination coming from the support side of the film is less favorable considering effectiveness of the photocatalytic film [28].

The rigorous modeling of the radiation and solute concentration distribution in the photocatalytic film is particularly important for characterization of the photoreactor [27, 28]. These studies have been successful in providing a description of the effect of optical film thickness on the photocatalytic process. However, a CFD model which can predict solute degradation as a function of the Reynolds number for different reactor configurations and its influence on transport within the photocatalytic film have received little attention, especially at the microscale. The primary objective of this work is to develop a CFD-based model for methylene blue degradation (MB) in the planar immobilized photocatalytic reactor and verifying its numerical predictions with experimental observations. The photocatalytic reaction kinetics was coupled with convection-diffusion to obtain steady-state behavior of the reactor. The study aims to obtain concentration and radiation distributions in the liquid microchannel and photocatalytic film by incorporating species mass transport and UV radiation. The effectiveness factor of the photocatalytic film is evaluated to quantify the performance of the reactor for varying optical thickness of the film. The photocatalytic microreactor model involves identical operating conditions and geometry that were used in experiments previously [29].

6.2 CFD modeling

As shown in the scheme in Fig.6.1, the photocatalytic reaction takes place on a thin planar film of immobilized photocatalysts (TiO_2). The microreactor is 500 μm in height and 65 mm in length. The photocatalytic reactor is assumed to have:

- isothermal, incompressible and laminar flow conditions under steady state.
- uniform surface illumination of the photocatalysts entering from the top of the

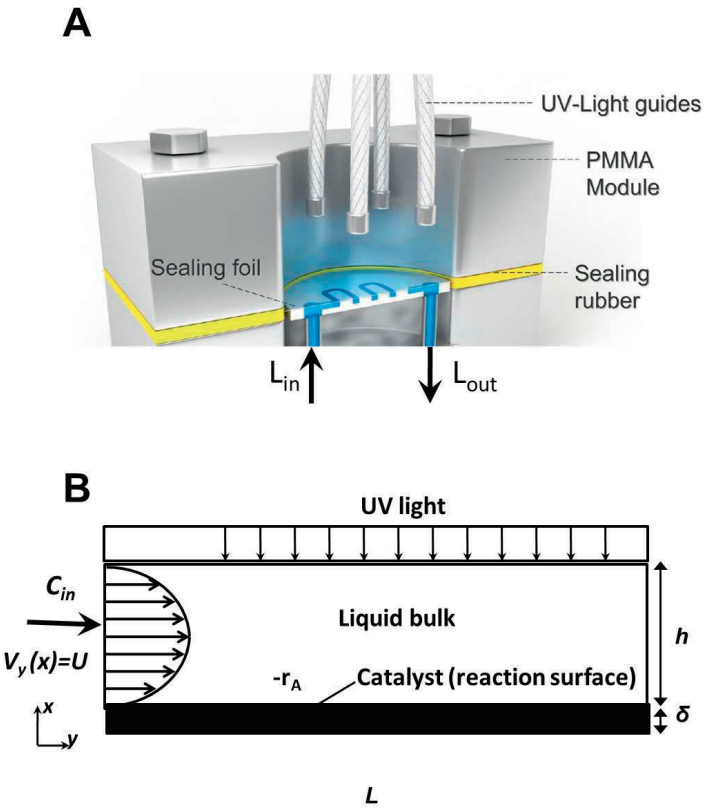

Figure 6.1: (A) Schematic representation of the porous photocatalytic membrane microreactor module (B) computational representation of the liquid channel in the photocatalytic microreactor

microchannel.

- uniform distribution of the photocatalysts over the substrate.

The laminar velocity profile perpendicular to the microchannel cross-section is represented by,

$$v_y = U\left[1 - \left(\frac{2x-h}{h}\right)^2\right] \tag{6.1}$$

where v_y is the axial liquid velocity (m/s), U is the maximum velocity (m/s), x is the distance from the catalytically active surface (m), and h is the height of the microchannel (m). The mass balance for reactant A in the liquid channel can be

written as:

$$v_y \frac{dC_A}{dy} = D \frac{d^2 C_A}{dx^2} \tag{6.2}$$

here C_A and D are concentration (mol/m^3) and diffusion coefficient (m^2/s) of A in water, respectively. The boundary condition for the channel inlet is as follows:

$$\text{At } y = 0 \text{ and all } x, \qquad C_A = C_{A,in} \tag{6.3}$$

where $C_{A,in}$ is the inlet concentration (mol/m^3). At the top of the microreactor, insulation (no-flux boundary) is assumed, resulting in the following boundary condition,

$$\text{At } x = h \text{ and all } y, \qquad \frac{dC_A}{dx}_{x=h} = 0 \tag{6.4}$$

The steady state mass transport equation for the photocatalytic layer ($0< x < \delta$) can be written as:

$$D_{A,M} \frac{d^2 C_A}{dx^2} = -r_A \tag{6.5}$$

where r_A is the rate of photocatalytic reaction of A (mol/m$^3 \cdot s$) and $D_{A,M}$ ($= D\epsilon/\tau$) is the effective diffusion coefficient of A in the photocatalytic layer (m^2/s). Here ϵ is the porosity and τ is the tortuosity of the photocatalytic film. For the adsorption and reaction in the catalyst layer ($0< x < \delta$) (at the liquid-catalyst and catalyst-substrate boundaries, respectively), the boundary conditions can be written as:

$$\text{At } x = 0, \qquad \frac{dC_A}{dx}_{x=0} = 0 \tag{6.6}$$

$$\text{At } x = \delta, \qquad C_A = C_{AS} \tag{6.7}$$

where C_{AS} is the concentration at the fluid-catalyst interface. The right hand term in Eq. 6.5 is provided by a reaction mechanism for the photocatalytic oxidation of MB. The direct oxidation reaction for the complete degradation of MB is given by [30, 31]:

$$C_6H_{18}N_3SCl + 25.5O_2 \overset{h\nu \geq 3.2eV, TiO_2}{\rightarrow} HCl + H_2SO_4 + 3HNO_3 + 16CO_2 + 6H_2O \tag{6.8}$$

The rate expression depends on the local surface rate of photon absorption (LSRPA) [25]. The MB concentration used in the experimental work is very low (70 μM) so UV absorption by dissolved MB can be neglected. We have considered a simple power-law reaction rate expression including radiation intensity defined as:

$$-r_A = kI_e^m C_A \tag{6.9}$$

where I_e is the local volumetric rate of radiant energy absorption (LVREA) [32, 33] and k is the apparent reaction rate constant. For parallel UV radiation pathways, the LVREA is described as $I_e = \mu I$ [26, 28, 34], where I is the average UV irradiation at the catalyst surface and μ is the absorption coefficient per unit thickness of the film. The exponent m in Eq. 6.9 depends on the efficiency of electron-hole formation. For mild UV radiation, the observed reaction rate is limited by the radiation intensity and the observed reaction rate becomes first-order for the light intensity.

The rate expression in Eq. 6.9 considers the radiation in the operating wavelength range by the catalyst film. The radiation flux (I) varies with depth according to the relation:

$$I = I_0 exp[-\mu x] \tag{6.10}$$

where I_0 is the uniform flux of irradiation that enters through the top of the microchannel. The value of the absorption coefficient, μ, depends on the chemical nature of the catalyst and structural properties of the photocatalytic film [21]. If the optical thickness θ of the photocatalytic film is defined as $\theta = \mu \cdot \delta$, where δ is the geometrical thickness of the film, Eq. 6.10 becomes:

$$I = I_0 exp[-\theta x/\delta] \tag{6.11}$$

Based on the above assumptions, the mass transfer equation in the photocatalytic film can be written as:

$$D_{A,M} \frac{\partial^2 C_A}{\partial x^2} = -r_A = kC_A I\mu \tag{6.12}$$

The dimensionless form of Eq. 6.12 can be written as:

$$\frac{\partial^2 c^*}{\partial x^{*2}} = \phi^2 c^* I^* \tag{6.13}$$

with $c^* = C_A/C_{AS}$, $x^* = x/\delta$, $I^* = I/I_0$ as dimensionless quantities and ϕ is defined as the Thiele modulus:

$$\phi^2 = \frac{\delta^2 k \mu I_0}{D_{A,M}} \tag{6.14}$$

Here the new boundary conditions are: at x^*=0, $dc^*/dx^* = 0$ and at x^*=1, c^*=1. The effectiveness factor is calculated by the control volume method [35] with the expression defined as:

$$\eta = \frac{\text{actual reaction rate}}{\text{reaction without mass and photon transfer limitations}} = \frac{1/\delta \int_0^\delta r_A}{k C_{AS} I_0 \mu} \tag{6.15}$$

The reaction rate expressed in the denominator of Eq. 6.15 represents the reaction rate which will be observed in an ideal case with uniform distribution of MB concentration and radiation intensity inside the film. The effectiveness factor allows to characterize the performance of the photocatalytic microreactor.

Table 6.1: Parameters and specifications of the photocatalytic microreactor

Photocatalytic microreactor	
Microchannel height (mm)	0.5
Reactor length (mm)	65
Inlet liquid flow rate (μL/min)	10, 30, 50
Initial MB concentration (μM)	70
Diffusion coefficient for MB-water (m^2/s)	1.5 x 10^{-9}

The numerical model for the photocatalytic microreactor was solved using finite element modeling (Comsol). The governing equations were converted to their finite element meshes and solved for the entire computational domain. The domain of the microreactor is divided into a triangular meshes. The total numbers of standard mesh elements are 41385 and the mesh density increases near the photocatalytic layer. The meshes were verified until the results become independent of mesh size. A uniform parabolic flow profile is implemented for the liquid flowing through the microchannel inlet. The simulation conditions for microreactor and operations are mentioned in Table 6.1. The average outlet concentration can be calculated as follows:

$$C_{A,out}(y) = \frac{\int C_A \cdot v_y dA}{\int v_y dA} \tag{6.16}$$

where A (m^2) is the cross-sectional area, and the integrals taken over the microchannel cross-section.

6.3 Results and discussion

The MB degradation in the photocatalytic microreactor was modeled and verified with experimental observations described in literature [29].

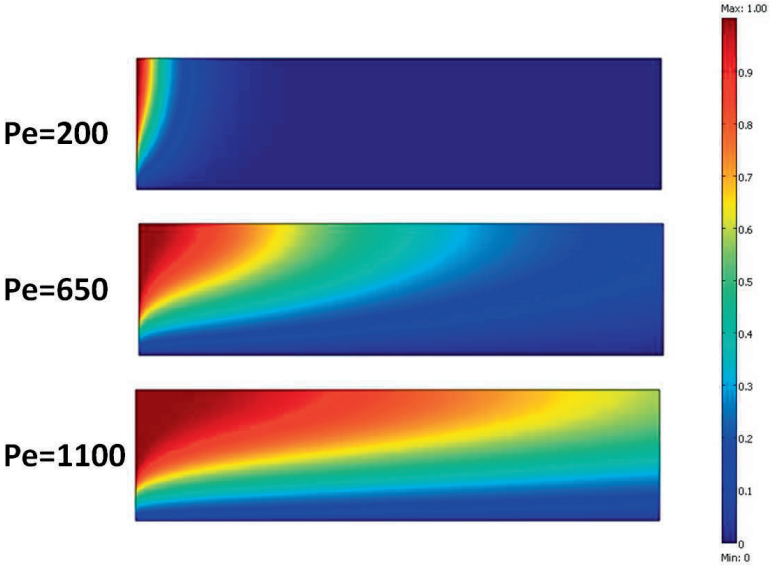

Figure 6.2: Concentration profile for three different Pe= 200, 650 and 1100 and 1000 W/m^2 UV irradiation.

Figure 6.2 shows the concentration profiles of MB in the presence of UV irradiation (1000 W m^{-2}) for three different Péclet numbers (Pe) of 200, 650 and 1100. A concentration boundary layer appears near the inlet of the reactor and grows in the perpendicular direction to the flow along the length of the microreactor. The developing profiles are the result of convection, diffusion and (photocatalytic) reaction in the microreactor. The concentration boundary layer thickness is an inverse function of velocity. From these profiles, the overall conversion can be determined.

Figure 6.3 depicts the overall conversion of MB for Re in the range of 0.25-250. The numerical results are compared with the experimental observations and they are in good agreement with each other. The results in Fig. 6.3 show that MB conversion decreases with increasing Re which is due lower residence time in the reactor. The comparison of numerical predictions and experimental results, as in Fig. 6.3, allow to extract the reaction rate constant (k). From the plot, the value of k is found to be 0.2

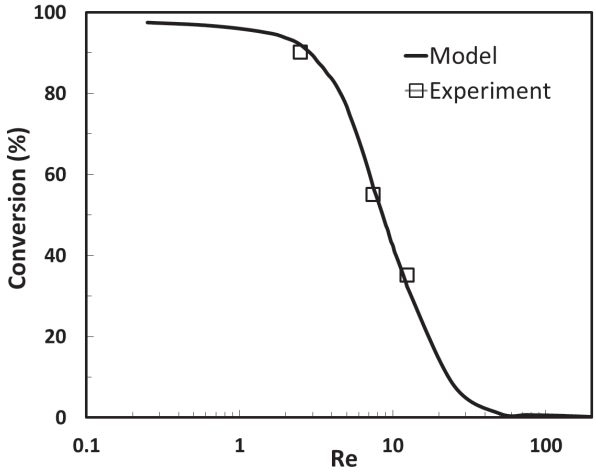

Figure 6.3: Conversion as a function of Reynolds number for 70 μM initial MB concentration and 1000 W/m^2 UV irradiation.

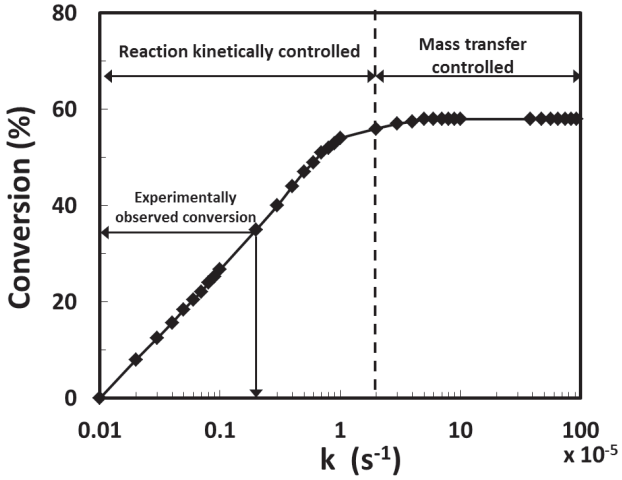

Figure 6.4: Result of conversion plotted against the reaction rate constant for 70 μM concentration, *Re* 12.5 and radiation intensity 1000 W/m^2.

$\times$ 10^{-5} s^{-1}.

It is known that mass transfer limitations often affect immobilized photoreactors. We attempted to identify the regime where the operation of microreactors is reaction limited. The reaction rate constant was varied ranging from 0.01 $\times$ 10^{-5} s^{-1} to 100

$\times 10^{-5}$ s^{-1}. Figure 6.4 shows that the conversion increases up to a k value of 2.0 $\times$ 10^{-5} s^{-1} and then achieves a constant value, suggesting that the reaction is transport limited beyond that point. A k value of 0.2 $\times$ 10^{-5} s^{-1} suggests that the reaction is kinetically controlled and mass transfer is efficient.

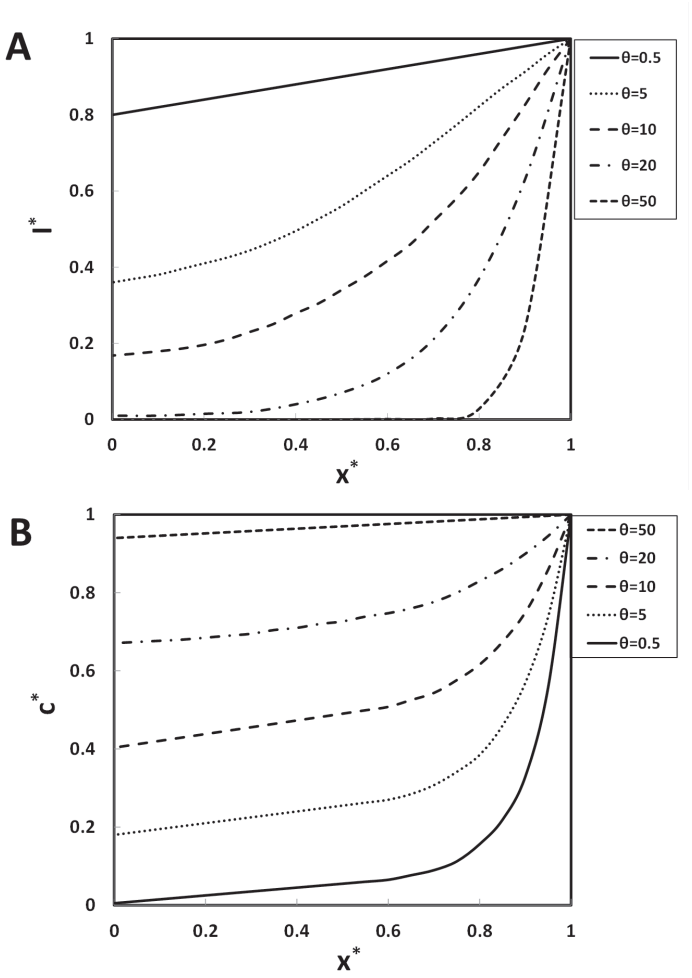

Figure 6.5: UV intensity and MB concentration profile for different optical thickness in the photocatalytic film for I_0=1000 W/m^2 (A) Irradiation intensity profile (B) MB concentration profile.

Figure 6.5A shows the dimensionless UV irradiation profile plotted for various values of optical thickness (θ=0.5-50) of the catalyst layer. Due to absorption of the UV light in the catalyst film, the corresponding intensity profiles are established. The UV

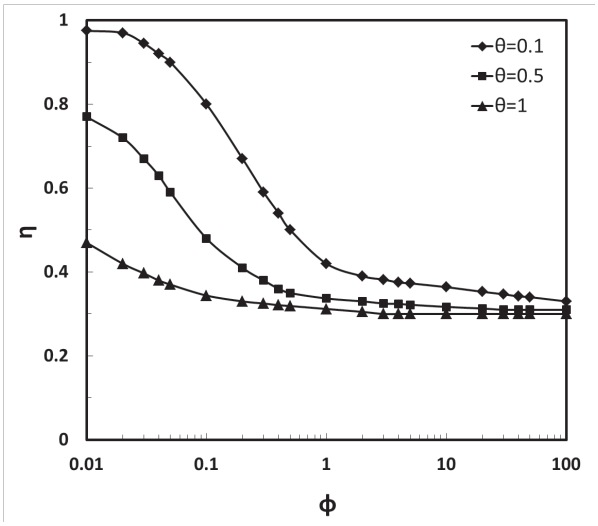

Figure 6.6: Effectiveness factor (η) plotted against Thiele modulus (ϕ) for a range of optical thicknesses (I_0=1000 W/m^2).

light reaches in the photocatalytic layer within the limits of penetration depth. For small optical thickness, the UV light is homogeneously distributed over photocatalysts. As optical thickness increases, the photocatalysts receives little exposure in deeper regions. This influences the final conversion and photocatalytic reactor efficiency. The optical film thickness strongly affects the UV intensity distribution which will influence the rate of the reaction consequently.

The steady-state numerical solution provides the concentration profile along the thickness of the photocatalytic film ($0< x < \delta$). Figure 6.5 B illustrates the concentration profile of MB *vs.* the dimensionless thickness of the photocatalytic film in the presence of UV irradiation (1000 W m^{-2}) for various values of optical thickness (θ=0.5-50). For small optical thickness ($\theta \leq$ 0.1-0.5), the light intensity distribution is almost uniform in the photocatalytic layer. The UV light can, in this case, access most photocatalysts in the film and complete degradation of MB is observed. The light intensity profile becomes steeper with increasing in the optical thickness as most of the UV light is being absorbed by the catalysts near film. This results in little light intensity exposing the remaining photocatalyst layer and therefore leads to a lower reaction rate. Consequently, the MB concentration remains relatively high in the photocatalytic film (flat concentration profile) and the MB degradation is compromised.

The effectiveness factor calculated for the photocatalytic microreactor (according to

eq. 6.15) is presented in Fig.6.6. It is qualitatively analogous to the effectiveness factor for conventional heterogeneous catalytic reactors [36, 37]. From Fig. 6.6, it is clear that the effectiveness factor decreases with increasing of Thiele modulus for all optical thickness. This is caused by diffusion and UV intensity limitations arising at high values of ϕ. As the photocatalytic film thickness increases the non-uniform distribution of UV light becomes more critical, which negatively affects the efficiency of the photocatalytic film.

For the first-order reaction rate mechanism (Eq. 6.9), the effectiveness factor eventually achieves an asymptotic value after a certain value of Thiele modulus. This plot qualitatively matches with the observations by Edwards *et al.* [28] for first order reaction kinetics. Confirming their observations, the maximum value of effectiveness factor, for $\phi \to 0$ and $\theta \to 0$, approaches to unity. Similarly, the effectiveness factor achieves a constant value at high Thiele modulus. This is due to reduced reaction rate caused by diffusion and UV light distribution limitations in the interior of the photocatalytic film. This leads to low values of the effectiveness factor which becomes relatively insensitive for the changes in the Thiele modulus. The plot of η versus ϕ for the photocatalytic reactor are in agreement with these general observations by Edwards et al. [28].

6.4 Conclusions

A CFD model for a planar photocatalytic microreactor was developed and validated to show good agreement with the experimental observations. The influence of the radiation intensity in the photocatalytic layer has been included by incorporating the absorption of UV radiation by means of optical thickness. The study showed that the degradation of MB is dependent on the optical thickness of the photocatalytic layer. The influence of UV light distribution on the performance of photocatalytic microreactor was analyzed using effectiveness factor. It showed that the reactor performance is strongly influenced by the extent to which UV radiation is distributed in the photocatalytic film. The model allows to consider the geometrical configurations of the reactor and the distribution of the radiation intensity across the photocatalysts. The coupled model covers a rigorous description of the photocatalytic microreactor, which is required to design photocatalytic microreactors for various applications.

6.5 Acknowledgments

This work was financially supported by Stichting voor de Technische Wetenschappen (STW, Project 07569) in the Netherlands. We also greatly acknowledge J.Bennink (Tingle.nl) for the illustrations.

6.6 References

[1] O. Alfano, D. Bahnemann, A. Cassano, R. Dillert and R. Goslich; *Photocatalysis in water environments using artificial and solar light*; Catalysis Today **58** (2-3) (2000) 199–230

[2] T. Van Gerven, G. Mul, J. Moulijn and A. Stankiewicz; *A review of intensification of photocatalytic processes*; Chemical Engineering and Processing **46** (9) (2007) 781–789

[3] A. Adesina; *Industrial exploitation of photocatalysis: progress, perspectives and prospects*; Catalysis Surveys from Asia **8** (4) (2004) 265–273

[4] J. Herrmann; *Heterogeneous photocatalysis: state of the art and present applications*; Topics in Catalysis **34** (1-4) (2005) 49–65

[5] C. Turchi and D. Ollis; *Photocatalytic degradation of organic water contaminants: mechanisms involving hydroxyl radical attack*; Journal of Catalysis **122** (1) (1990) 178–192

[6] H. De Lasa, B. Serrano and M. Salaices; *Photocatalytic reaction engineering* (2005); Springer Verlag

[7] R. Matthews; *Photocatalytic oxidation of organic contaminants in water: an aid to environmental preservation*; Pure Applied Chemistry **64** (9) (1992) 1285

[8] M. Bideau, B. Claudel, C. Dubien, L. Faure and H. Kazouan; *On the immobilization of titanium dioxide in the photocatalytic oxidation of spent waters*; Journal of Photochemistry & Photobiology, A: Chemistry **91** (2) (1995) 137–144

[9] K. Sopajaree, S. Qasim, S. Basak and K. Rajeshwar; *An integrated flow reactor-membrane filtration system for heterogeneous photocatalysis. Part I: Experiments and modelling of a batch-recirculated photoreactor*; Journal of Applied Electrochemistry **29** (5) (1999) 533–539

[10] S. Kagaya, K. Shimizu, R. Arai and K. Hasegawa; *Separation of tita-*

nium dioxide photocatalyst in its aqueous suspensions by coagulation with basic aluminium chloride; Water Research **33** (7) (1999) 1753–1755

[11] M. Dijkstra, A. Michorius, H. Buwalda, H. Panneman, J. Winkelman and A. Beenackers; *Comparison of the efficiency of immobilized and suspended systems in photocatalytic degradation*; Catalysis Today **66** (2-4) (2001) 487–494

[12] E. Coyle; *Micro-photochemistry: photochemistry in microstructured reactors. The new photochemistry of the future?*; Photochemical & Photobiological Sciences **7** (11) (2008) 1313–1322

[13] R. Gorges, S. Meyer and G. Kreisel; *Photocatalysis in microreactors*; Journal of Photochemistry and Photobiology A: Chemistry **167** (2-3) (2004) 95–99

[14] Y. Matsushita, N. Ohba, S. Kumada, K. Sakeda, T. Suzuki and T. Ichimura; *Photocatalytic reactions in microreactors*; Chemical Engineering Journal **135** (2008) S303–S308

[15] K. Jähnisch, V. Hessel, H. Löwe and M. Baerns; *Chemistry in microstructured reactors*; Angewandte Chemie International Edition **43** (4) (2004) 406–446

[16] G. Puma, J. Khor and A. Brucato; *Modeling of an annular photocatalytic reactor for water purification: oxidation of pesticides*; Environmental Science & Technology **38** (13) (2004) 3737–3745

[17] K. Jähnisch and U. Dingerdissen; *Photochemical Generation and [4+ 2]-Cycloaddition of Singlet Oxygen in a Falling-Film Micro Reactor*; Chemical Engineering & Technology **28** (4) (2005) 426–427

[18] H. Aran, J. Chinthaginjala, R. Groote, R. Roelofs, L. Lefferts, M. Wessling and R. Lammertink; *Porous ceramic mesoreactors: A new approach for gas-liquid contacting in multiphase microreaction technology*; Chemical Engineering Journal **169** (1-3) (2011) 239 – 246

[19] G. Bercic, A. Pintar and J. Levec; *Positioning of the reaction zone for gas-liquid reactions in catalytic membrane reactor by coupling results of mass transport and chemical reaction study*; Catalysis Today **105** (3-4) (2005) 589–597

[20] M. Roger and J. Villermaux; *Modelling of light absorption in photoreactors Part I. General formulation based on the laws of photometry*; The Chemical Engineering Journal **17** (2) (1979) 219–226

[21] M. Cabrera, O. Alfano and A. Cassano; *Absorption and scattering coefficients of titanium dioxide particulate suspensions in water*; The Journal of Physical Chemistry **100** (51) (1996) 20043–20050

[22] Z. Zhang, W. Anderson and M. Moo-Young; *Rigorous modeling of UV*

absorption by TiO2 films in a photocatalytic reactor; AIChE Journal **46** (7) (2000) 1461–1470

[23] J. Kuipers and W. Van Swaaij; *Computational fluid dynamics applied to chemical reaction engineering*; Advances in Chemical Engineering **24** (1998) 227–328

[24] J. Duran, M. Mohseni and F. Taghipour; *Modeling of annular reactors with surface reaction using computational fluid dynamics (CFD)*; Chemical Engineering Science **65** (3) (2010) 1201–1211

[25] I. Salvadó-Estivill, D. Hargreaves and G. Puma; *Evaluation of the intrinsic photocatalytic oxidation kinetics of indoor air pollutants*; Environmental Science & Technology **41** (6) (2007) 2028–2035

[26] D. Chen, F. Li and A. Ray; *Effect of mass transfer and catalyst layer thickness on photocatalytic reaction*; AIChE journal **46** (5) (2000) 1034–1045

[27] G. Camera-Roda and F. Santarelli; *Optimization of the thickness of a photocatalytic film on the basis of the effectiveness factor*; Catalysis Today **129** (1-2) (2007) 161–168

[28] M. Edwards, C. Villa, C. Hill Jr and T. Chapman; *Effectiveness factors for photocatalytic reactions occurring in planar membranes*; Industrial & Engineering Chemistry Research **35** (3) (1996) 712–720

[29] H. Aran; *Porous ceramic and metallic microreactors: Tuning interfaces for multiphase processes*; Ph.D. thesis (2011)

[30] S. Lakshmi, R. Renganathan and S. Fujita; *Study on TiO2-mediated photocatalytic degradation of methylene blue*; Journal of Photochemistry and Photobiology A: Chemistry **88** (2-3) (1995) 163–167

[31] A. Houas, H. Lachheb, M. Ksibi, E. Elaloui, C. Guillard and J. Hermann; *Photocatalytic degradation pathway of methylene blue in water*; Applied Catalysis B: Environmental **31** (2) (2001) 145–157

[32] A. Cassano, C. Martin, R. Brandi and O. Alfano; *Photoreactor analysis and design: fundamentals and applications*; Industrial & Engineering Chemistry Research **34** (7) (1995) 2155–2201

[33] A. Cassano and O. Alfano; *Reaction engineering of suspended solid heterogeneous photocatalytic reactors*; Catalysis Today **58** (2-3) (2000) 167–197

[34] G. Imoberdorf, A. Cassano, O. Alfano and H. Irazoqui; *Modeling of a multiannular photocatalytic reactor for perchloroethylene degradation in air*; AIChE Journal **52** (5) (2006) 1814–1823

[35] C. Hill; *An introduction to chemical engineering kinetics & reactor design* (1977);

Wiley New York

[36] J. Carberry; *Chemical and catalytic reaction engineering* (2001); Dover Publications

[37] H. Fogler; *Elements of chemical reaction engineering* (1998); Prentice Hall International

CHAPTER 7

Conclusions and outlook

In this chapter the conclusions of the work described are summarized followed by an outlook. This outlook mentions the current scenario of microreaction technology and demonstrates its capabilities for wider socio-economic benefits.

7.1 Conclusions

This study focused on the design and optimization of contacting devices that use membrane functionality for multiphase contacting at the microscale. Chapter 2-4 focus on physical gas-liquid contacting and chapter 5 and 6 address multiphase heterogeneously catalyzed reactions.

The concept of porous helical membrane devices presented in **Chapter 2** has been used to generate mixing at a microscale. Numerical and experimental studies demonstrated that helical structures perform more effectively compared to straight microchannel. This has been analyzed using both numerical and experimental methods. The helical design was exploited to produce secondary flows in microchannels, which enhance mixing. This work showed that the gas uptake in liquid flowing inside helical membrane channels was 80 % higher compared to straight microchannels for Re>60. The optimization study revealed that the flux enhancement is not only dependent on Re but also depends strongly on the geometrical configuration of the microchannel. To maximize the mixing index, three critical parameters were identified i.e., the curvature diameter, helical pitch and internal channel diameter. The design parameter sensitivity analysis showed that mixing can be greatly influenced by the curvature diameter and helical pitch. Increase in internal diameter of the microchannel increases mixing because of a pronounced Dean effect due to centrifugal force.

In **chapter 3**, a detailed numerical model and optimization study was performed to study transport effects for microgrooved membranes. The liquid flow field is greatly influenced by these microgrooves. Two types of microgrooves have been studied in relation to mass transport: continuous and non-continuous microgrooves. The use of continuous and alternating microgrooves gave enhanced mass transport. A detailed geometrical optimization study using the Taguchi method [1] was conducted to elucidate the enhancement in flux for microgrooved membranes compared to flat membranes. This research indicates that structured hydrophobic porous membranes can be successfully employed to increase mass transfer and reduce concentration polarization along the gas-liquid interface.

Chapter 4 describes experimental work related to the numerical study described in Chapter 3. A microgrooved membrane for gas-liquid contacting was fabricated using liquid induced phase-separation. An experimental study using grooved membranes suggest enhancement in flux up to 30 %. The flux enhancement is observed due to a partial shear-free gas-liquid interface. The performance of the membrane devices decreased with wetted microgrooves due to mass transport limitations. The flow visualization experiments reveal wetting of the microgrooves at higher liquid flow rates. According to both the numerical simulations and experimental observations of the gas-liquid contacting, we have shown that it is possible to increase the gas uptake in liquid by merely structuring the membrane surface.

Chapter 5 presents a detailed modeling approach for a porous membrane microreactor that covers a wide range of operating conditions and microreactor configurations. The proposed model and numerical simulations were validated with experimental data [2]. The boundary condition representing the reactor wall concentration as a function of catalytic membrane layer thickness has been obtained and an optimum in conversion and catalytic layer thickness was found. By comparing several flow rates and reactor diameters, it is concluded that a small channel diameter is important to achieve increased mass transfer to reactive boundaries. The performance of the microreactor drops at higher catalytic layer thickness due to gaseous reactant mass transfer limitation. The numerical model provides useful insight into the understanding of mass transport and catalytic reactions in membrane microreactors.

Chapter 6 describes a numerical model for photocatalytic degradation of methylene blue (MB) in a planar photocatalytic microreactor, which was validated with experimental observations. Influence of the radiation intensity in the photocatalytic layer has been included via the optical thickness. The study showed that the degradation of MB is dependent on the optical thickness of the photocatalytic layer. The effectiveness factor of the photocatalytic film is considered to study the performance of the microreactor. It was shown that the effectiveness factor is strongly influenced by the distribution of UV radiation in the photocatalytic film. The model optimizes geometrical parameters of the photoreactor and analyzes distribution of the radiation intensity across the photocatalytic film.

By simple design, enhanced mass transfer can be achieved in microscale channel geometries that can be constructed easily and used flexibly. CFD modeling help to understand the physical/chemical processes at the microscale and can be used to optimize the membrane reactors/contactors. A detailed modeling approach supported

with experiments help to identify the limitations and optimize the given system.

7.2 Outlook

Membrane based gas-liquid contacting has achieved significant interest for diverse applications. There are mainly two pathways to follow: (1) With the existing knowledge and technical abilities, apply innovations to new applications and carry forward the manufacturing/processing at various scales, finding new routes for conventional processes, interfacing with new developments etc. (2) Development of innovative membranes functionality and contacting principles with the help of different materials, fabrication methods and module development. Both of these approaches are fascinating and provide a comprehensive outlook towards the future.

7.2.1 Porous membranes and their applications

The research work in membrane development till date was mainly focusing on material choice. It will be in accordance with the process requirements and its robustness towards chemical, mechanical and thermal conditions. These conditions led to reinvent the fundamental principles of membrane fabrication. One of the research work that we performed was the fabrication of microgrooved membranes for gas-liquid contacting. They were prepared by using phase-separation micromolding [3] described in Chapter 4. It will be interesting to study the influence of polymer solution and coagulation bath composition in fabricating membranes with diverse surface properties. The development of the membrane based contacting has strongly emphasized membrane fabrication, tuning the membrane morphology. Porous membrane development requires thorough analysis of the physical properties, such as pore size distribution, pore structure, wetting behavior and reproducibility, of the prepared membranes and its performance in gas-liquid contacting. This helps to identify the problems concerning the efficiency of the devices. Chapter 2-4 provides a ground for further research into fundamental membrane properties for the improvement in gas-liquid contacting. The influence of different membrane configurations on the performance of device can also be studied further.

All flux enhancement experiments performed on microgrooved membranes in this thesis were performed with a thickness of 100-600 μm. This is the typical thickness for

gas-liquid contacting experiments. However, for large scale operation it is required to have robust membranes with narrow pore size distribution, which give enhanced gas uptake. Such membranes have insufficient mechanical stability after long operational hours. This problem needs to be addressed without compromising the basic advantages of such membranes. One approach to achieve this is by the preparation of composite membranes. The support can either be a planar or a hollow fiber membrane. Thin film can be applied on the support by a "dip coating" method.

We considered Accurel-porous polypropylene (PP) hollow fibers as helical microchannels in Chapter 2. If PP hollow fibers are modified with a highly hydrophobic coating at the outer surface, it can be used for multiphase contacting. One of the potential application is stripping of volatile species from an aqueous solution on the shell side. The pores of the hollow fiber membrane are filled with an organic compound which wets the membrane pores except for the hydrophobic coating layer while aqueous solutions flows on the outer (shell) side of the membrane. The volatile species eventually permeate through the organic liquid in the lumen side and through the pores (where vacuum is maintained) of the PP hollow fiber,where they are recovered [4].

This thesis presents gas-liquid contacting where the two phases are separated by porous membranes with pores filled with gas. In an interesting application, the membrane (pores filled with gas) separates two liquid phases on either side of the membrane for direct contact membrane distillation (DCMD) [5]. With two stabilized gas-liquid interfaces, transport of one fluid phase to another will occur through the porous membrane. Two liquid phases are kept at different temperatures with evaporation at one interface and condensation taking place at the other interface. In another approach, two fluid phases are at the same temperature but the transport of one volatile component from one liquid phase to the other liquid phase via a concentration difference, which creates osmotic pressure difference across the membrane. This is termed as osmotic distillation and it is used for the concentration of fruit juices. The evaporation of volatile compound at the membrane interface results in temperature and concentration polarization. The fluid flowing along the hydrophobic membrane encounters alternating sections of solid-liquid interface and gas-liquid interface. Such inhomogeneous interfaces resemble the study performed on microgrooves in this study (Chapter 3 and 4) that produce the net effect of reducing the drag force experienced by the liquid. Study of Ramon et al showed that membrane distillation processes are positively affected by slip flow at the gas-liquid interface [6].

In Chapter 2, we have shown that gas-liquid contacting can be improved using passive

micromixing using porous helical membranes. Porous helical channel can be used in gas absorption, pervaporation, air stripping, aeration and de-aeration. In above operations, in order to improve the performance of the membrane module, secondary flows can be created which reduce concentration polarization.

7.2.2 Membrane reactors

Membrane reactors are used for process intensification purposes to bring economic and environmental benefits, such as reduced reactor volume, lower energy consumption and improved conversion and selectivity [8, 9]. They provide different ways of exploring and exploiting multiphase fluid behavior at a scale where diffusion, interfacial tension and viscous effects play a major role [10].

The selection of a microreactor module design for an operation greatly depends on the physical/chemical system and the operating conditions [11]. For mass transfer limited reactions, specifically engineered microreactors offer significant improvement in mass transfer.

In this project, Aran et al. [12] developed porous stainless steel (SS) hollow fibers with high porosity and mechanical strength. Carbon nanofibers (CNFs) with high surface area for catalyst support were grown on the porous SS surface. The reactors were then finished with an outside gas permeable polymeric coating. The CNFs on the SS surface improves the performance of the microreactor significantly. Such microreactors possess high catalytic surface area, mechanical strength and efficient gas-liquid contacting.

It is necessary to include the design of integrated heat management that can improve the control of the reaction temperature in the microchannel. For planar geometries, possible design could be a multi-layer microreactor concept providing heat integration across different layers. Obviously, the accurate distribution of the phases and control of process conditions are essential elements in this kind of scale-out design. For reaction involving aqueous mediums, evaporative cooling is also a promising option. Another interesting approach is to include nanofluids involving functionalities of reaction and heat transfer in multifunctional reactors. Nanofluids based on TiO_2 dispersed in ethylene glycol has been implemented in an integrated reactor assembly, which led to a significant increase in the overall heat transfer [13].

Integration of system elements, such as microactuators, mixers, sensors, dispensers, heat

exchangers and data analysis tools will be essential to expand the applicability of microcontactor/reactor devices and allow improved system control and operation.

Chemically modified surfaces provide manipulation of the wetting properties [14, 15]. Such surfaces can be effectively used to control the flow. By selectively patterning the surface with different properties, multiphase flow can be manipulated into a single phase system. This way interfacial forces can be utilized to stabilize the interface even at conditions where flow instabilities typically occur. There are multiple ways to selectively alter the wetting properties such as, plasma treatment [16], surface modification with silanes [17], UV treatment [18], deposition/coating of thin polymer film [19] and reversible switching of surface properties [20]. Another interesting approach is the change of surface tension by using surfactants at the gas-liquid interface.

For physical surface modifications, gas discharge based processes (i.e. plasma treatments) and photo-induced (i.e. UV) treatments offer simple process methods. UV-light can be used for photo-induced modifications that are restricted to the surface, without changing bulk properties.

In terms of flow field dynamics, velocity profiles in microreactors play an important role which affect momentum and mass transfer affecting the performance of the microreactor. With the availability of flow analysis devices, such as microPIV, investigation of mixing in microchannels (as discussed in this thesis in Chapter 4) can bring important results that will help to efficiently characterize the gas-liquid contacting using porous membranes.

Considering numerical simulations, the CFD models can be useful in designing and testing microfluidic systems. The fabrication of lab-on-a-chip systems is quite complex and requires interdisciplinary research and development. Additionally, the production time in a cleanroom facilities can be several weeks. So, numerical simulations are extremely useful, providing complete understanding of fundamental physical and chemical processes, and developing optimal designs.

7.2.3 Research opportunities

For chemical synthesis, the development of new and improved membrane reactors can begin from considering fundamental aspects of thermodynamics and transport phenomena [23]. For equilibrium-limited reactions, higher yields, selectivity and

conversions can be obtained by maintaining the reaction conditions which is possible by tuning the membrane functionality. This shows that equilibrium-limited processes which cannot be carried out at larger scale can find promising alternatives by configuring microreactor modules that are within the scope of technological development.

It is interesting to study the gas and liquid flow through porous structures to understand the complex flow fields. Porous medium is represented by a wide distribution of pore sizes and inter-connectivity of the porous structure. The flow through such a morphology leads to formation of pockets and finger like formations that cannot be filled by the intruding fluid. Most of the studies in this field is related to oil-recovery and related applications in petroleum engineering, e.g. carbon capture and sequestration. It is important to understand how multiple phases interact. Gas-liquid contacting through the array of microporous pillars (which can also be used as a catalyst support) can mimic the multiphase flow in a miniature packed bed. Marquez et al. [24] studied the flow pattern in such a reactor where they observed formations of stable gas-filled and liquid-filled zones after each pass of the slug. Such configurations can be useful in membrane based applications where local physical/chemical processes are relevant and it will help to eliminate additional surface modification methods.

In a typical microfluidic mixing process, the efficiency of the mixing can be controlled by the area of fluid/fluid interface through which molecular diffusion takes place. As discussed in Chapter 3 and 4 in this thesis, microgrooved membranes provide enhancement in flux for surface reactions, using slip velocity at the gas-liquid interface. One of the interesting study that can follow up this work is the recent research by Almarcha et al.[25] that showed a chemical reaction at the interface can lead to hydrodynamic instability which results in perturbation of the interface. The formation of product leads to a change in physical and chemical properties of the phases involved near the gas-liquid interface, giving rise to finger like structures from the reaction zone. The instabilities are similar to Rayleigh-Taylor type [26] and arise from an interaction between formed product and the convection-driven fluid flows. Interestingly, this process (self)propagates further as a result of severe concentration gradients at the interface. However, chemical reaction driven hydrodynamic instabilities require presence of gravity (high Bo) in order to drive convective flows which is a challenge in microfluidics as surface forces are dominant. The detailed modeling supported by experiments can give important insight into the system. An increase in temperature or addition of surfactants can lead to increase in Bo, which creates a situation for the hydrodynamic instability to appear in microchannels. This has been confirmed

by some preliminary simulations and experimental work in our group (SFI/TNW), where ethanol vapor induces Marangoni flow in microchannels resulting in enhanced mixing.

Although applications of membranes in lab-on-a-chip (LoC) devices have existed for quite some time, it is still possible to increase its usage in the field extensively. Membrane based application have added advantage of easy and economical fabrication compared to typical cleanroom technologies. Although not directly related to membranes, one example is micropatterned paper based diagnostic tools [27] which leads to the development of simple microfluidic systems for applications in public health in developing countries where diagnosis is often expensive and time-consuming. It is likely that future applications will see different approaches in the way porous membranes are applied: moving beyond the proof-of-concept stage and becoming an integral tool for complex technologies.

7.3 References

[1] A. Atkinson, A. Donev and R. Tobias, editors; *Optimum Experimental Designs*; ISBN 978-0-19-929659-0 (2007); New York: Oxford University Press

[2] H. Aran; *Porous ceramic and metallic microreactors: Tuning interfaces for multiphase processes*; Ph.D. thesis (2011)

[3] L. Vogelaar, R. Lammertink, J. Barsema, W. Nijdam, L. Bolhuis-Versteeg, C. Van Rijn and M. Wessling; *Phase separation micromolding: a new generic approach for microstructuring various materials*; Small **1** (6) (2005) 645–655

[4] Y. Qin, J. Sheth and K. Sirkar; *Pervaporation membranes that are highly selective for acetic acid over water*; Industrial & engineering chemistry research **42** (3) (2003) 582–595

[5] L. Song, B. Li, K. Sirkar and J. Gilron; *Direct contact membrane distillation-based desalination: novel membranes, devices, larger-scale studies, and a model*; Industrial & engineering chemistry research **46** (8) (2007) 2307–2323

[6] G. Ramon, Y. Agnon and C. Dosoretz; *Heat transfer in vacuum membrane distillation: Effect of velocity slip*; Journal of Membrane Science **331** (1-2) (2009) 117–125

[7] D. Zarkadas and K. Sirkar; *Antisolvent crystallization in porous hollow fiber devices*; Chemical engineering science **61** (15) (2006) 5030–5048

[8] R. Dittmeyer, K. Svajda and M. Reif; *A review of catalytic membrane layers for gas/liquid reactions*; Topics in catalysis **29** (1) (2004) 3–27

[9] G. Centi, R. Dittmeyer, S. Perathoner and M. Reif; *Tubular inorganic catalytic membrane reactors: advantages and performance in multiphase hydrogenation reactions*; Catalysis today **79** (2003) 139–149

[10] H. Stone, A. Stroock and A. Ajdari; *Engineering flows in small devices*; Annu. Rev. Fluid Mech. **36** (2004) 381–411

[11] K. Jähnisch, V. Hessel, H. Löwe and M. Baerns; *Chemistry in microstructured reactors*; Angewandte Chemie International Edition **43** (4) (2004) 406–446

[12] H. Aran, S. Pacheco Benito, M. Luiten-Olieman, S. Er, M. Wessling, L. Lefferts, N. Benes and R. Lammertink; *Carbon nanofibers in catalytic membrane microreactors*; Journal of Membrane Science **381** (1-2) (2011) 244–250

[13] H. Chen and Y. Ding; *Heat Transfer and Rheological Behaviour of Nanofluids–A Review*; Advances in Transport Phenomena pages 135–177

[14] M. Tokeshi, T. Minagawa, K. Uchiyama, A. Hibara, K. Sato, H. Hisamoto and T. Kitamori; *Continuous-flow chemical processing on a microchip by combining microunit operations and a multiphase flow network*; Analytical chemistry **74** (7) (2002) 1565–1571

[15] B. Zhao, J. Moore and D. Beebe; *Surface-directed liquid flow inside microchannels*; Science **291** (5506) (2001) 1023

[16] A. Tserepi, E. Gogolides, K. Tsougeni, V. Constantoudis and E. Valamontes; *Tailoring the surface topography and wetting properties of oxygen-plasma treated polydimethylsiloxane*; Journal of applied physics **98** (2005) 113502

[17] B. Grzybowski, R. Haag, N. Bowden and G. Whitesides; *Generation of micrometer-sized patterns for microanalytical applications using a laser direct-write method and microcontact printing*; Analytical Chemistry **70** (22) (1998) 4645–4652

[18] V. Lien, Y. Berdichevsky and Y. Lo; *A prealigned process of integrating optical waveguides with microfluidic devices*; Photonics Technology Letters, IEEE **16** (6) (2004) 1525–1527

[19] H. Chen, Y. Elkasabi and J. Lahann; *Surface modification of confined microgeometries via vapor-deposited polymer coatings*; Journal of the American Chemical Society **128** (1) (2006) 374–380

[20] J. Lahann, S. Mitragotri, T. Tran, H. Kaido, J. Sundaram, I. Choi, S. Hoffer, G. Somorjai and R. Langer; *A reversibly switching surface*; Science **299** (5605) (2003) 371

[21] R. Allen, S. Melchionna and J. Hansen; *Intermittent permeation of cylindrical nanopores by water*; Physical review letters **89** (17) (2002) 175502

[22] R. Roth and K. Kroll; *Capillary evaporation in pores*; Journal of Physics: Condensed Matter **18** (2006) 6517

[23] J. Moulijn, J. Perez-Ramirez, A. van Diepen, M. Kreutzer and F. Kapteijn; *Catalysis engineering on three levels*; International Journal of Chemical Reactor Engineering **1** (1) (2003) 4

[24] N. Marquez, P. Castano, J. Moulijn, M. Makkee and M. Kreutzer; *Transient Behavior and Stability in Miniaturized Multiphase Packed Bed Reactors*; Industrial & Engineering Chemistry Research **49** (3) (2009) 1033–1040

[25] C. Almarcha, P. Trevelyan, P. Grosfils and A. De Wit; *Chemically driven hydrodynamic instabilities*; Physical review letters **104** (4) (2010) 44501

[26] D. Sharp; *An overview of Rayleigh-Taylor instability*; Physica D: Nonlinear Phenomena **12** (1-3) (1984) 3–10

[27] A. Martinez, S. Phillips and G. Whitesides; *Three-dimensional microfluidic devices fabricated in layered paper and tape*; Proceedings of the National Academy of Sciences **105** (50) (2008) 19606

Summary

This thesis describes research work about multiphase contacting/reactions using porous membranes. Membrane based gas-liquid contacting offers many benefits, such as stable operation, easy fabrication and sustainable module design. Furthermore, accurate reaction control, higher mass transport due to enhanced surface-to-volume ratios and continuous operation are other key advantages of membrane based multiphase contacting/reaction. In this thesis, **Chapter 2-4** focus on improving (physical) gas-liquid mass transfer using different geometrical configurations and **Chapter 5** and **6** describe detailed modeling approach to characterize the performance of heterogeneously catalyzed membrane microreactor.

Chapter 2 describes the concept of helical membrane channels to generate mixing at a microscale. The mixing performance of helical channel is compared with straight channel using numerical and experimental studies. The results show that helical structures perform more effectively compared to straight microchannel. The helical design was exploited to produce secondary flows in microchannels, which enhances mixing. The optimization study revealed that the flux enhancement is strongly dependent on the geometrical configuration of the microchannel, i.e. the curvature diameter, helical pitch and internal channel diameter.

In **Chapter 3**, numerical and optimization study was performed to evaluate transport effects for microgrooved membranes. Two types of microgrooves have been studied in relation to mass transport: continuous and non-continuous microgrooves. The liquid flow field is greatly influenced by these microgrooves and enhanced mass transport is achieved. A detailed geometrical optimization study conducted to study the enhancement in flux for microgrooved membranes compared to flat membranes. This research indicates that structured hydrophobic porous membranes can be successfully employed to increase mass transfer and reduce concentration polarization along the gas-liquid interface.

Chapter 4 describes experimental work related to the numerical study described in Chapter 3. A microgrooved membrane for gas-liquid contacting was fabricated using liquid induced phase-separation. An experimental study using grooved membranes suggest enhancement in flux up to 30 %. The flux enhancement is observed due to a partial shear-free gas-liquid interface. The performance of the membrane devices decreased with wetted microgrooves due to mass transport limitations. The flow

visualization experiments reveal wetting of the microgrooves at higher liquid flow rates. According to both the numerical simulations and experimental observations of the gas-liquid contacting, it was shown that it is possible to increase the gas uptake in liquid by merely structuring the membrane surface.

Chapter 5 presents a detailed modeling approach for a porous membrane microreactor that covers a wide range of operating conditions and microreactor configurations. The model and numerical simulations were validated with experimental data. The boundary condition representing the reactor wall concentration as a function of catalytic membrane layer thickness was obtained and an optimum in conversion and catalytic layer thickness was found. By comparing several flow rates and reactor diameters, it is concluded that a small channel diameter is important to achieve increased mass transfer to reactive boundaries. The performance of the microreactor drops at higher catalytic layer thickness due to gaseous reactant mass transfer limitation. The numerical model provides useful insight into the understanding of mass transport and catalytic reactions in membrane microreactors.

Chapter 6 describes a numerical model for photocatalytic degradation of methylene blue (MB) in a planar photocatalytic microreactor, which was validated with experimental observations. Influence of the radiation intensity in the photocatalytic layer has been included via the optical thickness. The study showed that the degradation of MB is dependent on the optical thickness of the photocatalytic layer. The effectiveness factor of the photocatalytic film is considered to study the performance of the microreactor. It was shown that the effectiveness factor is strongly influenced by the distribution of UV radiation in the photocatalytic film. The model optimizes geometrical parameters of the photoreactor and analyzes distribution of the radiation intensity across the photocatalytic film.

The last chapter, **Chapter 7** "Conclusions and outlook, summarizes results obtained in the previous chapters and provides ideas and needs for future research.

Samenvatting

Dit proefschrift bevat onderzoek naar meer fasen contacting/reacties gefaciliteerd door poreuze membraan microcontactoren/reactoren. Het gebruik van membraan reactoren/contactoren heeft door de relatief kleine dimensies voordelen in vergelijking tot conventionele reactoren/contactoren. Enkele van deze voordelen zijn:

- Een significant grotere oppervlakte/volume verhouding
- Hogere stofoverdracht
- Continue stabiel contact tussen gas en vloeistof fase
- Makkelijk en duurzaam ontwerp
- Systeem is beter beheersbaar

In het eerste hoofdstuk van dit proefschrift wordt een inleiding gegeven waarin het fenomeen meer fasen contacting beschreven wordt. Vervolgens focussen **hoofdstukken 2-4** zich op het verbeteren van de stofoverdracht in membraan microreactoren/contactoren doormiddel van het optimaliseren van de geometrie. In **hoofdstukken 5** en **6** wordt er een gedetailleerde aanpak (model) gepresenteerd voor het karakteriseren van heterogene katalytische reacties in een (membraan) microreactor.

Hoofdstuk 2 beschrijft het concept van spiraalvormige microreactoren, waarbij door ge geometrie menging op microschaal optreedt. De prestaties in stofoverdracht van een spiraalvormige membraan reactor/contactor zijn vergeleken met de prestaties van een rechte membraan microreactor/contactor. Dit is gedaan door zowel numerieke als experimentele studies uit te voeren. De resultaten laten zien dat spiraal vormige geometrien efficinter zijn dan de rechte geometrien. Dit is toe te schrijven aan secondaire stromingen welke ontstaan in de spiraalvormige geometrien. Een optimalisatie studie laat zien dat de mate van efficintie sterk afhankelijk is van de gekozen geometrie, belangrijke variabelen hierin zijn onder andere; de diameter van de kromming, de afstand tussen de krommingen en de interne diameter van de microkanalen.

In **hoofdstuk 3** is het effect van micropatronen op een hydrofobe poreuze membraan oppervlakten numeriek bestudeerd. De micropatronen zullen zich indien er aan een aantal randvoorwaarden voldaan worden zich vullen met gas. Over het gas/vloeistof oppervlak van de micropatronen zal hierdoor minder wrijving zijn dan met het

oppervlak van het membraan. Dit resulteert in een ander stromingsprofiel. De numerieke studie laat zien dat het stromingsprofiel inderdaad veranderd en hierdoor de concentratie polarisatie aan de oppervlakte van het membraan verminderd. Dit heeft uiteindelijk tot gevolg dat de stofoverdracht toeneemt.

Hoofdstuk 4 beschrijft experimenteel werk gerelateerd aan de numerieke studie uitgevoerd in hoofdstuk 3. Voor deze experimenten is een poreus hydrofoob membraan met een micropatroon op het oppervlakte geproduceerd aan de hand van vloeistof/vloeistof fasen scheiding. De resultaten van de experimenten laten een toename tot 30 % in de stofoverdracht zien in vergelijking met een patroonloos membraan. De prestaties van membraan modules namen af wanneer de micropatronen gevuld werden met vloeistof, dit gebeurd onder andere bij verhoogde stromingssnelheden. Dit wordt toegeschreven aan stofoverdrachtslimitaties welke optreden bij de met vloeistof gevulde micropatronen. De conclusie van hoofdstuk 3 en 4 is dat door enkel een patroon op het membraanoppervlak aan te brengen de stofoverdracht verhoogd kan worden.

Hoofdstuk 5 presenteert een gedetailleerde modellerings-aanpak voor poreuze microreactoren, welke toepasbaar is over een groot gebied van operating condities en microreactor configuraties. Het beschreven model en de numerieke simulaties zijn gevalideerd met experimentele data. De randvoorwaarde voor de reactorwal concentratie als functie van de katalytische membraan laag dikte was gevonden. Met deze randvoorwaarde is een optimum gevonden in de conversie en dikte van de katalytische laag. Door het vergelijken van verschillende stroom snelheden en reactor diameters, kan de conclusie getrokken worden dat een kleine reactor diameter belangrijk is in het bereiken van verhoogde stofoverdracht naar de reactieve reactorwanden. De prestaties van de microreactor verminderd bij een toenemende dikte van de katalytische laag door stofoverdracht limitatie van de in de gasfase zijnde reactant. Het numerieke model geeft een inzicht in de stofoverdracht in membraan microreactoren.

Hoofdstuk 6 beschrijft een numeriek model voor foto-katalytische degradatie van methyleen blauw (MB) in een vlakke foto-katalytische microreactor. Het model is gevalideerd met experimentele observaties. De invloed van de intensiteit van de radiatie in de foto-katalytische laag is meegenomen via de optische dikte. De studie laat zien dat de degradatie van MB is afhankelijk van de optische dikte van de foto-katalytische laag. De effectiviteits factor van de foto-katalytische film is gevarieerd om de effectiviteit van de microreactor te bestuderen. Het is aangetoond dat de effectiviteits factor sterk benvloed wordt door de distributie van UV straling in de foto-katalytische laag. Aan de hand van het model kunnen geometrische parameters van foto-reactor geoptimaliseerd

worden. Tevens analyseert het model de distributie van de radiatie intensiteit over de foto-katalytische film.

Het laatste hoofdstuk, hoofdstuk Conclusions and outlook, vat de resulaten verkregen in de voorgaande hoofdstukken samen en draagt ideen aan voor toekomstig onderzoek.

Acknowledgements

It has been a great journey for me during these four years of PhD work. It was indeed a great learning experience both at personal and scientific fronts. In the process, I have met many supporting, inspirational and motivating people whom I would like to thank and show my deepest gratitude.

Firstly, I sincerely thank my inspirational promoter, guide and supervisor Prof.Dr. Rob Lammertink for giving me this wonderful opportunity to pursue my PhD. I very well remember our first lunch meeting (during interview) when you briefly explained about the future research work, and it immediately impressed me and convinced me to pursue my career working with you. You always motivated me to try on new things, gave instant and constructive feedback, and allowed me to think differently. I was always inspired by your research insightfulness and problem solving approach. Your friendly nature allowed me to discuss openly on many issues, at both scientific and personal level. I highly appreciate your time and efforts in reading and correcting this thesis. I am greatly indebted to you for all the support, guidance, ideas and help without which my PhD would not have been possible.

I also appreciate the help and support provided by Prof.Dr. Matthias Wessling. I would like to thank you for sharing your knowledge, experience and ability to make research interesting. I am very thankful for your guidance and suggestions during PhD.

It is very necessary to understand and adjust with the working environment in a new country. Thankfully, I never had to worry about these small but very important tasks due to Greet for her excellent administrative help and support. I also thank Lidy and Nienke for their help in my last years of PhD. Thank you very much for making my life so simple and easy during my PhD.

I would also like to extend my thanks to my past officemates of ME321; Bernke, Matias, Mike, Anne Corine, Jeroen and Sandra. I had nice time with you all, especially those discussions and cookies. I am also thankful to my other office mates in ME312; Can, Elif and Ineke. You were all very fun loving and supportive officemates.

I would like to mention special thanks for my very good friend and project partner, Can Aran. I am very fortunate to have you as my project buddy with whom I shared all ups and downs during PhD. We shared many wonderful moments during four years of PhD. I enjoyed every discussion with you and your attitude towards looking at things differently. Ofcourse, how can I forget our awesome parties, conferences and coffee breaks? I feel extremely lucky to meet you, and treasure you as a friend. I would also like to wish you and Laura all the best wishes for your life ahead.

I would also like to express my thanks to my friend and paranymph Mayur Dalwani. We are friends since our old masters days (7 years) and I share a long and unique friendship with you. Till now, we have seen quite interesting (and pleasant!!) analogies in our lives and in future we expect to see them more, you know what I mean!!!! I

had really nice time with you and Shraddha during all the festivals, dinners and get together. I truly appreciate your friendship and wish you both all the best.

Srivatsa, my special friend, you were very helpful and supportive in every situation. Your friendship will remain always special throughout my life. I wish you good luck for your career and life ahead.

I also thank Jeroen Ensink who worked with me for his Masters assignment and contributed his research work in this thesis (Chapter 3) and the Dutch summary. It was great working with you, you are now a good friend and I wish you best of luck for your life. My thank also extends to my friends Juan, Jordi, Gregory and Shaun for all the nice times.

Working in MTG/SFI was always fun because of the colleagues I was working with. I thank Harmen, Herman, John Heeks, Marcel, Erik, Erik vdV and Antoine for all their technical help and support. I really enjoyed all the group activities like borrels, BBQs, sand-volleyballs, NPS parties, bike tours, batavierenrace (I am 4 time proud runner ☺), pub-quiz and bowling events. I also thank Jorrit, Katja, Sander, Jens, Hakan, Zeynep, Wilbert, Ikenna, Kareena, Joao, Gerard, Alisia, Paul, Nicolas, Wika, Geraldine, Ana, Marlon, David, Olga, Enver, Harro, Al-Hadidi, Wojciech, Gor, Yusuf, Irdham, Jorris and Jumeng for all the nice time and fun.

Pravin uncle and Seema aunty, our dutch parents, I would say we have been very blessed to have you here as part of our family. Your support and guidance in every aspect of life matters a lot to me. I highly appreciate your love, care and seek your blessings for rest of my life. I also wish Prashad and Sheetal all the best for their future.

I also extend my gratitude towards the Indian community in Enschede, with whom I always felt home-away from home. I specially thank Pramod-Vishakha, Chandu-Minakshi, Supriyo Anindita, Dhaval-Hinal, Vikram-Ashmita, Chintan-Usha, Vijaya-Sangeeta, Pitbhai-Kamlaji, Panduranga-Pallavi, Jeetu-Lavanya, Sandeep-Jalaja, Sreenath-Vidhya, Digvijay-Abha, Omkar-Sampada, Giri-Varsha, Kishore-Hema, Arun, Raghav, Shashank, Hemant, Nilesh and Hanumant-Neeru. I had amazing time with you during all Indian functions, festivals and dinners. I will always cherish those beautiful moments spent with you all.

My parents have always been immense source of inspiration, support and guidance throughout my life and career. Without their unconditional love and care, I would not have achieved anything in this life. I have no words to express my gratitude towards them. Mummy, pappa tame aapeli shiksha badhi degree karta mahaan che. Tame aam j tamara ashirvaad ane prem aapta rehjo. Ujjval, you have been always with me in all my thicks-n-thins and supported me in all my struggles, I thank you very much for everything. I also heartily thank mumma, papa and Vishal for all the love and support.

Finally, I thank the most special, beautiful and important person in my life, my wife-Falguni. Honestly, I have no clue how to thank you for all the sacrifices you have

made, for all the things that you looked after and for all incessant torrent of love and care that you gave me. You just cannot stop impressing me even after almost three years of our marriage, that I always discover new energy, talent and force in you. I am always in best of my comfort whenever I am with you and feel completeness in your presence. And soon we are expecting little member in our Jani family, I can proudly say that I have got the most lovely wife in this world. I love you.

Jigar